COMPARTMENTAL TISSUE CHARACTERIZATION USING NMR RELAXOMETRY

By

Richard D. Dortch

Dissertation

Submitted to the Faculty of the

Graduate School of Vanderbilt University

in partial fulfillment of the requirements

for the degree of

DOCTOR OF PHILOSOPHY

in

Biomedical Engineering

May, 2009

Nashville, Tennessee

Approved:
Professor Mark D. Does
Professor Adam W. Anderson
Professor John C. Gore
Professor Todd E. Peterson
Professor William M. Valentine
Professor Thomas E. Yankeelov

To my wife, Shannon

and

To my son, Samuel

ACKNOWLEDGEMENTS

I am grateful to the many people who made significant contributions to this project. I first want to thank my committee members for their support and guidance. I feel truly lucky to have worked with such a talented group of scientists. I especially want to thank my advisor, Dr. Mark Does, for the many opportunities he has provided throughout my tenure as a graduate student. Without his support, expertise, and flexibility — giving me the freedom to pursue numerous ideas, some of which yielded promising results, many of which did not — none of the work presented herein would have been possible.

In addition to these contributions, this research would not have been possible without the available resources within the Vanderbilt University Institute of Imaging Science (VUIIS). I specifically want to thank Dr. John Gore for establishing an environment rich in not only state-of-the-art imaging resources, but also in talent, knowledge, and collaborative spirit. Additionally, I would like to acknowledge funding from the National Institutes of Health (Grant #EB001744, PI: Mark Does) and the National Science Foundation (Career Award #0448915, PI: Mark Does), which has allowed me to utilize the aforementioned resources within the VUIIS.

My family and friends have provided much needed emotional support throughout this process. I specifically want to thank my mom for her guidance and for instilling in me the work ethic needed to survive graduate school. Finally, and most importantly, I want to thank my wonderful wife, Shannon, who is a constant source of love, support, and inspiration.

TABLE OF CONTENTS

LIST OF TABLES

LIST OF FIGURES

CHAPTER I

BACKGROUND AND SIGNIFICANCE

Introduction

MRI is unique in its sensitivity to a wide array of contrast mechanisms in soft tissue. Unfortunately, MRI acquisitions are typically limited to spatial resolutions on the order 1 mm^3. At this scale, the physiological and/or microanatomical parameters that give rise to the observed contrast can show significant heterogeneity. Ideally, one could decrease the imaging resolution to limit this heterogeneity; however, this is not often practical due to signal-to-noise ratio (SNR) and/or acquisition time limitations.

Techniques are available for separating compartmental signals based upon differences in T_2 relaxation times [1, 2]. When used in conjunction with the appropriate compartmental tissue model, these techniques allow one to resolve signal from tissue compartments that exist on a sub-voxel scale. For example, these methods have been applied in myelinated tissue (e.g., white matter [3, 4], peripheral nerve [5-8]) to resolve myelin water signal (water trapped between the myelin bilayers) from the bulk NMR signal. The fractional contribution of the myelin water signal to the bulk signal, or myelin water fraction (WMF), has been shown to correlate with myelin content [3, 8-12] while being less sensitive than other methods [e.g, magnetization transfer (MT)] to confounding factors such as inflammation [13]. Despite this promise, several fundamental questions still remain with regards to: 1) the relationship between the extracted signal components and underlying tissue compartments and 2) the effect of intercompartmental

water exchange on the extracted compartment sizes. Both of these fundamental questions will be addressed herein as discussed below.

Compartmental Models of Myelinated Tissue

Myelin is an insulating sheath that surrounds axons. The myelin sheath is formed by glial cells — oligodendrocytes in the central nervous system (CNS) and Schwann cells in the peripheral nervous systems (PNS) — that wrap their processes about axonal segments in a spiral-like manner. The main consequence of myelination is increased conduction velocity of action potentials through a process known as saltatory conduction. This arises due to a number of factors unique to the myelin sheath including its: 1) segmental structure, 2) high lipid content (70% dry weight), 3) low water content (40% total volume), and 4) thickness (0.1–0.6 μm in CNS and 0.2–2.0 μm in PNS) [14-17]. Loss of the myelin sheath, or demyelination, is a hallmark of a number of pathologies (e.g., multiple sclerosis). Following demyelination, conduction of action potentials can be impaired or lost. In some cases, remyelination of axons can occur; however, the new myelin sheaths are often thinner and, consequently, less effective [17]. Though much progress has been made in understanding these processes, much is still not understood.

In addition to facilitating saltatory conduction, the myelin sheath also acts as a barrier to water exchange. As a result, three distinct water compartments are found in myelinated tissue: 1) myelin water, or mobile water between myelin bilayers, 2) axonal water, or mobile water within myelinated axons, and 3) interaxonal water, or all mobile water outside of the myelin sheath. This compartmental model is illustrated in Fig. 1.1 in an electron micrograph of frog sciatic

nerve. It is commonly assumed that exchange between all subcompartments (e.g., axoplasm and intracellular organelles) is fast on the T_2 timescale. As a result, signal from myelinated tissue can be modeled as a sum of signal from these three compartments: myelin water, axonal water, and interaxonal water.

Fig. 1.1. Electron micrograph of frog sciatic nerve showing the three distinct microanatomical compartments: myelin (M), axonal (A), and interaxonal (I) compartments.

Peripheral Nerve

Much of the pioneering work with regards to compartmental modeling of neural tissue has been performed in peripheral nerve, which is functionally and structurally similar to white matter. Swift and Fritz [5] first demonstrated that T_2 relaxation was nonmonoexponential in peripheral nerve. Work by Vasilescu *et al.* [6] a decade later showed that peripheral nerve was indeed best characterized by three T_2 components, which is consistent with the compartmental model described in the previous section. More recently, Does *et al.* showed that the derived T_2 components in nerve exhibit unique T_1s [18-20] and MT properties [18], which further argues for the assignment of these T_2 components to unique microanatomical water compartments. Based upon this body of work, peripheral nerve is modeled as a sum of three T_2 components: 1) a short-lived component with a $T_2 \approx 15$ ms that represents approximately 20% of the signal, 2) an intermediate-lived component with a $T_2 \approx 70$ ms that represents approximately 50% of the signal,

and 3) a long-lived component with a $T_2 \approx 300$ ms that represents approximately 30% of the signal.

The short-lived T_2 component in nerve has long been thought to represent myelin water, given the larger pool of exchangeable semi-solid protons available to myelin water — recall that myelin has a high macromolecular content and relatively low water content. This assignment has been confirmed experimentally by its absence in nonmyelinated nerve [21] as well by its disappearance following demyelination [8]. Studies in crayfish abdominal nerve have also shown that the MWF correlates with histologically-derived estimates of the fractional water volume of the myelin compartment. As a result, the current consensus is that the short-lived T_2 component represents myelin water in peripheral nerve.

Assignment of the intermediate- and long-lived T_2 components to underlying tissue compartments has proven to be less straightforward. Vasilescu *et al.* [6] first assigned the intermediate- and long-lived components to axonal and interaxonal water, respectively, based upon comparison of the T_2 component sizes to previously derived [22] compartment sizes from studies of H_2O–D_2O diffusion-mediated exchange. Menon *et al.* [23] made the same assignment based upon similarities between the fractional size of the T_2 components and histologically-derived estimates of the fractional water volume of each compartment. These results were supported in part by compartmental MT studies by Does *et al.* [18]. The authors found that the intermediate-lived T_2 component signal exhibited a larger MT effect than the long-lived T_2 component signal, which is consistent with the assumption that the axonal space has a larger pool of exchangeable semi-solid protons than does the interaxonal space.

Two more recent studies have reversed this assignment. Peled *et al.* [24] found that diffusion was more restricted for the long-lived T_2 component signal than for the intermediate-lived T_2

component signal. Assuming that diffusion is more restricted in the axonal space than the interaxonal space, this suggests assignment of the intermediate- and long-lived T_2 components to interaxonal and axonal water, respectively. More recently, Wachowicz *et al*. [25] perfused excised sciatic nerve with a solution containing contrast reagents and noted a shift in T_2 times for the intermediate-lived T_2 component prior to the other components. Assuming the interaxonal space has access to the perfused reagent prior to the other compartments, this supports the previous finding of Peled *et al.* [24].

Based upon this body of work, the intermediate- and long-lived T_2 components are tentatively assigned to interaxonal and axonal water, respectively. The fact that interaxonal water exhibits a shorter T_2 than axonal water is somewhat puzzling as it goes against the assumption that the pool of exchangeable semi-solid protons is larger in the axonal space. Peled *et al.* [24] have suggested that the abundance of collagen I in the endoneurium might explain this shorter T_2 for interaxonal water.

White Matter and Optic Nerve

Like peripheral nerve, T_2 relaxation is nonmonoexponential in white matter as first demonstrated by Menon *et al.* [26]. Unlike peripheral nerve, a sizeable body of work has shown that white matter is best characterized by two T_2 components [3, 4, 9, 12, 27-29]: 1) a short-lived component with a T_2 = 10−30 ms that represents 10−30% of the signal and 2) a long-lived component with a $T_2 \approx 80$ ms that represents the remaining signal fraction. Additional studies in optic nerve [30, 31], a commonly used model for white matter, have also identified two T_2 components with similar relaxation times and signal fractions, although a more recent study has

identified three T_2 components in optic nerve [32]. The results presented herein suggest that optic nerve is best characterized by two T_2 components.

Drawing from studies in peripheral nerve, early studies in white matter assigned the short-lived T_2 component to myelin water. Experimentally, this has been verified in white matter through an observed: 1) decrease in MWF in demyelinating tissues [3, 4, 9] and 2) correlation between MWF and quantitative myelin measurements derived from histology [12, 29]. Further evidence of this assignment has been obtained through compartmental characterization of diffusion [30] and MT [31] in optic nerve.

The long-lived T_2 component in white matter is thought to represent all non-myelin water. In other words, white matter signal arising from axonal and interaxonal water is not resolvable based upon differences in compartmental T_2s. Ideally, one could duplicate the compartmental studies of diffusion [24, 33] and MT [18] performed in peripheral nerve to determine whether the compartmental characteristics of these quantities are preserved in white matter. Unfortunately, this is not possible for axonal and interaxonal compartments in white matter.

Compartment-specific Contrast Reagents

The inability to resolve signal from axonal and interaxonal water in white matter likely arises because each compartment exhibits similar relaxation characteristics. Under this presumption, signal from these compartments could be isolated by preferentially altering the T_1 and/or T_2 of axonal or interaxonal water using a compartment-specific contrast reagent.

Recent work in optic nerve [34] suggests that Gd-DTPA, which does not cross intact cell membranes, may be such a reagent. One potential drawback of this approach is that Gd-DTPA has been shown to cross cell membranes in fixed tissue [35]. Chromium, specifically Cr(VI) in

the form of potassium dichromate, may be another such reagent as it has been shown to result in white matter specific enhancement following injection into neural tissue [36]. This enhancement is thought to arise due to reduction of diamagnetic Cr(VI) to paramagnetic chromium species [Cr(V) and/or Cr(III)] by oxidizable myelin lipids. That is, enhancement is "turned on" following tissue-specific reduction of Cr(VI). Though myelin lipids are thought to play a primary role, differential enhancement of axonal and interaxonal water may occur as exchange with and/or access to paramagnetic chromium may be different for these compartments.

Intercompartmental Exchange

Thus far, water exchange between compartments has not been discussed. Previous work suggests that this exchange is relatively slow, but not insignificant, in white matter and optic nerve [31, 37, 38] and very slow in peripheral nerve [18] on the T_2 timescale — note the larger effect in CNS, which is thought to arise due to thinner myelin sheaths. As a result, exchange is typically neglected in the compartmental models used to describe myelinated tissue in the CNS and PNS, especially with respect to T_2.

Though exchange is typically neglected, quantification of exchange rates in myelinated tissue is still of interest for several reasons. For one, quantification of these rates is needed to complete the compartmental model. Knowledge of these rates might prove useful in a number of simulation and optimization studies (e.g., optimizing studies of compartment-specific contrast enhancement). Secondly, exchange rates may be effected by a number of pathological states (e.g, demyelination, remyelination), which could result in apparent changes in MWF that do not reflect changes in myelin content — MWF is increasingly underestimated with increasing exchange rate. Finally, the timescale of other NMR properties (e.g., T_1, diffusion) is typically

much longer than the timescale of T_2. In these cases, the effects of intercompartmental exchange will be more significant. For example, Bjarnason *et al.* [38] found that the T_1 recovery in excised white matter was best described by a single component at physiological temperatures, while the T_2 decay from the same tissue was best described by two components. These results suggest that intercompartmental exchange in white matter is relatively slow in the T_2 timescale, but relatively fast on the T_1 timescale.

Exchange rates have been previously quantified in optic nerve [31] and white matter [38] *ex vivo*. In each of these studies, multidimensional MT−T_2 data were collected and fitted to a four-pool model comprised of: 1) myelin water, 2) non-myelin water, 3) semi-solid protons within the myelin compartment, and 4) semi-solid protons within the non-myelin compartment. Unfortunately, the intercompartmental exchange rates derived from each of these studies were quite different. Given the structural similarity between white matter and optic nerve, these differences likely cannot be explained solely by the differences in tissue model used and can most likely be attributed to a combination of: 1) the large number of free parameters in the four-pool model and 2) the different methods used to collect the MT−T_2 data. Given the discrepancy between the findings of these two studies, additional studies are needed to quantify exchange rates in myelinated tissue.

Dissertation Overview

The primary aims of this work are to: 1) develop and validate novel methods for measuring intercompartmental exchange 2) apply these methods in myelinated tissue, and 3) develop methods for resolving axonal and interaxonal water in white matter and optic nerve. Basic NMR theory and methods are first outlined in Chapter II. In the following chapters, novel methods for

measuring intercompartmental exchange are developed (Chapter III), validated *via* simulation and phantom studies (Chapter IV), and applied in model tissue systems (Chapter V). In Chapter VI, compartmental relaxation measurements are presented in a wide array of myelinated tissues before and after administration of contrast reagents as a means to characterize the compartmental enhancement pattern associated with each reagent. These measurements were used in conjunction with the exchange measurements in Chapter V to aid interpretation of the compartmental selectivity of each reagent. Chapter VII describes an additional study involving compartmental characterization of a rat gliobastoma model *in vivo*. Chapter VIII concludes the dissertation and outlines possible future directions.

References

[1] C. L. Lawson and R. J. Hanson, *Solving Least Squares Problems*. Englewood Cliffs, NJ: Prentice-Hall, 1974.

[2] K. P. Whittall and A. L. Mackay, "Quantitative Interpretation of NMR Relaxation Data," *J Magn Reson*, vol. 84, pp. 134–152, 1989.

[3] W. A. Stewart, A. L. Mackay, K. P. Whittall, G. R. W. Moore, and D. W. Paty, "Spin-spin relaxation in experimental allergic encephalomyelitis: Analysis of CPMG data using a nonlinear least-squares method and linear inverse-theory," *Magn Reson Med*, vol. 29, pp. 767–775, 1993.

[4] A. Mackay, K. Whittal, J. Adler, D. Li, D. Paty, and D. Graeb, "In-vivo visualization of myelin water in brain by magnetic resonance," *Magn Reson Med*, vol. 31, pp. 673–677, 1994.

[5] T. J. Swift and O. G. Fritz, "A proton spin-echo study of state of water in frog nerves," *Biophysics J*, vol. 9, pp. 54–59, 1969.

[6] V. Vasilescu, E. Katona, V. Simplaceanu, and D. Demco, "Water compartments in myelinated nerve. 3. Pulsed NMR results," *Experientia*, vol. 34, pp. 1443–1444, 1978.

[7] M. D. Does and R. E. Snyder, "T_2 relaxation of peripheral nerve measured in-vivo," *Magn Reson Imaging*, vol. 13, pp. 575–580, 1995.

[8] M. D. Does and R. E. Snyder, "Multiexponential T_2 relaxation in degenerating peripheral nerve," *Magn Reson Med*, vol. 35, pp. 207–213, 1996.

[9] P. J. Gareau, B. K. Rutt, S. J. Karlik, and J. R. Mitchell, "Magnetization transfer and multicomponent T_2 relaxation measurements with histopathologic correlation in an experimental model of MS," *J Magn Reson Imaging*, vol. 11, pp. 586–595, 2000.

[10] S. Webb, C. A. Munro, R. Midha, and G. J. Stanisz, "Is multicomponent T_2 a good measure of myelin content in peripheral nerve?" *Magn Reson Med*, vol. 49, pp. 638–645, 2003.

[11] E. E. Odrobina, T. Y. J. Lam, T. Pun, R. Midha, and G. J. Stanisz, "MR properties of excised neural tissue following experimentally induced demyelination," *NMR Biomed*, vol. 18, pp. 277–284, 2005.

[12] C. Laule, E. Leung, D. K. Lis, A. L. Traboulsee, D. W. Paty, A. L. MacKay, and G. R. Moore, "Myelin water imaging in multiple sclerosis: quantitative correlations with histopathology," *Mult Scler*, vol. 12, pp. 747–753, 2006.

[13] G. J. Stanisz, S. Webb, C. A. Munro, T. Pun, and R. Midha, "MR properties of excised neural tissue following experimentally induced inflammation," *Magn Reson Med*, vol. 51, pp. 473–479, 2004.

[14] R. W. Williams and L. M. Chalupa, "An analysis of axon caliber within the optic nerve of the cat: evidence of size groupings and regional organization," *J Neurosci*, vol. 3, pp. 1554–1564, 1983.

[15] R. L. Friede and W. Beuche, "A new approach toward analyzing peripheral nerve fiber populations. I. Variance in sheath thickness corresponds to different geometric proportions of the internodes," *J Neuropathol Exp Neurol*, vol. 44, pp. 60–72, 1985.

[16] R. M. Henkelman, G. J. Stanisz, J. K. Kim, and M. J. Bronskill, "Anisotropy of NMR properties of tissues," *Magn Reson Med*, vol. 32, pp. 592–601, 1994.

[17] N. Baumann and D. Pham-Dinh, "Biology of oligodendrocyte and myelin in the mammalian central nervous system," *Physiol Rev*, vol. 81, pp. 871–927, 2001.

[18] M. D. Does, C. Beaulieu, P. S. Allen, and R. E. Snyder, "Multi-component T_1 relaxation and magnetisation transfer in peripheral nerve," *Magn Reson Imaging*, vol. 16, pp. 1033–1041, 1998.

[19] M. D. Does and J. C. Gore, "Compartmental study of T_1 and T_2 in rat brain and trigeminal nerve in vivo," *Magn Reson Med*, vol. 47, pp. 274–283, 2002.

[20] A. R. Travis and M. D. Does, "Selective excitation of myelin water using inversion-recovery-based preparations," *Magn Reson Med*, vol. 54, pp. 743–747, 2005.

[21] C. Beaulieu, F. R. Fenrich, and P. S. Allen, "Multicomponent water proton transverse relaxation and T_2-discriminated water diffusion in myelinated and nonmyelinated nerve," *Magn Reson Imaging*, vol. 16, pp. 1201–1210, 1998.

[22] V. Vasilescu, D. G. Margineanu, and E. Katona, "Heavy water intake in tissues. II.H_2O-D_2O exchange in the myelinated nerve of the frog," *Experientia*, vol. 33, pp. 192–194, 1977.

[23] R. S. Menon, M. S. Rusinko, and P. S. Allen, "Proton relaxation studies of water compartmentalization in a model neurological system," *Magn Reson Med*, vol. 28, pp. 264–274, 1992.

[24] S. Peled, D. G. Cory, S. A. Raymond, D. A. Kirschner, and F. A. Jolesz, "Water diffusion, T_2, and compartmentation in frog sciatic nerve," *Magn Reson Med*, vol. 42, pp. 911–918, 1999.

[25] K. Wachowicz and R. E. Snyder, "Assignment of the T_2 components of amphibian peripheral nerve to their microanatomical compartments," *Magn Reson Med*, vol. 47, pp. 239–245, 2002.

[26] R. S. Menon and P. S. Allen, "Application of continuous relaxation-time distributions to the fitting of data from model systems and excised tissue," *Magn Reson Med*, vol. 20, pp. 214–227, 1991.

[27] R. Harrison, M. J. Bronskill, and R. M. Henkelman, "Magnetization-transfer and T_2 relaxation components in tissue," *Magn Reson Med*, vol. 33, pp. 490–496, 1995.

[28] P. J. Gareau, B. K. Rutt, C. V. Bowen, S. J. Karlik, and J. R. Mitchell, "In vivo measurements of multi-component T_2 relaxation behaviour in guinea pig brain," *Magn Reson Imaging*, vol. 17, pp. 1319–1325, 1999.

[29] A. Dula, "Micro-anatomical characterization of central white matter using magnetic resonance imaging," in *Biomedical Engineering*, vol. Ph.D. Nashville, TN: Vanderbilt University, 2008, pp. 111.

[30] G. J. Stanisz and R. M. Henkelman, "Diffusional anisotropy of T_2 components in bovine optic nerve," *Magn Reson Med*, vol. 40, pp. 405–410, 1998.

[31] G. Stanisz, A. Kecojevic, M. Bronskill, and R. Henkelman, "Characterizing white matter with magnetization transfer and T_2," *Magn Reson Med*, vol. 42, pp. 1128–1136, 1999.

[32] I. Bonilla and R. E. Snyder, "Transverse relaxation in rat optic nerve," *NMR Biomed*, vol. 20, pp. 113–120, 2007.

[33] T. J. Andrews, M. T. Osborne, and M. D. Does, "Diffusion of myelin water," *Magn Reson Med*, vol. 56, pp. 381–385, 2006.

[34] I. Ronen and D. Kim, "Compartment-specific q-space analysis of diffusion-weighted data from isolated rhesus optic and sciatic nerves," *Magn Reson Imaging*, in press.

[35] A. Purea and A. G. Webb, "Reversible and irreversible effects of chemical fixation on the NMR properties of single cells," *Magn Reson Med*, vol. 56, pp. 927–931, 2006.

[36] T. Watanabe, R. Tammer, S. Boretius, J. Frahm, and T. Michaelis, "Chromium(VI) as a novel MRI contrast agent for cerebral white matter: Preliminary results in mouse brain in vivo," *Magn Reson Med*, vol. 56, pp. 1–6, 2006.

[37] I. M. Vavasour, K. P. Whittall, D. K. Li, and A. L. MacKay, "Different magnetization transfer effects exhibited by the short and long T_2 components in human brain," *Magn Reson Med*, vol. 44, pp. 860–866, 2000.

[38] T. A. Bjarnason, I. M. Vavasour, C. L. Chia, and A. L. MacKay, "Characterization of the NMR behavior of white matter in bovine brain," *Magn Reson Med*, vol. 54, pp. 1072–1081, 2005.

CHAPTER II

GENERAL NMR THEORY AND METHODS

Overview of NMR [1]

NMR arises from an interaction between certain nuclei and externally applied magnetic fields**.** In an NMR experiment, this interaction is exploited to create signal characteristic of these nuclear species. While each nuclear particle possesses spin angular momentum **J** and a magnetic dipole moment **μ**, all nuclei are not available for study *via* NMR. This is because nuclear particles of the same kind tend to pair up so that their spins and dipole moments cancel out. Therefore, only nuclei with unpaired particles, or an odd number of protons and/or neutrons, are available. Spin ½ hydrogen (^{1}H) nuclei, specifically associated with water molecules, were studied herein because of the natural abundance of water in tissue. As a result, the discussion below will be limited to ^{1}H nuclei, or so-called proton spins.

When placed in an external static magnetic field $\mathbf{B}_0$, nuclei tend to align their dipole moments parallel (defined as the positive *z*-axis) or anti-parallel (defined at the negative *z*-axis) to the direction of the applied field. The parallel state is of slightly lower energy; therefore, slightly more dipole moments tend to align in this direction. Because they possess spin angular momentum and a dipole moment, these nuclei also experience a torque. This causes the dipole moments to precess about the applied field according to

$$\frac{d\boldsymbol{\mu}}{dt} = \gamma \frac{d\mathbf{J}}{dt} = \gamma \left(\boldsymbol{\mu} \times \mathbf{B}_0 \right). \tag{2.1}$$

where γ represents the gyromagnetic ratio, a constant intrinsic to each proton or nucleus ($2\pi \times 4.26$ kHz/Gauss for ^{1}H). For a given nucleus, the frequency of this precession ω_0, or resonant frequency, can be related to the magnitude of the static magnetic field by the Larmor relationship

$$\omega_0 = \gamma B_0 \tag{2.2}$$

where $B_0 = |\mathbf{B}_0|$. The local magnetic field is also modulated by its local molecular environment, or more specifically its local electronic structure. This results in slightly different resonant frequencies for different molecular environments, which can be described *via* the chemical shift σ

$$\omega_0 = \gamma B_0 (1 - \sigma). \tag{2.3}$$

The resultant system can be visualized as two sets of cones: one set from dipole moments precessing about the positive *z*-axis and one set from dipole moments precessing about the negative *z*-axis. The observed bulk magnetization **M** is the sum of all dipole moments within the volume *V*

$$\mathbf{M} = \frac{1}{V} \sum_{\substack{\text{protons} \\ \text{in V}}} \boldsymbol{\mu}. \tag{2.4}$$

Assuming the dipole moments are uniformly distributed about each cone and slightly more dipole moments are aligned along the positive *z*-axis, **M** reduces to a single vector aligned along the positive *z*-axis. In other words, placing a sample in an external static magnetic field $\mathbf{B}_0$ produces a net magnetization **M** that is aligned along the direction of $\mathbf{B}_0$.

Combining Eqns. (2.1) and (2.4) yields the following equation of motion for the bulk magnetization

$$\frac{d\mathbf{M}}{dt} = \gamma\left(\mathbf{M} \times \mathbf{B}_{ext}\right) \tag{2.5}$$

for an arbitrary external magnetic field $\mathbf{B}_{ext}$. From this expression, it can be seen that the bulk magnetization does not precess when aligned along $\mathbf{B}_0$ (and $\mathbf{B}_{ext} = \mathbf{B}_0$). Signal cannot be measured by receiver coils when this is the case because they rely on the conversion of time-varying magnetic fluxes to current *via* Faraday's Law. Therefore, the bulk magnetization must be tipped away from $\mathbf{B}_0$ to create precession and a measurable signal. This can be achieved by applying an orthogonal magnetic field $\mathbf{B}_1$ (or RF pulse) that oscillates at a frequency equal to the resonant frequency ω_0 of the nucleus of interest. During the RF pulse, the bulk magnetization precesses about $\mathbf{B}_{ext} = \mathbf{B}_0 + \mathbf{B}_1$, tipping the bulk magnetization away from the *z*-axis through an angle

$$\theta = \gamma B_1 t_p \tag{2.6}$$

where $B_1 = |\mathbf{B}_1|$ and t_p is the length of the RF pulse. After the RF pulse is turned off, the bulk magnetization is no longer aligned along the direction of $\mathbf{B}_0$, resulting in a precession about $\mathbf{B}_0$ and a time-varying magnetic flux that can be detected by receiver coils.

Often times it is convenient to decompose the bulk magnetization vector into components that are parallel and perpendicular to the *z*-axis. The parallel, or longitudinal, component is simply defined by *z*-component of the bulk magnetization vector M_z. The perpendicular, or transverse, component is defined in complex form as

$$M_{\perp} = M_x + iM_y . \tag{2.7}$$

This transverse component is often manipulated by applying additional magnetic field gradients

$$G_r = \frac{\partial B_z}{\partial r}, \tag{2.8}$$

which create a linear variation in the *z*-component of the magnetic field B_z along a given dimension *r*. In the presence of a field gradient, the total *z*-component of the magnetic field is defined as (neglecting chemical shift)

$$B_z(r) = B_0 + rG_r . \tag{2.9}$$

Recall, that the transverse magnetization precesses at a frequency defined by Eq. (2.2) when no field gradient is present. The addition of magnetic field gradients causes the transverse magnetization to precess according to

$$\omega(r) = \gamma(B_0 + rG_r), \tag{2.10}$$

resulting in a spatially dependent frequency of precession. Over time, this results in a spatially dependent phase, which can be visualized as a fanning out of individual spins in the complex transverse plane. The resultant phase dispersion $\Delta\phi$ across Δr can be expressed as

$$\Delta\phi(t) = \gamma\Delta r\int G_r(t)dt\,. \tag{2.11}$$

This phase dispersion is commonly exploited to selectively suppress unwanted signal components that can arise from imperfections in B_0 and B_1. The gradients used for this type of application are commonly referred to as crusher or spoiler gradients. The relationship between precession frequency and position established by gradients is also exploited (*via* the Fourier transform) in magnetic resonance imaging (MRI) to create images.

Relaxation [1, 2]

When placed in an external magnetic field, the bulk magnetization vector will eventually reach a state of thermal equilibrium along the longitudinal axis. The magnitude of magnetization in this state is referred to the equilibrium magnetization M_0. Application of an RF pulse perturbs the system away from equilibrium, creating in many cases coherent transverse magnetization that

can be detected by receiver coils. Following this perturbation, equilibrium is restored over time through a process known as relaxation, which arises from interactions between individual nuclei and their local molecular environment. Relaxation processes can be divided into two types: 1) spin-lattice relaxation (characterized by the rate constant $R_1 = 1/T_1$) is the process by which thermal equilibrium is restored following perturbation by an RF pulse and 2) spin-spin relaxation (characterized by the rate constant $R_2 = 1/T_2$) is the process by which coherent transverse magnetization is destroyed.

The local magnetic field experienced by a dipole is modulated in both direction and amplitude through interactions with neighboring dipoles. Random thermal motion, therefore, results in random fluctuations in the local magnetic field. The component of these random fluctuations that occurs at (or twice) the Larmor frequency is efficient at stimulating a spin-lattice relaxation. In addition to this component, spin-spin relaxation is also sensitive to low-frequency random fluctuations in the local magnetic field. Based upon the Larmor relationship, the process of spin-spin relaxation can be visualized as a fanning out (or dephasing) of individual spins in the transverse plane due to these random local field fluctuations. This process destroys coherent transverse magnetization because the bulk magnetization is the sum over these individual spins.

To account for relaxation, additional terms need to be added to Eq. (2.5). These resultant set of coupled ordinary differential equations is referred to as the Bloch equations

$$\frac{d\mathbf{M}}{dt} = \gamma\left(\mathbf{M} \times \mathbf{B}_{ext}\right) + R_1\left(M_0 - M_z\right)\hat{z} - R_2\mathbf{M}_{\perp}. \tag{2.12}$$

Assuming the signal is demodulated at the resonant frequency used for excitation ω_0, this can be rewritten in matrix form as

$$\frac{d\mathbf{M}}{dt} = \begin{pmatrix} -R_2 & \Delta\omega & -\omega_1 \sin\phi \\ -\Delta\omega & -R_2 & \omega_1 \cos\phi \\ \omega_1 \sin\phi & -\omega_1 \cos\phi & -R_1 \end{pmatrix} \begin{pmatrix} M_x \\ M_y \\ M_z \end{pmatrix} + \begin{pmatrix} 0 \\ 0 \\ R_1 M_0 \end{pmatrix} \tag{2.13}$$

where $\omega_1 = \gamma B_1$ is the frequency of precession about an applied RF pulse, ϕ is the corresponding RF phase in the transverse plane, and $\Delta\omega$ is the deviation from resonance. If we are concerned only with the rate of change of magnetization following an RF pulse ($\omega_1 = 0$) and assume we are on-resonance ($\Delta\omega = 0$), these equations can be decoupled

$$\frac{dM_z}{dt} = R_1 \left(M_0 - M_z \right) \tag{2.14}$$

$$\frac{dM_\perp}{dt} = -R_2 M_\perp \tag{2.15}$$

and solved

$$M_z(t) = M_0 - \left(M_0 - M_z(0) \right) e^{-tR_1} \tag{2.16}$$

$$M_\perp(t) = M_\perp(0) e^{-tR_2} . \tag{2.17}$$

These expressions describe the recovery and decay of longitudinal and transverse magnetization, respectively, due to relaxation.

Contrast Reagents [3]

Paramagnetic NMR contrast reagents can be used to increase the relaxation rates of neighboring water molecules. This increase in water relaxation rates arises from fluctuating local magnetic field created by unpaired electron spins in the paramagnetic contrast reagent. There are two main contributions to paramagnetic relaxation enhancement: 1) inner sphere contributions and 2) outer sphere contributions. Inner sphere contributions are due to the interactions between electron spins and water molecules in the first coordinate sphere of the contrast reagent, which is transferred to bulk water spins through chemical exchange. Outer sphere contributions arise from the fluctuating field experienced by bulk water spins as they diffuse near the paramagnetic contrast reagent. The observed relaxation rate $R_{1,2}^{obs}$ in the presence of a paramagnetic contrast reagent is linearly proportional to the concentration of reagent [CR] in the absence of exchange (i.e., in a homogeneous, well-mixed solution)

$$R_{1,2}^{obs} = R_{1,2}^{0} + r_{1,2}[CR] \tag{2.18}$$

where $R_{1,2}^{0}$ is the relaxation rate when no contrast reagent is present and $r_{1,2}$ is the correlation between reagent concentration and $R_{1,2}^{obs}$, or relaxivity.

A number of paramagnetic ions are capable of producing relaxation rate enhancement. Gadolinium [Gd(III)] has seven unpaired electrons, can be readily chelated (e.g., Gd-DTPA) to decrease its toxicity, and possesses a relatively long electron spin relaxation time (this increases the amount of time that coupling between electron spins in the contrast reagent and nuclear spins in the bulk solution can occur). These factors have lead to its widespread use clinically. More recently, potassium dichromate — the dichromate ion contains diamagnetic Cr(VI) — has

received some attention [4] as a potential white matter specific contrast reagent. This specificity is thought to arise due to reduction of diamagnetic Cr(VI) to paramagnetic chromium species [Cr(V) and/or Cr(III)] by oxidizable myelin lipids.

In Chapter VI, gadolinium and chromium will be investigated as potential compartment-specific contrast reagents. Using Eq. (2.18), the increase in relaxation rates (primarily R_1) associated with each contrast reagent will be used to estimate its compartmental distribution. One caveat that must be considered when making such an estimate is that relaxivity is not a constant, but is modulated by local macromolecular content [5]. As a result, compartmental differences in macromolecular content need to be considered when making these estimates.

Multiexponential T_2 [6]

As discussed in Chapter I, a number of tissues exhibit multiexponential T_2 (MET_2). In these tissues, the decay of transverse magnetization can no longer be described by solution to the Bloch equations, which only accounts for single component relaxation. MET_2 relaxation can, however, be described by extending these solutions to include multiple components

$$M_{\perp}(t) = \int_0^{\infty} s(T_2) \exp(-t / T_2) dT_2 \tag{2.19}$$

where $s(T_2)$ is the magnitude of the exponential component at relaxation time T_2. This integral equation falls into a class of equations known as Laplace transforms. Unfortunately, numerical inversion of Laplace transforms — determining $s(T_2)$ from the inverse Laplace transform (ILT)

of $M_{\perp}(t)$ — is an ill-posed problem. Despite this, stable inversion of MET_2 decay data is possible given adequate signal-to-noise ratio (SNR) and appropriate solution constraints.

The simplest method for numerically integrating Eq. (2.19) is to assume $s(T_2)$ is a sum of M delta functions

$$S(T_2) = \sum_{j=1}^{M} s_j \delta(T_2 - T_{2,j}) . \tag{2.20}$$

Substituting Eq. (2.20) into (2.19) yields

$$M_{\perp}(t) = m_i = \sum_{j=1}^{M} s_j e^{-t_i / T_{2,j}} \quad i = 1, 2, ..., N . \tag{2.21}$$

This can be expressed as a system of linear equations

$$\mathbf{m} = \mathbf{A}\mathbf{s} \tag{2.22}$$

where $\mathbf{m}$ ($N \times 1$) is a vector of measured echo magnitudes, $\mathbf{s}$ ($M \times 1$) is a vector of unknown exponential component amplitudes (or T_2 distribution), and $\mathbf{A}$ ($N \times M$) is a matrix of known decaying exponentials — a large number of exponential terms is typically assumed in order to adequately sample the T_2 domain — defined by

$$\mathbf{A} = \begin{pmatrix} e^{-t_1 T_{2,1}} & \cdots & e^{-t_1 T_{2,M}} \\ \vdots & \ddots & \vdots \\ e^{-t_N T_{2,1}} & \cdots & e^{-t_N T_{2,M}} \end{pmatrix}. \tag{2.23}$$

This system of equations can be solved by least-squares minimization of

$$\left\| \mathbf{As} - \mathbf{m} \right\|^2, \tag{2.24}$$

yielding the T_2 distribution (or T_2 spectrum).

As previously stated, additional constraints are needed to stabilize this inversion. Because the number of spins in a given compartment cannot be negative, nonnegative constraints are commonly incorporated *via* the nonnegative least-squares (NNLS) algorithm [7]. The NNLS algorithm is ideally suited for fitting MET_2 decay data because it requires no initial guesses and is guaranteed to converge. Furthermore, the nonnegative constraints are implicit in the algorithm and, therefore, need not be included as extra rows in **A**.

The NNLS algorithm tends to return T_2 distributions with a few isolated delta functions. However, a number of systems (e.g., myelinated tissue) are better characterized by continuous T_2 distributions. Fortunately, one can incorporate regularization constraints into the NNLS algorithm (as additional rows in **A**) to obtain such distributions. Commonly used regularization constraints include minimization of the squared amplitude of the T_2 spectrum (or "energy")

$$\sum_{j=1}^{M} s_j^2 \tag{2.25}$$

or the squared second-derivative of the T_2 spectrum (or "curvature")

$$\sum_{j=1}^{M-2} \left| s_{j+2} - 2s_{j+1} + s_j \right|^2 . \tag{2.26}$$

These constraints are then weighted against least-squares constraints by a term known as the regularizer. As the regularizer term approaches zero, the least-squares constraint dominates and spectra with isolated delta functions are obtained. As the regularizer term is increased, smoother spectra that are less sensitive to noise are obtained at the cost of data misfit. The optimal regularizer value is often deemed to be the value that results in a given percent increase in χ^2 misfit (typically 1–2%) relative to the unregularized, least-squares solution [8].

This process is demonstrated in Fig. 2.1 for a typical white matter decay curve with two components: 1) a short-lived component with a T_2 = 20 ms that represents 20% of the signal

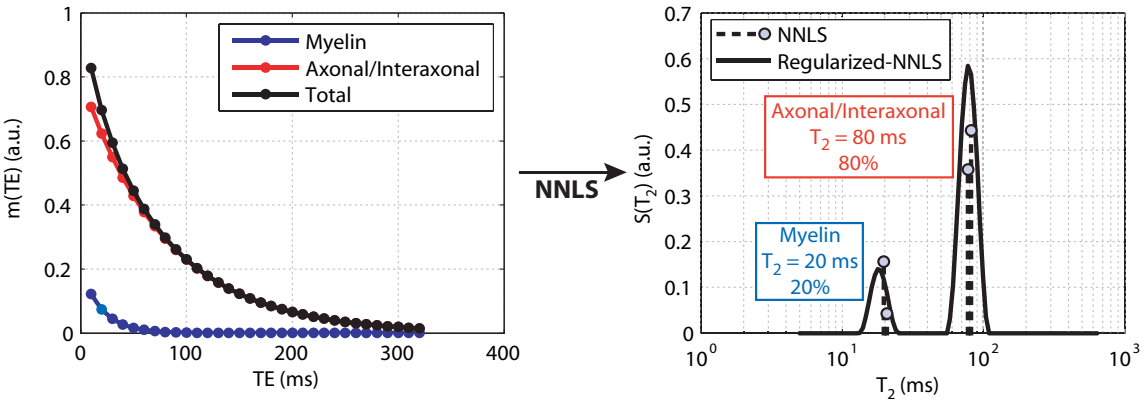

Fig 2.1. Sample MET_2 decay (left) and corresponding T_2 distribution (right) from white matter. The biexponential decay is decomposed into components representing myelin water and axonal/interaxonal water. Adding constraints to regularize the solution results in a smooth spectrum that is less sensitive to noise at the cost of data misfit. Note, the T_2 distributions are scaled in (b) for display purposes.

(assumed to represent myelin water) and 2) a long-lived component with a T_2 = 80 ms that represents the remaining signal fraction (assumed to represent axonal/interaxonal water). Note the two discrete components observed in the unregularized solution, which are replaced by smooth peaks in the regularized solution.

Acquiring T_2 Decay Data

The CPMG sequence [9] shown in Fig 2.2 is commonly used to acquire high fidelity T_2 decay data. By applying a series of refocusing (π) pulses at odd integers of a delay (τ = esp/2) and collecting signal at even integers of τ, signal loss due to B_0 inhomogeneities is refocused, forming a so-called spin-echo that decays according to T_2. Generally, sequences that apply a large number of RF pulses exhibit artifacts associated with B_0 and B_1 inhomogeneities. In the CPMG sequence, the relative phase of the excitation and refocusing pulses is designed to minimize this effect.

The multiple spin-echo sequence (Fig. 2.3) developed by Poon and Henkelman [10] is often used when one wishes to image the spatial distribution of T_2. Again, by applying a series of refocusing pulses at odd integers of a delay (τ) and collecting signal at even integers of τ, multiple echoes that decay according to T_2 can be acquired following a single excitation RF pulse. Unfortunately, the imaging

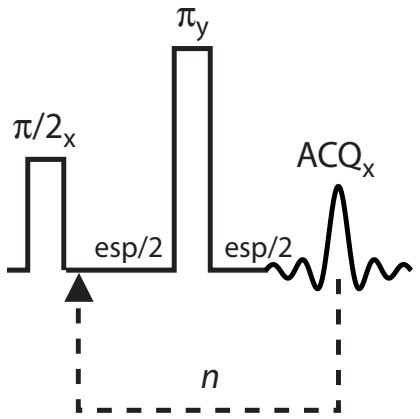

Fig. 2.2. Pulse sequence diagram for the CPMG sequence. The relative phase of the excitation (π/2) and refocusing (π) pulses is designed to reduce sensitivity to B_0 and B_1 inhomogeneities. esp = echo spacing; τ = esp/2; n = number of echoes.

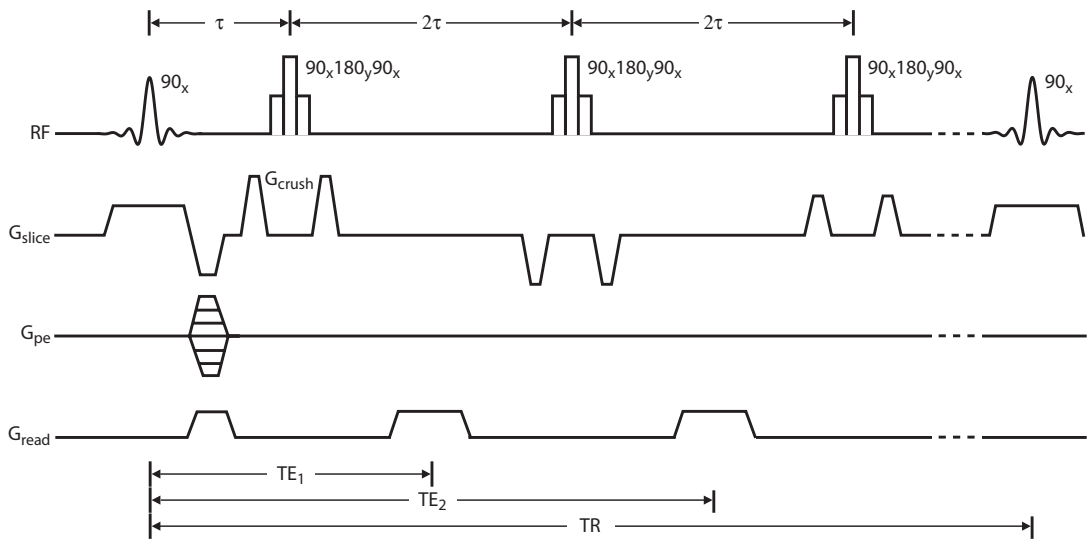

Fig 2.3. Pulse sequence diagram for a single-slice multiple spin-echo sequence. Only the first two echoes are shown; however, typically 32 echoes or more are acquired per excitation. Signal is acquired at even integers of τ such that the signal decays according to T_2. The combination of broadband composite refocusing pulses and crusher gradients placed about each refocusing pulse (in an alternating and descending fashion) serve to eliminate signal from unwanted coherence pathways (e.g., stimulated echoes).

gradients (specifically the phase encode gradients G_{pe} in Fig. 2.3) employed in this sequence render the CPMG phase cycling scheme ineffective in reducing artifacts associated with B_0 and B_1 inhomogeneities. Therefore, to minimize artifact contributions, $90_x180_y90_x$ broadband composite refocusing pulses [11] are applied between pairs of crusher gradients of alternating and descending magnitude [10]. The broadband composite pulses serve to correct for B_1 inhomogeneities, while the arrangement of crusher gradients is optimized to dephase any remaining signal from unwanted coherence pathways.

Integrated T_1–T_2 Experiments

In addition to T_2, quantitative measurement of compartmental T_1s is also of interest. Because of exchange between compartments, multiple T_1 components are often not observed in tissue, even in cases where multiple T_2 components are resolved. To get around this limitation, integrated T_1–

T_2 measurements, which are sensitive to the correlated T_1 and T_2 within a spin group [12-14], can be employed. One sequence used for acquiring T_1–T_2 data is the inversion recovery prepared CPMG (IR-CPMG) sequence shown in Fig 2.4. In this sequence, an inversion recovery preparation period, during which the magnetization undergoes T_1 relaxation, is added prior to the CPMG readout. By repeating the sequence over a range of inversion times, one can generate 2D T_1–T_2 data. Subtracting these data from thermal equilibrium (this ensures nonnegativity constraints are satisfied) results in a $I \times J$ data set that decays according to

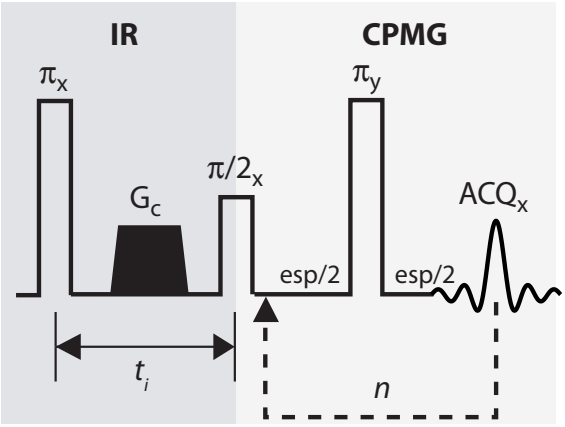

Fig. 2.4. Pulse sequence diagram for the IR-CPMG sequence used to acquire T_1–T_2 data. esp = echo spacing; t_i = inversion time; n = number of echoes in CPMG train; G_c = crusher gradient.

$$m_{ij} = 2\sum_{m=1}^{M}\sum_{n=1}^{N} s_{mn} e^{-\tau_i/T_{1,m}} e^{-t_j/T_{2,n}} \tag{2.27}$$

where τ_i and t_j are the inversion and echo times, respectively; and I and J are the total number of data points in the T_1 and T_2 dimension, respectively. These data can be reordered into a linear system of equations as defined in Eq. (2.20) where **m** is vector ($IJ \times 1$) of acquired T_1–T_2 data, **s** is a vector ($MN \times 1$) of unknown T_1–T_2 exponential component magnitudes, and **A** ($IJ \times MN$) is a matrix of known decaying T_1–T_2 exponential components. Once reordered, inversion of these data into the 2D relaxation time domain can be achieved using the same methods as described for T_2 data.

References

[1] E. M. Haacke, R. W. Brown, M. R. Thompson, and R. Venkatesan, *Magnetic Resonance Imaging: Physical Principles and Sequence Design*. New York: John Wiley and Sons, 1999.

[2] M. H. Levitt, *Spin Dynamics: Basics of Nuclear Magnetic Resonance*. New York: John Wiley and Sons, 2001.

[3] É. Tóth, L. Helm, and A. Merbach, "Relaxivity of MRI Contrast Agents," in *Contrast Agents I*, 2002, pp. 61–101.

[4] T. Watanabe, R. Tammer, S. Boretius, J. Frahm, and T. Michaelis, "Chromium(VI) as a novel MRI contrast agent for cerebral white matter: Preliminary results in mouse brain in vivo," *Magn Reson Med*, vol. 56, pp. 1–6, 2006.

[5] G. J. Stanisz and R. M. Henkelman, "Gd-DTPA relaxivity depends on macromolecular content," *Magn Reson Med*, vol. 44, pp. 665–667, 2000.

[6] K. P. Whittall and A. L. Mackay, "Quantitative Interpretation of NMR Relaxation Data," *J Magn Reson*, vol. 84, pp. 134–152, 1989.

[7] C. L. Lawson and R. J. Hanson, *Solving Least Squares Problems*. Englewood Cliffs, NJ: Prentice-Hall, 1974.

[8] S. J. Graham, P. L. Stanchev, and M. J. Bronskill, "Criteria for analysis of multicomponent tissue T_2 relaxation data," *Magn Reson Med*, vol. 35, pp. 370–378, 1996.

[9] S. Meiboom and D. Gill, "Modified spin echo method for measuring nuclear relaxation times," *Rev Sci Instrum*, vol. 29, pp. 688–691, 1958.

[10] C. S. Poon and R. M. Henkelman, "Practical T_2 quantitation for clinical applications," *J Magn Reson Imaging*, vol. 2, pp. 541–553, 1992.

[11] M. H. Levitt and R. Freeman, "Compensation for pulse imperfections in NMR spin-echo experiments," *J Magn Reson*, vol. 43, pp. 65–80, 1981.

[12] H. Peemoeller and M. M. Pintar, "Two-dimensional time-evolution approach for resolving a composite free-induction decay," *J Magn Reson*, vol. 41, pp. 358–360, 1980.

[13] A. E. English, K. P. Whittall, M. L. Joy, and R. M. Henkelman, "Quantitative two-dimensional time correlation relaxometry," *Magn Reson Med*, vol. 22, pp. 425–434, 1991.

[14] J. E. M. Snaar and H. Vanas, "A method for the simultaneous measurements of NMR spin-lattice and spin-spin relaxation times in compartmentalized systems," *J Magn Reson*, vol. 99, pp. 139–148, 1992.

CHAPTER III

NMR THEORY AND METHODS FOR MEASURING EXCHANGE RATES

In this chapter, expressions for the magnetization of an arbitrary *N*-pool exchanging system will be developed. These expressions will, in turn, be used to develop expressions for three different pulse sequences that can be used to extract exchange rates. Each approach will be discussed in this chapter and will be further tested and validated in Chapter IV.

Theory

Consider *N* exchanging pools (or compartments) of protons with the same chemical shift. Define unique equilibrium magnetizations M_0^i, spin-lattice relaxation rates R_1^i, and spin-spin relaxation rates R_2^i for each pool *i*. The rate of change in magnetization (during free precession) for this system can be expressed as a set of coupled ordinary differential equations, which are commonly referred to as the Bloch-McConnell equations [1, 2]. Using notation similar to that of Kimmich [3], these equations can be expressed as

$$\frac{d\mathbf{M}_{\perp}(t)}{dt} = \mathbf{L}_2\mathbf{M}_{\perp}(t) \tag{3.1}$$

$$\frac{d\mathbf{M}_{z}(t)}{dt} = \mathbf{L}_1\left[\mathbf{M}_{z}(t) - \mathbf{M}_0\right] \tag{3.2}$$

where $\mathbf{M}_\perp$, $\mathbf{M}_z$, and $\mathbf{M}_0$ are vectors ($N \times 1$) containing the transverse, longitudinal, and equilibrium magnetizations of each pool, respectively. The general solutions to these equations are

$$\mathbf{M}_\perp(t) = \exp\left(\mathbf{L}_2 t\right)\mathbf{M}_\perp(0) \tag{3.3}$$

$$\mathbf{M}_z(t) = \mathbf{M}_0 - \exp\left(\mathbf{L}_1 t\right)\left[\mathbf{M}_0 - \mathbf{M}_z(0)\right]. \tag{3.4}$$

Here, $\mathbf{L}_1$ and $\mathbf{L}_2$ are matrices ($N \times N$) defined as

$$\mathbf{L}_1 = -\mathbf{R}_1 + \mathbf{K} \tag{3.5}$$

$$\mathbf{L}_2 = -\mathbf{R}_2 + \mathbf{K} \tag{3.6}$$

where $\mathbf{R}_1$ and $\mathbf{R}_2$ are diagonal matrices ($N \times N$) containing the relaxation rates for each pool

$$\mathbf{R}_1 = \begin{pmatrix} R_1^i & \cdots & 0 \\ \vdots & \ddots & \vdots \\ 0 & \cdots & R_1^N \end{pmatrix};\ \mathbf{R}_2 = \begin{pmatrix} R_2^i & \cdots & 0 \\ \vdots & \ddots & \vdots \\ 0 & \cdots & R_2^N \end{pmatrix} \tag{3.7}$$

and $\mathbf{K}$ is a matrix ($N \times N$) of pseudo first-order exchange rates

$$\mathbf{K} = \begin{pmatrix} -\sum_{i \neq 1} k_{i1} & \cdots & k_{N1} \\ \vdots & \ddots & \vdots \\ k_{1N} & \cdots & -\sum_{i \neq N} k_{iN} \end{pmatrix}. \tag{3.8}$$

In Eq. (3.8), k_{ij} represents exchange from pool *i* to pool *j*. Assuming the system is in equilibrium, the forward and backward exchange rates between any two pools can be related using the principle of detailed balance

$$k_{ij}M_0^i = k_{ji}M_0^j. \tag{3.9}$$

These general solutions [Eqs. (3.3) and (3.4)] can be expanded in terms of the eigenvalues and eigenvectors of $\mathbf{L}_1$ and $\mathbf{L}_2$

$$\mathbf{M}_\perp(t) = \mathbf{U}_{L_2}\begin{pmatrix} \exp\left(\lambda_{L_2}^i t\right) & \cdots & 0 \\ \vdots & \ddots & \vdots \\ 0 & \cdots & \exp\left(\lambda_{L_2}^N t\right) \end{pmatrix}\mathbf{U}_{L_2}^{-1}\mathbf{M}_\perp(0) \tag{3.10}$$

$$\mathbf{M}_z(t) = \mathbf{M}_0 - \mathbf{U}_{L_1}\begin{pmatrix} \exp\left(\lambda_{L_1}^i t\right) & \cdots & 0 \\ \vdots & \ddots & \vdots \\ 0 & \cdots & \exp\left(\lambda_{L_1}^N t\right) \end{pmatrix}\mathbf{U}_{L_1}^{-1}\left[\mathbf{M}_0 - \mathbf{M}_z(0)\right]. \tag{3.11}$$

where $\lambda_{L_1}^i$ is the i^{th} eigenvalue of $\mathbf{L}_1$ and $\mathbf{U}_{L_1}$ is a matrix whose columns are the corresponding eigenvectors. Similar definitions apply for $\lambda_{L_2}^i$ and $\mathbf{U}_{L_2}$ with respect to $\mathbf{L}_2$.

From these solutions, it can be seen that the magnetization from each pool evolves as a sum of *N* exponentials whose rate constants are the eigenvalues of $\mathbf{L}_1$ and $\mathbf{L}_2$. From this point forward, we will refer these as the apparent relaxation rates $\tilde{R}_1^i = 1/\tilde{T}_1^i$ and $\tilde{R}_2^i = 1/\tilde{T}_2^i$. The observed NMR signal is the sum of magnetizations from the individual pools

$$M_{obs}(t) = \sum_{i=1}^{N} M_{\perp}^{i}(t); \tag{3.12}$$

therefore, the bulk signal also evolves as a sum of N exponentials according to the same apparent relaxation rates. To separate the observed NMR signal into components that represent the underlying pools, the inverse Laplace transform can be applied to T_2 decay data using the NNLS algorithm [4, 5] as described in Chapter II.

Methods

Based upon the above general solutions, one can derive expression for a given pulse sequence. Fitting data from the appropriate sequence to these expressions may allow one to invert the system and extract model parameters such as the exchange rates. In the following sections, the effect of exchange on CPMG data will first be discussed. Following this discussion, several examples of pulse sequences used for extracting exchange rates will be outlined. The two-pool system shown in Fig 3.1 will be used to demonstrate each approach. Unless otherwise specified,

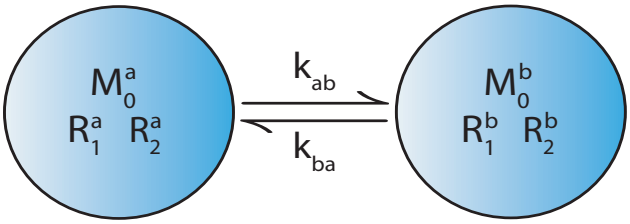

Fig. 3.1. Two pool model with pools *a* and *b*. Unique equilibrium magnetizations M_0^i and relaxation rates (R_1^i and R_2^i) are defined for each pool *i*. Exchange in each direction is defined *via* the exchange rates k_{ab} and k_{ba}.

the following model parameters will be used for these demonstrations: $R_1^a = 1.25\ \text{s}^{-1}$, $R_1^a / R_1^b = 2$, $R_2^a = 50\ \text{s}^{-1}$, $R_2^b = 12.5\ \text{s}^{-1}$, $M_0^a = M_0^b = 0.5$, and $k_{ab} = k_{ba} = 2\ \text{s}^{-1}$.

CPMG

The CPMG sequence shown in Fig. 2.2 is commonly used to acquire T_2 decay data, and inversion of these data can be used to separate signal arising from pools of different $\tilde{T}_2$. The extent to which the extracted T_2s and pool sizes reflect the underlying intrinsic values is dependent on the relative rate of exchange between these pools (Fig. 3.2). In the slow-exchange limit ($k_{ab} + k_{ba} << \left| R_2^a - R_2^b \right|$), the apparent T_2s and pool sizes accurately reflect the intrinsic

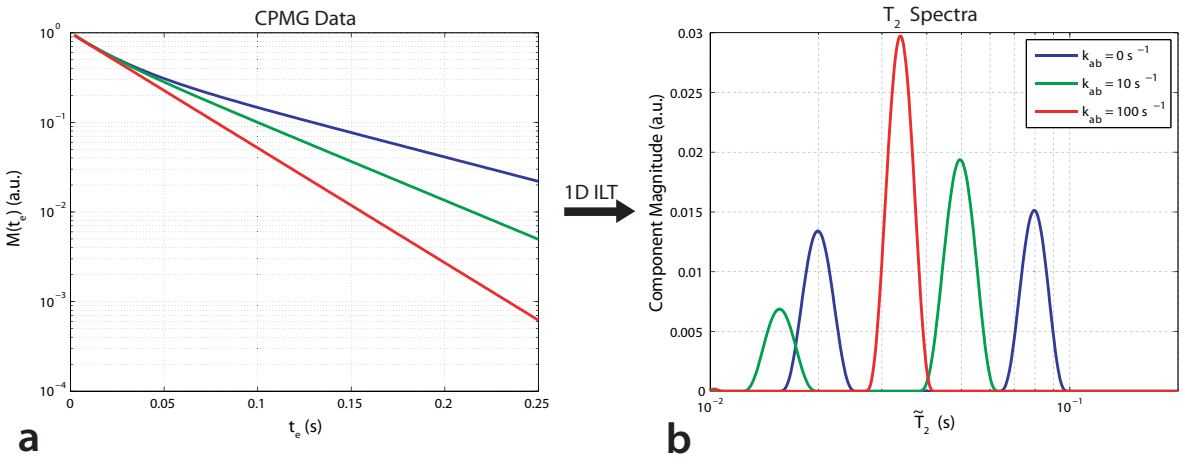

Fig. 3.2. CPMG data (a) and corresponding T_2 spectra (b) as a function of exchange rate (using the two-pool model in Fig. 3.1 and the model parameters in the text). When no exchange is present ($k_{ab} = 0\ \text{s}^{-1}$), the apparent T_2s and pool sizes reflect the intrinsic values. For intermediate exchange ($k_{ab} = 10\ \text{s}^{-1}$), the apparent T_2s are shifted to lower values. Also, the size of the short- and long-T_2 components are under- and overestimated, respectively. For fast exchange ($k_{ab} = 100\ \text{s}^{-1}$), only a single peak is observed, whose apparent $\tilde{R}_2 = M_0^a R_2^a + M_0^b R_2^b$ (assuming $M_0^a + M_0^b = 1$).

values. As the exchange rate increases, the apparent T_2 s are shifted to lower values, while the size of the short- and long-lived pools are under- and overestimated, respectively. In the fast-exchange limit ($k_{ab} + k_{ba} >> \left| R_2^a - R_2^b \right|$), only a single peak is observed, whose $\tilde{R}_2 = M_0^a R_2^a + M_0^b R_2^b$ (assuming $M_0^a + M_0^b = 1$). Using the eigen-expansion in Eq. (3.10), a general expression for the apparent pool sizes as a function of exchange rate can be derived

$$\tilde{\mathbf{M}}_0 = \left(\mathbf{U}_{L_2} \cdot \mathbf{1}_{N \times N} \right) \circ \left(\mathbf{U}_{L_2}^{-1} \mathbf{M}_0 \right)^T \tag{3.13}$$

where $\tilde{\mathbf{M}}_0$ is a vector ($N \times 1$) of apparent pool sizes, $\mathbf{1}_{i \times j}$ is a matrix or vector ($i \times j$) of ones, $\circ$ represents the element-wise (or Hadamard) matrix multiplication operation, $\cdot$ represents the dot product operation, and the superscript *T* represents the matrix transpose operation. Unfortunately, it is not possible to determine the exchange rates given the apparent pool sizes and T_2 s unless one of the independent model parameters is known. This is because we have five unknowns (R_2^a, R_2^b, M_0^a, M_0^b, and k_{ab}) and only four equations (two expressions each for the apparent pool sizes and T_2 s). Typically, we do not have knowledge of any of the intrinsic values; therefore, more complex, multi-dimensional experiments have been developed to extract exchange rates. Several examples are given in the following sections.

REXSY

One method for measuring exchange between pools of different $\tilde{T}_2$ is the 2D T_2–T_2 relaxation exchange spectroscopy (REXSY) pulse sequence shown in Fig. 3.3. This sequence was first suggested by Lee *et al.* [6] and has recently been used to investigate exchange in porous media

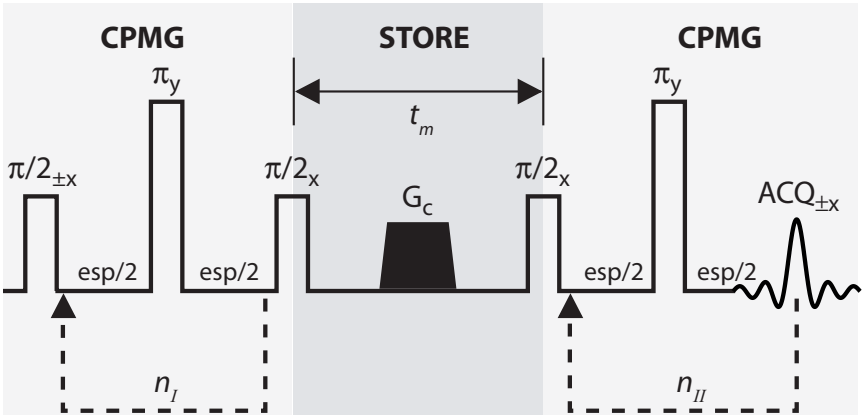

Fig. 3.3. Pulse sequence diagram for the REXSY sequence. esp = echo spacing; t_m = mixing time; n_I = number of refocusing pulses in 1st CPMG encoding dimension; n_{II} = number of refocusing pulses in 2nd CPMG encoding (or readout) dimension; G_c = crusher gradient.

[7-11]. The REXSY sequence consists of two CPMG pulse trains separated by a "mixing time" during which the magnetization is stored on the longitudinal axis. For a given mixing time, the number of refocusing pulses in the first CPMG period is arrayed, resulting in a 2D data set that decays according to $\tilde{T}_2$ in each dimension

$$M_{obs}(t_{e1},t_{e2}) = \iint s(\tilde{T}_2^{(I)},\tilde{T}_2^{(II)}) \exp\left(-t_{e1}/\tilde{T}_2^{(I)}\right) \exp\left(-t_{e2}/\tilde{T}_2^{(II)}\right) d\tilde{T}_2^{(I)} d\tilde{T}_2^{(II)} \qquad (3.14)$$

where $s(\tilde{T}_2^{(I)},\tilde{T}_2^{(II)})$ is the weight of each exponential term, or T_2–T_2 spectrum, and the roman numerals denote the 1st and 2nd CPMG encoding dimension. Inversion of Eq. (3.14) into a 2D T_2–T_2 spectrum can be achieved *via* 2D ILT methods [4, 5, 12]. As shown in Fig 3.4, spins that reside in the same compartment during each CPMG train will exhibit the same $\tilde{T}_2$ and will appear as diagonal peals in the resultant T_2–T_2 spectrum, while spins that exchange during the

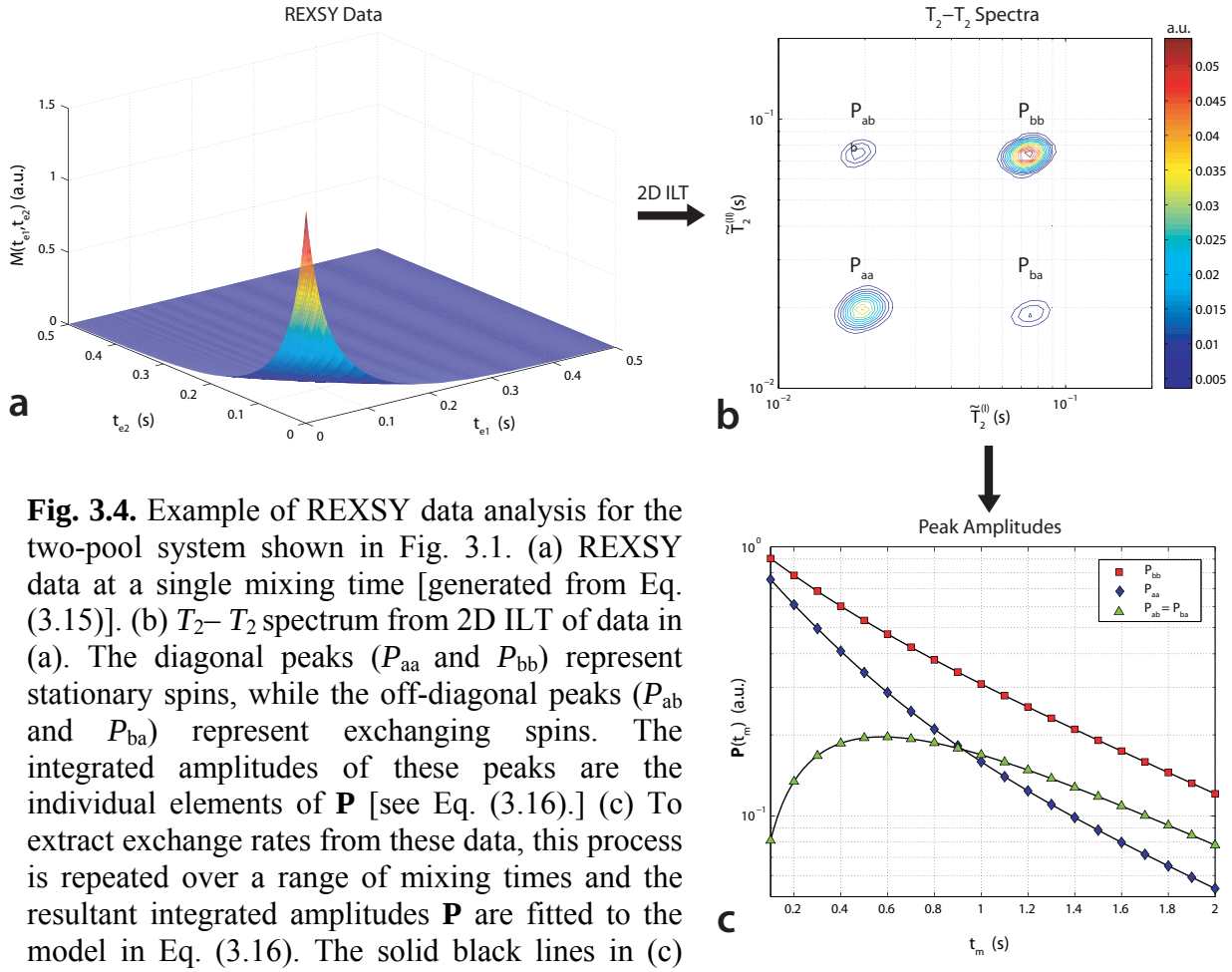

Fig. 3.4. Example of REXSY data analysis for the two-pool system shown in Fig. 3.1. (a) REXSY data at a single mixing time [generated from Eq. (3.15)]. (b) T_2– T_2 spectrum from 2D ILT of data in (a). The diagonal peaks (P_{aa} and P_{bb}) represent stationary spins, while the off-diagonal peaks (P_{ab} and P_{ba}) represent exchanging spins. The integrated amplitudes of these peaks are the individual elements of **P** [see Eq. (3.16).] (c) To extract exchange rates from these data, this process is repeated over a range of mixing times and the resultant integrated amplitudes **P** are fitted to the model in Eq. (3.16). The solid black lines in (c) represent this fit.

mixing time will exhibit different $\tilde{T}_2$ during each CPMG train and will appear as off-diagonal peaks in the resultant T_2–T_2 spectrum.

For a single mixing time, the T_2–T_2 spectrum allows one to qualitatively observe the exchange of spins between compartments of different $\tilde{T}_2$. In order to quantify the exchange rates, the experiment can be repeated over a range of mixing times, fitting the amplitude of the observed diagonal and off-diagonal spectral peaks to the appropriate model, which can be derived using the general solutions to the Bloch-McConnell equations above.

Assuming a two-part phase cycle, which subtracts magnetization that is stored on the -*z* axis during the mixing time from magnetization that is stored on the +z axis during the mixing time, the observed magnetization for each pool during the REXSY pulse sequence can be derived from Eqs. (3.3) and (3.4)

$$\mathbf{M}(t_{e1}, t_m, t_{e2}) = 2\exp\left(\mathbf{L}_2 t_{e1}\right)\exp\left(\mathbf{L}_1 t_m\right)\exp\left(\mathbf{L}_2 t_{e2}\right)\mathbf{M}_0 \tag{3.15}$$

where t_m is the mixing time, $t_{e1} = esp * n_I$ is the T_2-weighting duration in the 1st CPMG encoding dimension, and $t_{e2} = esp * n_{II}$ is the echo time in the 2nd CPMG encoding (or readout) dimension. Using the eigen-expansion in Eq. (3.10), this can be rewritten as a sum of exponential terms [as in Eq. (3.14)] of amplitude

$$\mathbf{P}(t_m) = 2\left(\mathbf{U}_{L_2}^{-1}\mathbf{M}_0\mathbf{1}_{1\times N}\right)\circ\left[\mathbf{1}_{N\times 1}\left(\mathbf{U}_{L_2}\cdot\mathbf{1}_{N\times N}\right)\right]\circ\left[\mathbf{U}_{L_2}^{-1}\exp\left(\mathbf{L}_1 t_m\right)\mathbf{U}_{L_2}\right]^T \tag{3.16}$$

where the diagonal elements of $\mathbf{P}$ ($N\times N$) contain the integrated peak amplitudes of the diagonal peaks in $s(\tilde{T}_2^{(I)}, \tilde{T}_2^{(II)})$ and the off-diagonal elements contain the integrated peak amplitudes of the off-diagonal peaks in $s(\tilde{T}_2^{(I)}, \tilde{T}_2^{(II)})$. In other words, $\mathbf{P}$ is an expression for the integrated peak amplitudes derived from 2D ILT of the REXSY data.

IR-CPMG

Extracting exchange rates from REXSY data requires a relatively long, 3D experiment (n_I x n_{II} x number of t_m). Another potential method for extracting exchange rates is based upon the 2D

inversion-recovery prepared CPMG (IR-CPMG) sequence shown in Fig. 2.4. The main advantage of this approach is that it potentially allows one to extract exchange rates from a 2D experiment (n x number of t_i), reducing acquisition time relative to the REXSY based approach.

Most commonly, this sequence is used to measure correlated T_1–T_2 [13]; however, it was recently proposed as a method for extracting exchange information [7]. It can be shown that, like REXSY data, 2D ILT of T_1–T_2 data results in spectra with off-diagonal peaks, which reflect exchange between compartments of different $\tilde{T}_2$. Unfortunately, the cross peaks are not all positive, which violates the nonnegativity constraint needed to robustly perform the 2D ILT. To get around this, we have developed a method based upon 1D ILT of the CPMG data (at each inversion time) that does not violate this constraint (see Fig. 3.5).

For a given inversion time, the IR-CPMG signal decays according to Eq. (2.19). Subtracting data from thermal equilibrium — this ensures that the nonnegative constraint of the 1D ILT method is met — the observed magnetization for each pool during the IR-CPMG pulse sequence can be derived from Eqs. (3.3) and (3.4)

$$\mathbf{M}(t_i, t_e) = 2\exp\left(\mathbf{L}_2 t_e\right)\exp\left(\mathbf{L}_1 t_i\right)\mathbf{M}_0 . \tag{3.17}$$

where t_i is the inversion time and t_e is the echo times for the CPMG readout. The eigen-expansion in Eq. (3.10) can be used to derive an expression for the peak amplitudes as a function of inversion time

$$\mathbf{P}(t_i) = 2\left(\mathbf{U}_{L_2} \cdot \mathbf{1}_{N\times N}\right) \circ \left\{\mathbf{U}_{L_2}{}^{-1}\exp\left(\mathbf{L}_1 t_i\right)\mathbf{M}_0\right\}^T . \tag{3.18}$$

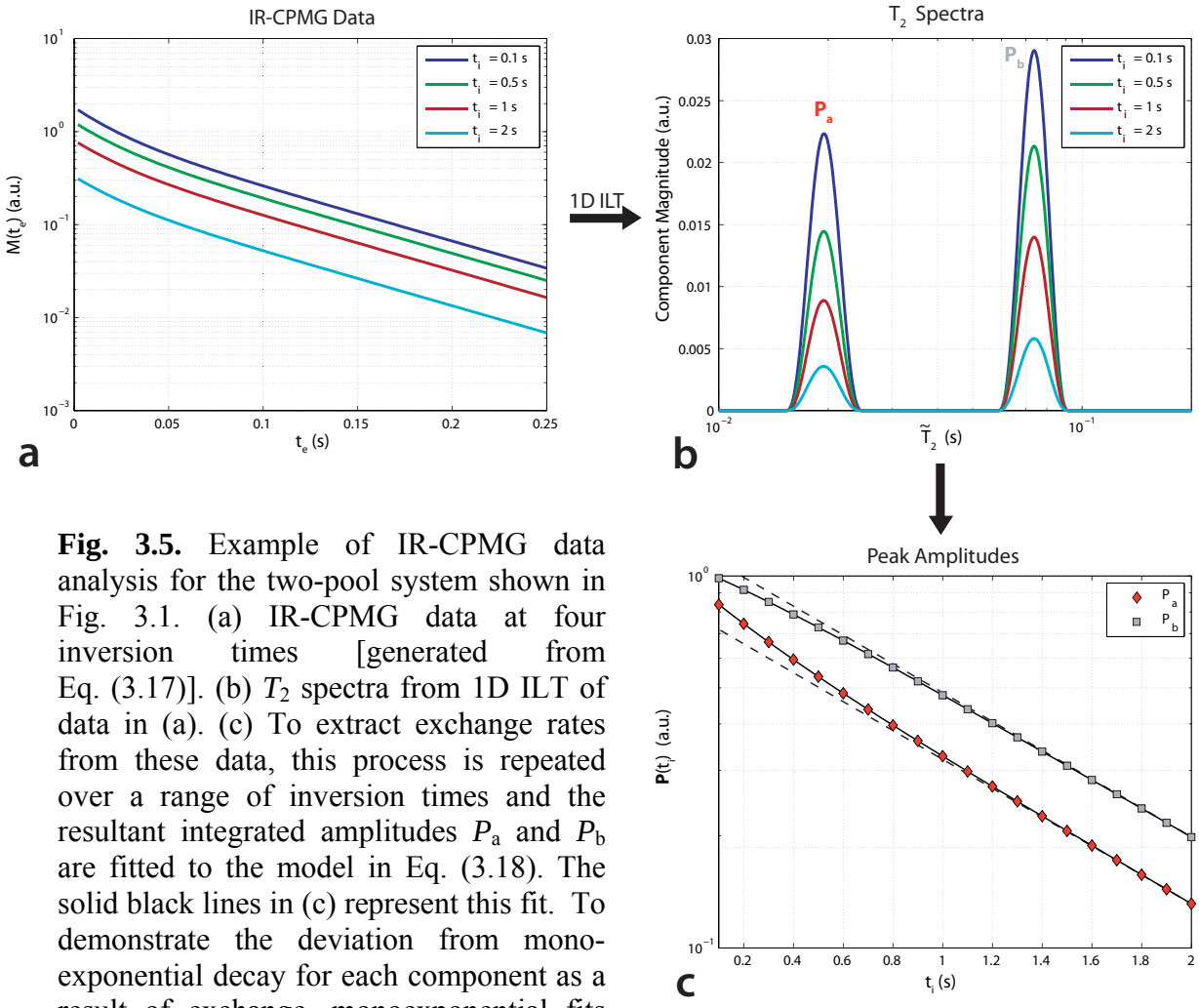

Fig. 3.5. Example of IR-CPMG data analysis for the two-pool system shown in Fig. 3.1. (a) IR-CPMG data at four inversion times [generated from Eq. (3.17)]. (b) T_2 spectra from 1D ILT of data in (a). (c) To extract exchange rates from these data, this process is repeated over a range of inversion times and the resultant integrated amplitudes P_a and P_b are fitted to the model in Eq. (3.18). The solid black lines in (c) represent this fit. To demonstrate the deviation from mono-exponential decay for each component as a result of exchange, monoexponential fits are also shown as dashed black lines

where $\mathbf{P}$ is a vector ($N \times 1$) of peak amplitudes.

For a two-pool system, it can be shown that one of the peak amplitudes evolves as the *difference* between two decaying exponentials as a function of inversion time (note the initial downward slope in P_b in Fig. 3.5c), while the other peak evolves as the *sum* of two decaying exponentials. One drawback, however, is that the exchange related component (short-T_1 component in Fig. 3.5c) is typically much smaller than other component(s), especially for slowly exchange systems. This results in high SNR demands to accurately fit the model [14, 15].

Furthermore, magnetization transfer (MT) between semi-solid and mobile protons can similarly effect the peak amplitudes of the liquid pools [16], making it difficult to uniquely identify intercompartmental exchange between mobile proton pools in cases where MT is present. In order to address these issues, we have developed a novel approach, which we call IR-REXSY.

IR-REXSY

The IR-REXSY sequence (Fig. 3.6) adds an inversion recovery preparation to the REXSY sequence in order to null one of the components based upon difference in compartmental R_1s. During the mixing time, this nulled component grows due to exchange with the non-nulled component(s). This allows one to uniquely identify intercompartmental exchange — MT will not result in any growth in the nulled component because t_{e1} is much longer than the T_2 of the macromolecular pool, resulting in a loss of coherence for this pool prior to the mixing period. Furthermore, though this inversion pulse suppresses signal from the non-nulled pool (dependent

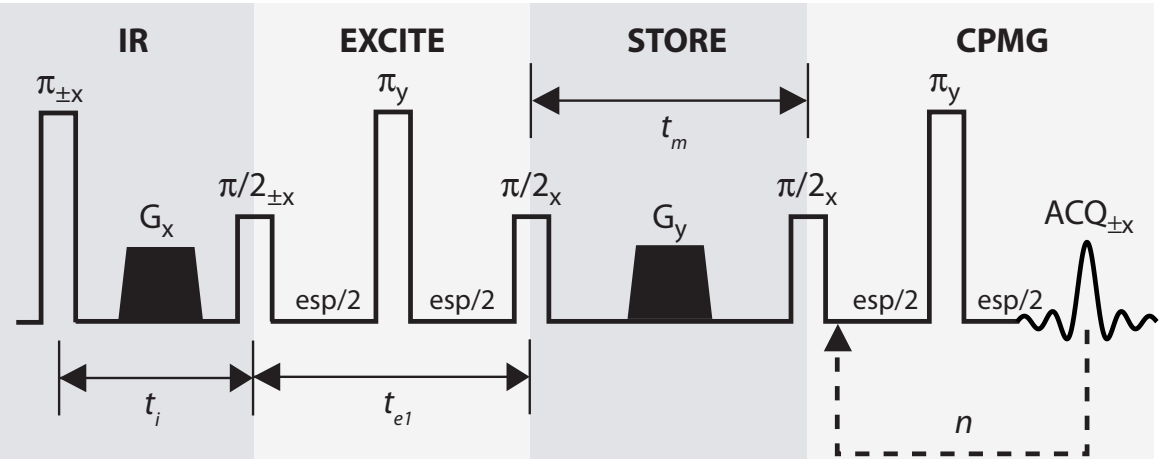

Fig. 3.6. Pulse sequence diagram for the IR-REXSY sequence. esp = echo spacing; t_m = mixing time; t_i = inversion time; t_{e1} = echo time prior to storage; n = number of refocusing pulses in CPMG readout; G_x = crusher gradient applied along x; G_y = crusher gradient applied along y.

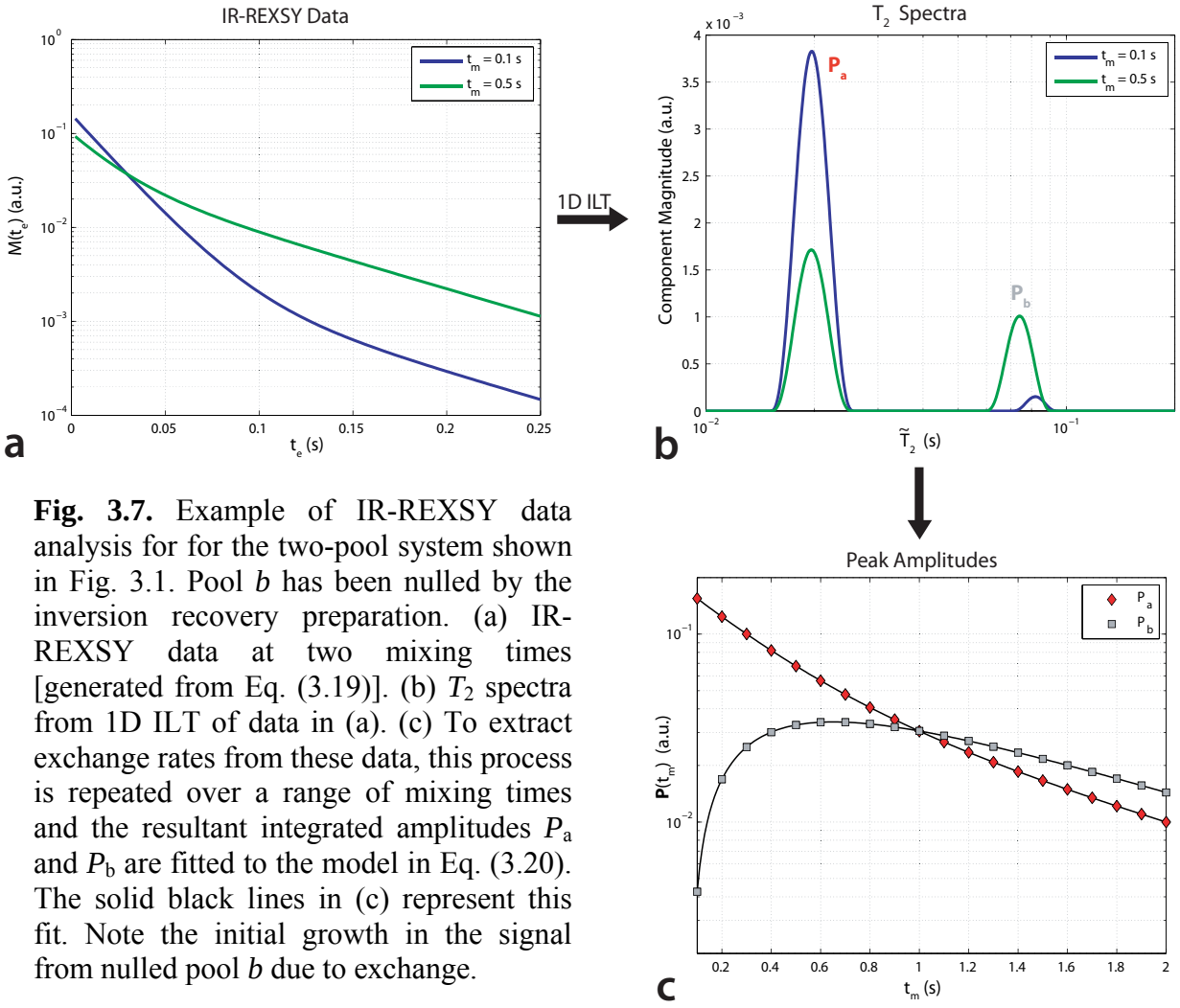

Fig. 3.7. Example of IR-REXSY data analysis for for the two-pool system shown in Fig. 3.1. Pool *b* has been nulled by the inversion recovery preparation. (a) IR-REXSY data at two mixing times [generated from Eq. (3.19)]. (b) T_2 spectra from 1D ILT of data in (a). (c) To extract exchange rates from these data, this process is repeated over a range of mixing times and the resultant integrated amplitudes P_a and P_b are fitted to the model in Eq. (3.20). The solid black lines in (c) represent this fit. Note the initial growth in the signal from nulled pool *b* due to exchange.

on the relative compartmental R_1s and the exchange rate), the resultant data may exhibit decreased SNR demands relative to the IR-CPMG approach. This is because much of the non-exchange related signal is filtered out using this approach.

The data analysis for the IR-REXSY sequence (see Fig. 3.7) is similar to that of the IR-CPMG sequence. For a given mixing time, the IR-REXSY signal decays according Eq. (2.19), which again can be inverted into a T_2 spectrum using 1D ILT methods. In the resultant T_2 spectrum, the peak representing spins from the nulled component will grow as a function of mixing time due to exchange with the other non-nulled component(s). Thus, by fitting the

amplitude of the observed spectral peaks as a function of mixing time to the appropriate model, one can extract exchange rates from IR-REXSY data.

Using the same two-part phase cycle used for the REXSY sequence, the observed magnetization for each pool during the IR-REXSY pulse sequence can be derived from Eqs. (3.3) and (3.4)

$$\mathbf{M}(t_i, t_{e1}, t_m, t_{e2}) = 2\exp\left(\mathbf{L}_2 t_{e2}\right)\exp\left(\mathbf{L}_1 t_m\right)\exp\left(\mathbf{L}_2 t_{e1}\right)\left[\mathbf{M}_0 - 2\exp\left(\mathbf{L}_1 t_i\right)\mathbf{M}_0\right]. \qquad (3.19)$$

Note that this two-part phase cycle is particularly important for the IR-REXSY sequence. This is because it ensures that the observed signal arises solely from spins that are excited by the first $\pi/2$ pulse — spins that are in the transverse place during the "Excite" period in Fig. 3.6 — and converts the T_1 recovery during the mixing time to a decay. This is important here, as any growth in the nulled component can be attributed directly to exchange. Once again, the eigen-expansion in Eq. (3.10) can be used to rewrite the expression as a sum of exponential terms of amplitude

$$\mathbf{P}(t_m, t_i) = 2\left(\mathbf{U}_{L_2} \cdot \mathbf{1}_{N\times N}\right) \circ \left\{\mathbf{U}_{L_2}{}^{-1}\exp\left(\mathbf{L}_1 t_m\right)\exp\left(\mathbf{L}_2 t_{e1}\right)\left[\mathbf{M}_0 - 2\exp\left(\mathbf{L}_1 t_i\right)\mathbf{M}_0\right]\right\}^T \qquad (3.20)$$

where $\mathbf{P}$ is a vector ($N \times 1$) of integrated peak amplitudes.

REFERENCES

[1] M. H. McConnell, "Reaction Rates by Nuclear Magnetic Resonance," *J Chem Phys*, vol. 28, pp. 430–431, 1958.

[2] J. R. Zimmerman and W. E. Brittin, "Nuclear magnetic resonance studies in multiple phase systems: lifetime of a water molecule in an absorbing phase of silica gel," *J Phys Chem*, vol. 61, pp. 1328–1333, 1957.

[3] R. Kimmich, *NMR: Tomography, Diffusometry, Relaxometry*. Berlin: Springer-Verlag, 1997.

[4] C. L. Lawson and R. J. Hanson, *Solving Least Squares Problems*. Englewood Cliffs, NJ: Prentice-Hall, 1974.

[5] K. P. Whittall and A. L. Mackay, "Quantitative Interpretation of NMR Relaxation Data," *J Magn Reson*, vol. 84, pp. 134–152, 1989.

[6] J. H. Lee, C. Labadie, C. S. Springer, and G. S. Harbison, "2-Dimensional Inverse Laplace Transform Nmr - Altered Relaxation-Times Allow Detection of Exchange-Correlation," *J Am Chem Soc*, vol. 115, pp. 7761–7764, 1993.

[7] P. J. McDonald, J. P. Korb, J. Mitchell, and L. Monteilhet, "Surface relaxation and chemical exchange in hydrating cement pastes: a two-dimensional NMR relaxation study," *Phys Rev E Stat Nonlin Soft Matter Phys*, vol. 72, pp. 011409, 2005.

[8] K. E. Washburn and P. T. Callaghan, "Tracking pore to pore exchange using relaxation exchange spectroscopy," *Phys Rev Lett*, vol. 97, pp. 175502, 2006.

[9] P. J. McDonald, J. Mitchell, M. Mulheron, L. Monteilhet, and J. P. Korb, "Two-dimensional correlation relaxation studies of cement pastes," *Magn Reson Imaging*, vol. 25, pp. 470–473, 2007.

[10] J. Mitchell, J. D. Griffith, J. H. Collins, A. J. Sederman, L. F. Gladden, and M. L. Johns, "Validation of NMR relaxation exchange time measurements in porous media," *J Chem Phys*, vol. 127, pp. 234701, 2007.

[11] L. Monteilhet, J. P. Korb, J. Mitchell, and P. J. McDonald, "Observation of exchange of micropore water in cement pastes by two-dimensional T(2)-T(2) nuclear magnetic resonance relaxometry," *Phys Rev E Stat Nonlin Soft Matter Phys*, vol. 74, pp. 061404, 2006.

[12] L. Venkataramanan, S. Yi-Qiao, and M. D. Hurlimann, "Solving Fredholm integrals of the first kind with tensor product structure in 2 and 2.5 dimensions," *IEEE Trans Signal Proc*, vol. 50, pp. 1017–1026, 2002.

[13] A. E. English, K. P. Whittall, M. L. Joy, and R. M. Henkelman, "Quantitative two-dimensional time correlation relaxometry," *Magn Reson Med*, vol. 22, pp. 425–434, 1991.

[14] F. R. Fenrich, C. Beaulieu, and P. S. Allen, "Relaxation times and microstructures," *NMR Biomed*, vol. 14, pp. 133–139, 2001.

[15] S. J. Graham, P. L. Stanchev, and M. J. Bronskill, "Criteria for analysis of multicomponent tissue T_2 relaxation data," *Magn Reson Med*, vol. 35, pp. 370–378, 1996.

[16] D. F. Gochberg, R. P. Kennan, and J. C. Gore, "Quantitative studies of magnetization transfer by selective excitation and T_1 recovery," *Magn Reson Med*, vol. 38, pp. 224–231, 1997.

CHAPTER IV

SIMULATION AND VALIDATION OF NMR EXCHANGE MEASUREMENTS

Introduction

Chapters III outlined the theory and methods for measuring intercompartmental exchange. In particular, two novel approaches (IR-CPMG and IR-REXSY) were presented, both of which reduce acquisition time compared to the existing REXSY approach. The goals of the studies presented in this chapter are: 1) to compare these three approaches in terms of their sensitivity to experimental noise and 2) to validate the two novel approaches in a model system. To compare approaches, Monte Carlo simulations were performed. To validate each approach, NMR measurements were performed in an aqueous urea [$(NH_2)_2CO$] model system. Aqueous urea contains two chemically distinct proton pools that are chemically shifted by approximately 1.1 ppm: 1) water protons (two per water molecule) and 2) urea protons (four per urea molecule). In the past, this system has been used to study chemical exchange [1-3]. It was chosen for this study because: 1) aqueous urea is biexponential (urea protons have a shorter T_2 than water protons because they are scalar coupled to fast relaxing quadrapolar ^{14}N spins [1]), 2) urea has a high solubility in water (allowing one to create solutions where 30% or more of the total proton signal arises from urea protons), 3) urea and water proton relaxation rates can be individually manipulated with contrast reagents [4], 4) proton exchange rates can be manipulated by altering pH and temperature [1], and 5) and the system is fully invertible from T_2 data alone because the pool sizes are known from the stoichiometry of the solution. The last of these is especially important as it serves as a "gold standard" against which each method can be compared.

Materials and Methods

Simulations

A two-pool system as shown in Fig. 4.1 was defined for all simulations. Each set of simulations required definition of 7 independent model parameters: R_1^a, R_1^b, R_2^a, R_2^b, M_0^a, M_0^b, and R_x. Here, R_x is the single parameter representation of the exchange rate [5], which must be weighted by the pool sizes in each direction to obtain the pseudo first-order exchange rates (e.g, $k_{ab} = R_x M_0^b$). These model parameters were varied using combinations of the following: R_1^a = 1.25 s^{-1}, R_1^a / R_1^b = {2, 1.5, 1.25}, R_2^a = 50 s^{-1}, R_2^b = 12.5 s^{-1}, M_0^a = {0.2, 0.5, 0.8}, M_0^b = {0.2, 0.5, 0.8}, and R_x = {0.5, 1, 2, 4, 8} $s^{-1} M_0^{-1}$.

For each combination of model parameters, data were generated for: 1) equilibrium CPMG 2) REXSY, 3) IR-REXSY, and 4) IR-CPMG pulse sequences. The REXSY, IR-REXSY, and IR-CPMG data were generated to compare different methods for measuring exchange, while the equilibrium CPMG data were used to constrain the fitting algorithm (see section *Data Analysis* for details). Equilibrium CPMG data were generated using Eq. (3.3), generating 500 echoes (n) at an echo spacing (*esp*) of 2 ms. These parameters were also used for the CPMG trains of the other sequences. REXSY data were generated using Eq. (3.15) at 32 t_m values linearly arrayed in 60 ms increments and at 24 T_2-weighting periods (t_{e1}) pseudo-logarithmically

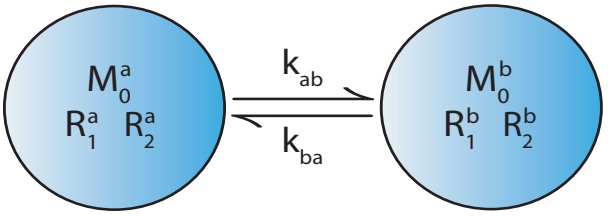

Fig. 4.1. Two-pool model (pools *a* and *b*) used for simulations. Equilibrium magnetizations and relaxation rates are defined for each pool. Exchange in each direction is defined *via* the exchange rates k_{ab} and k_{ba}. The same model applies for urea, assigning pool *a* to urea protons and pool *b* to urea water protons.

arrayed from 2 to 500 ms. IR-REXSY data were generated using Eq. (3.19) at the same t_m values with t_{e1} = 2 ms. Two sets of IR-REXSY data were generated, one in which pool *a* was nulled and one in which pool *b* was nulled. The t_i required to null each component was determined numerically [using Eq. (3.19)]. IR-CPMG data were generated using Eq. (3.17) at 32 t_i values linearly arrayed in 60 ms increments.

For each set of simulated data, 1000 Monte Carlo trials were performed. Gaussian noise was added to the simulated data at each trial with a signal-to-noise ratio (SNR) of 2000 — SNR is defined as the sum of the equilibrium magnetization divided by the standard deviation of the noise. Note, the SNR is defined relative to the equilibrium magnetization; therefore, the effective SNR of IR-REXSY will be much lower than the REXSY or IR-CPMG data due to the inversion recovery preparation at the beginning of the IR-REXSY sequence. Simulated noisy data were then fitted to the appropriate model (see *Data Analysis* for details) to extract model parameters. The SNR for each fitted parameter — defined as the expected parameter value divided by the standard deviation in the fitted value across trials — was then used to compare the three methods.

Urea Phantom Studies

Phantom Preparation

A 7-molal urea stock solution was prepared, yielding a ratio of 20/80% for urea/water protons. Urea and water proton relaxation rates were adjusted by addition of approximately 0.2 mM Gd-DTPA (Magnvist®; Berlex, Inc.) and 1 μg/mL $FeO_{1.44}$ (Ferodex®; Berlex, Inc.) [4], resulting in a model with relaxation rates similar to values observed in tissue ($R_1 / R_2 \approx 1/10$). The solution

was then buffered with approximately 10 mM phosphate buffer, titrated to a pH of 8 with NaOH, and transferred (50 μL) to 5-mm NMR tubes.

NMR

NMR measurements were made at bore temperature (≈20˚C) using a 300 MHz, 16-cm bore Varian Inova (Varian Inc., Palo Alto, CA) spectrometer equipped with imaging gradients capable of generating 27 G/cm with switching times to full amplitude of 100 μs. An in-house-built loop-gap resonator (10 mm in diameter, 20 mm long) was used for RF transmission and reception.

Data were collected for: 1) equilibrium CPMG 2) REXSY, 3) IR-REXSY, and 4) IR-CPMG pulse sequences. CPMG data were collected using a 1-ms *esp*, 1024 n, a 15-s predelay to ensure thermal equilibrium before each inversion pulse, and four averaged excitations (NEX). The same CPMG readout parameters and predelay values were used for all other experiments. REXSY data were collected at 30 t_m values linearly arrayed in 50 ms increments and 24 T_2-weighting periods (t_{e1}) pseudo-logarithmically arrayed from 2 to 512 ms. IR-REXSY data were collected using the same t_m values with t_{e1} = 2 ms. The t_i was experimentally determined — from IR-CPMG data using the approach described in [6] — to null water proton signal. REXSY and IR-REXSY sequences were repeated twice (NEX = 2) to accompany the two-part phase cycle described in Chapter III. In order to correct for presumed phase instabilities in our system, signed magnitude data (with the sign determined from the relative phase of the data) were combined instead of the raw complex data. This only had an affect on data acquired at longer mixing times, where the difference in magnitude for data stored on the ± *z*-axis is small. IR-CPMG data were collected at 24 t_i values logarithmically arrayed from 50 ms to 3.5 s and NEX = 4.

Data Analysis

Determining apparent relaxation times and pool fractions

For equilibrium CPMG data (both simulated and experimental), the apparent relaxation times $\tilde{T}_2^i$ and pool sizes $\tilde{M}_0^i$ for each pool *i* were first determined by fitting equilibrium CPMG data to the following biexponential model (with constant offset term *C*)

$$M_{obs}(t_e) = \tilde{M}_0^a \exp\left(-t_e / \tilde{T}_2^a\right) + \tilde{M}_0^b \exp\left(-t_e / \tilde{T}_2^b\right) + C \tag{4.1}$$

in a nonlinear least-squares sense using the Levenberq-Marquardt algorithm [7, 8]. This nonlinear approach was chosen over linear ILT methods because the smoothing commonly employed to regularize the ILT operation can bias the resultant apparent relaxation times and pool sizes when the T_2 spectrum is better defined by two delta functions. These apparent values were then used to constrain subsequent fitting as described in the following sections.

Determining exchange rates from CPMG data in urea phantom

As previously stated, it is possible to invert the model from the apparent T_2 s and pool sizes in urea because the relative intrinsic pool sizes (20/80%) are known from the stoichiometry of the solution. To do this, numerically generated apparent T_2 s and pool sizes were simply fitted to the CPMG-derived experimental values in a nonlinear least-squares sense using the Levenberq-Marquardt algorithm. The apparent T_2 s were generated by calculating the eigenvalues of

$$\mathbf{L}_2 = \begin{pmatrix} -R_2^a - R_x M_0^b & R_x M_0^a \\ R_x M_0^b & -R_2^b - R_x M_0^a \end{pmatrix} \tag{4.2}$$

and apparent pool sizes were generated from Eq. (3.13). Given that M_0^a and M_0^b are known, this results in a system with only three independent unknowns (R_2^a, R_2^b, and R_x) and four equations (two expressions each for the apparent pool sizes and T_2 s).

Determining exchange rates from REXSY, IR-REXSY, and IR-CPMG data

The following data fitting procedures apply for both simulated and experimental data. REXSY data were 2D inverse Laplace transformed [Eq. (3.14)] at each mixing time, yielding T_2–T_2 spectra as a function of mixing time. A sparse 2×2 grid of exponentials terms with relaxation times $\tilde{T}_2^a$ and $\tilde{T}_2^b$ (derived from equilibrium CPMG data) were used for these fits. This eliminated the need to integrate the area under the peak amplitudes, which has previously been shown [9] to be a major source of uncertainty in this type of analysis. IR-REXSY decay data (at each mixing time) were fitted to Eq. (4.1) in a nonlinear least-squares sense using the Levenberq-Marquardt algorithm. IR-CPMG data were subtracted from thermal equilibrium (to convert the T_1 recovery into a decay), and T_2 decay data at each inversion time were fitted to Eq. (4.1) using the same approach. For these fits, data were fitted to exponentials with apparent relaxation times $\tilde{T}_2^a$ and $\tilde{T}_2^b$ as derived from the equilibrium CPMG data.

The resultant spectral amplitudes were then fitted to the appropriate model — Eq. (3.16), Eq. (3.20), or Eq. (3.18) — in a nonlinear least-squares sense using a subspace trust-region method [10, 11]. This method was chosen here because it was less sensitive to initial parameter guesses than more traditional approaches (e.g., Levenberq-Marquardt). During each iteration of

the optimization procedure, the current iteration's R_x was used in conjunction with the equilibrium CPMG-derived apparent T_2 s and pool sizes to numerically determine the current iteration's intrinsic T_2 s and pool sizes (using an analogous approach as described in *Determining exchange rates from CPMG data in urea phantom*). This effectively constrained these four parameters (R_2^a, R_2^b, M_0^a, and M_0^b), reducing the number of free parameters to three (R_1^a, R_1^b, and R_x). This fitting procedure is summarized in Fig. 4.2.

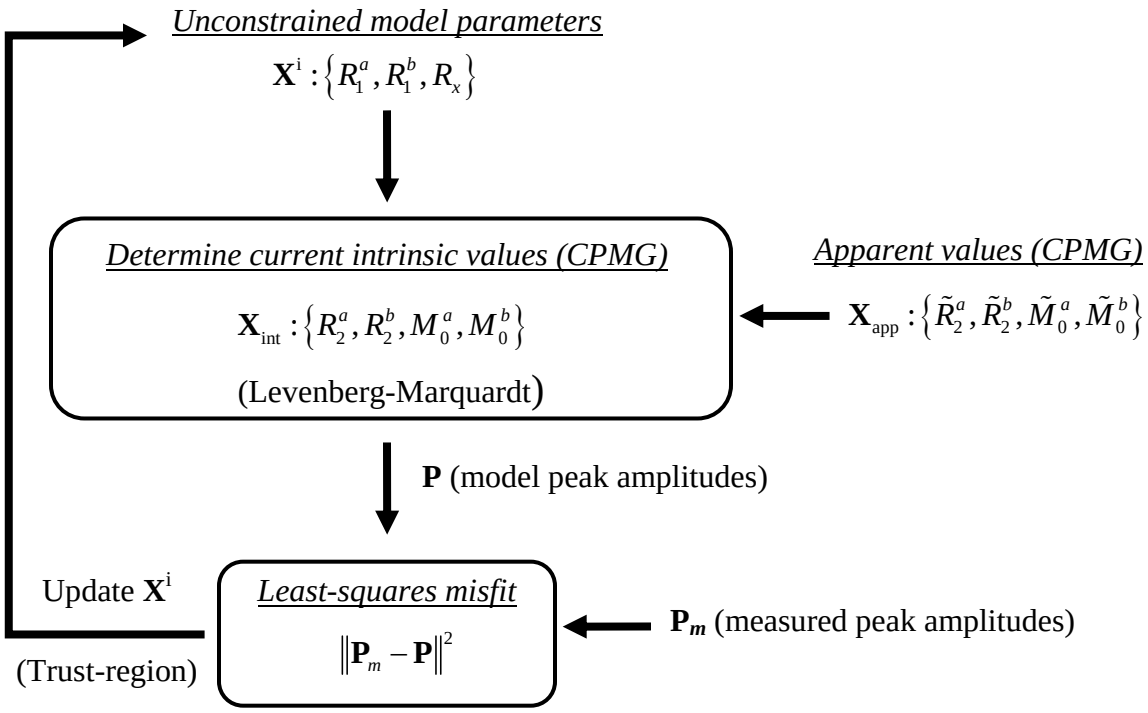

Fig. 4.2. Flowchart demonstrating the fitting procedure used for all methods (REXSY, IR-REXSY, and IR-CPMG). A trust-region method was used to minimize the least-squares misfit of measured and model peak amplitudes, yielding the exchange rate and spin-lattice relaxation rates for each site. During each iteration of this procedure, the current iteration's exchange rate was used in conjunction with the CPMG-derived apparent pool sizes and spin-spin relaxation rates to numerically determine the remaining model parameters.

Results and Discussion

Simulations

The SNR of the fitted exchange rates R_x as a function of R_x and R_1^a / R_1^b are summarized in Fig. 4.3 ($M_0^a = 0.2,\ M_0^b = 0.8$) and Fig. 4.4 ($M_0^a = M_0^b = 0.5$). An additional set of simulations was performed with $M_0^a = 0.8$ and $M_0^b = 0.2$. Results for these simulations were nearly identical to those given in Fig 4.3; therefore, they are not shown. Results are given for each for the following sequences: REXSY, IR-REXSY in which component *a* was nulled, IR-REXSY in which component *b* was nulled, and IR-CPMG. Qualitatively, the results shown in Figs. 4.3 and 4.4 are similar, with the results in Fig. 4.4 shifted to higher SNRs. This is consistent with previous analyses of multiexponential fitting [12, 13], which found that the uncertainty of the fitted parameters was smallest when the pool sizes were similar in magnitude. Because of these similarities, the following discussion should apply to any two-pool system, irrespective of the relative pool sizes.

As can be seen in Fig. 4.3 and 4.4, the IR-REXSY results were similar when component *a* or *b* was nulled. Therefore, for a two-pool system, the choice of which pool to null is mostly arbitrary [unless one is considering magnetization transfer (MT) as discussed in Chapter V]. Also, the SNR of the fitted exchange rate decreased (for the most part) as a function R_x and R_1^a / R_1^b. This can be attributed to a decrease in effective SNR with increasing R_x and R_1^a / R_1^b, resulting from increased suppression of the non-nulled component following the inversion recovery preparation. Interestingly, though the IR-REXSY signal has a lower effective SNR than the IR-CPMG signal, the resultant fitted parameters exhibit a higher relative SNR in many cases ($R_x \leq 4\ \mathrm{s}^{-1} M_0^{-1}$). This can be attributed to that fact that the inversion recovery preparation in the

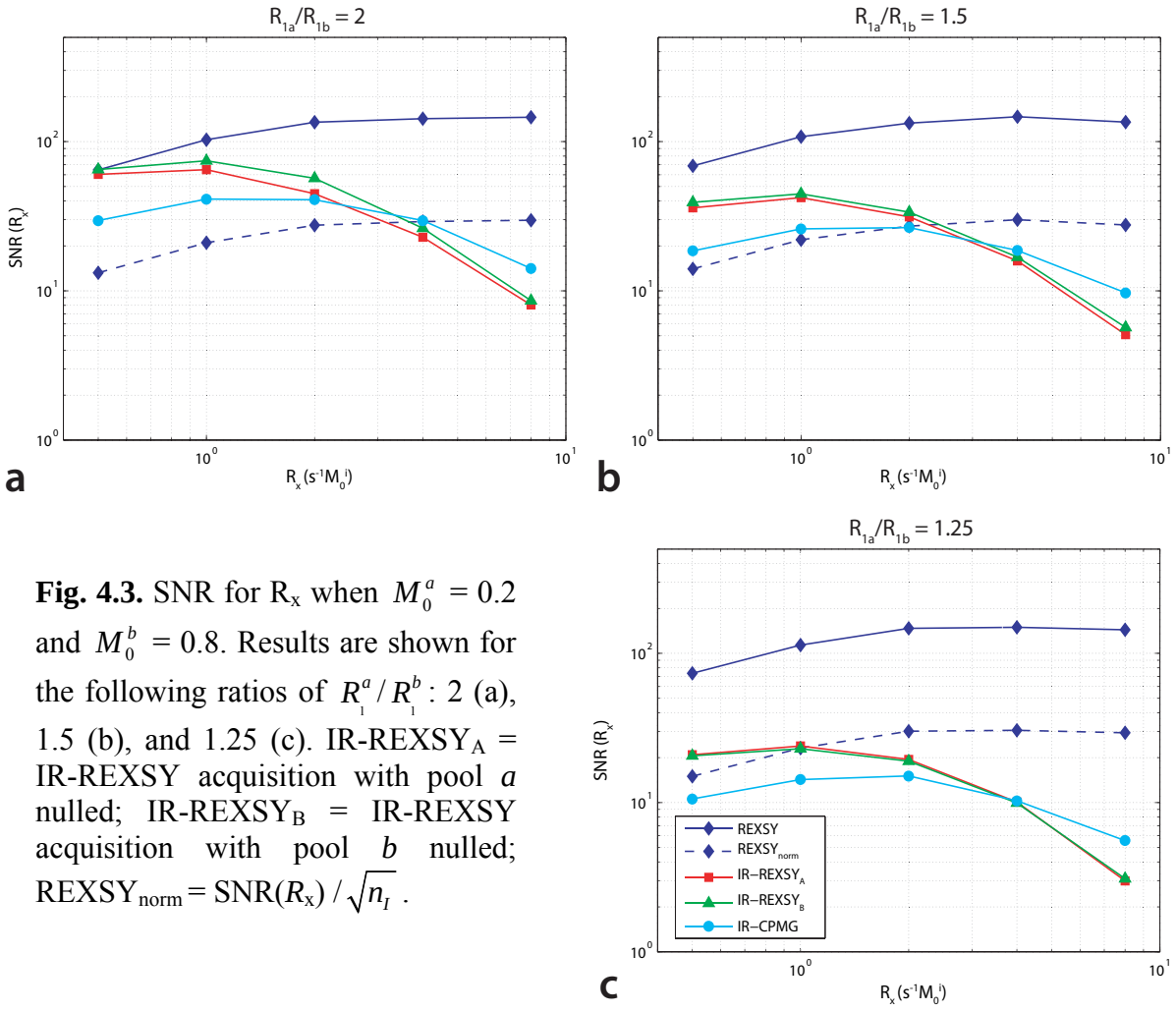

Fig. 4.3. SNR for R_x when $M_0^a = 0.2$ and $M_0^b = 0.8$. Results are shown for the following ratios of R_1^a / R_1^b: 2 (a), 1.5 (b), and 1.25 (c). IR-REXSY$_A$ = IR-REXSY acquisition with pool *a* nulled; IR-REXSY$_B$ = IR-REXSY acquisition with pool *b* nulled; $\text{REXSY}_{\text{norm}} = \text{SNR}(R_x) / \sqrt{n_I}$.

IR-REXSY sequence is designed to essentially filter out the non-exchange related signal, allowing one to directly fit signal related to exchange (much like fitting the off-diagonal peaks in REXSY-derived T_2–T_2 spectra).

For the REXSY sequence, the SNR of the fitted exchange rate increased (for the most part) as a function R_x. This can be attributed to a increase in relative off-diagonal amplitude with increasing R_x. Unlike IR-REXSY and IR-CPMG, REXSY results showed no dependence on R_1^a / R_1^b. REXSY outperformed the other techniques for nearly all R_x and R_1^a / R_1^b combinations.

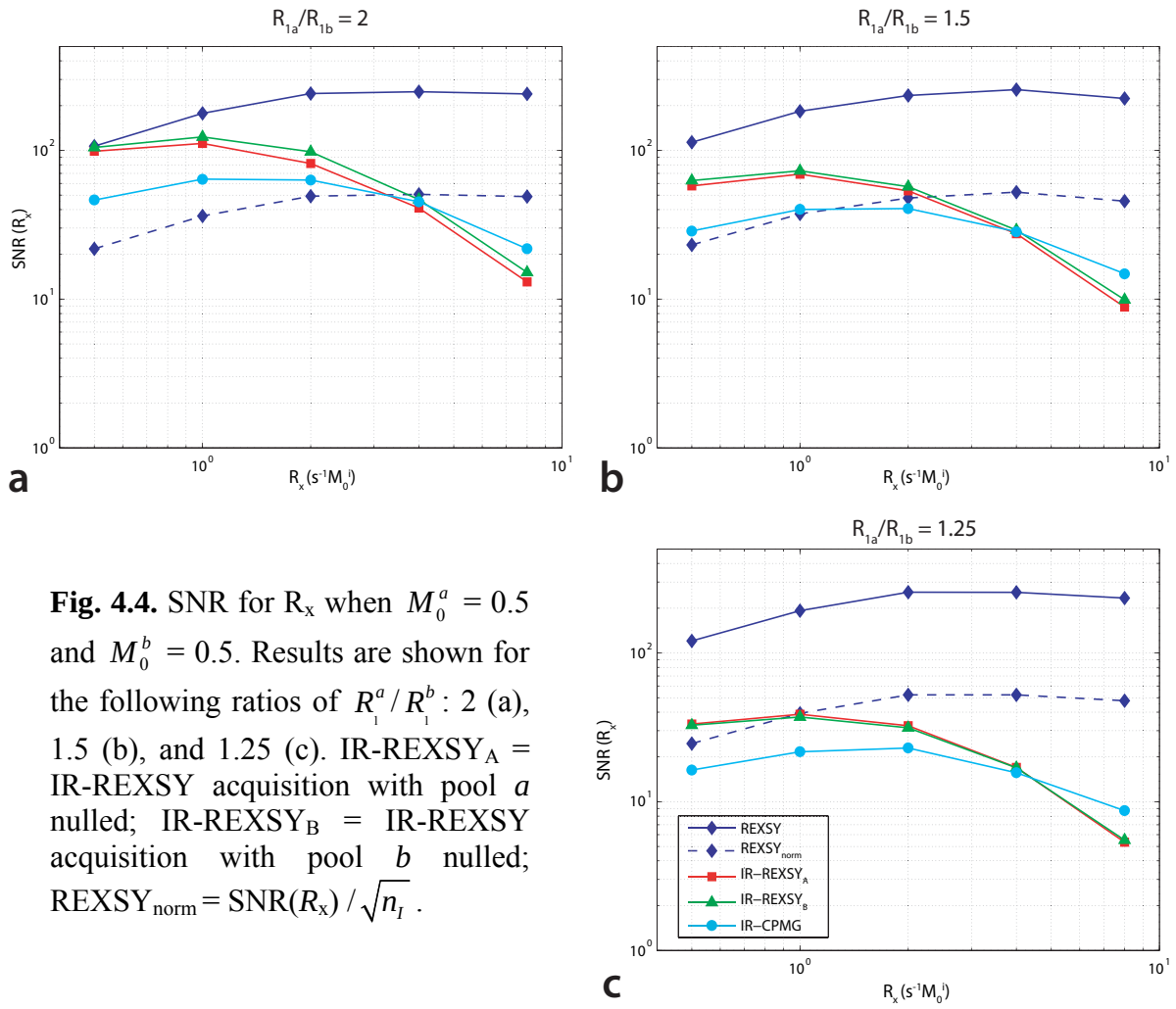

Fig. 4.4. SNR for R_x when $M_0^a = 0.5$ and $M_0^b = 0.5$. Results are shown for the following ratios of R_1^a / R_1^b: 2 (a), 1.5 (b), and 1.25 (c). IR-REXSY$_A$ = IR-REXSY acquisition with pool *a* nulled; IR-REXSY$_B$ = IR-REXSY acquisition with pool *b* nulled; $\text{REXSY}_{\text{norm}} = \text{SNR}(R_x) / \sqrt{n_I}$.

However, the acquisition time for the REXSY sequence is approximately n_I times longer than the acquisition time for the IR-REXSY and IR-CPMG sequences. Therefore, to compare these sequences in terms of SNR efficiency, plots of the $SNR / \sqrt{n_I}$ were also generated for REXSY data ($\text{REXSY}_{\text{norm}}$). When comparing these sequences with respect to SNR efficiency, REXSY outperforms the other techniques only when exchange is relatively fast and when the ratio of R_1^a / R_1^b is relatively low. Irrespective of the relative performance of these three approaches, both 2D approaches (IR-REXSY and IR-CPMG) perform quite well over most combinations of

R_x and R_1^a / R_1^b. In fact, for relatively slow to intermediate exchange rates ($R_x \leq 4\ s^{-1} M_0^{-1}$), these results suggest that we can fit the exchange rates with an uncertainty of less than 10%.

In choosing between the IR-REXSY and IR-CPMG approaches, one must consider several factors. First, IR-REXSY requires time to experimentally determine the optimal timings to null the component of choice. As a result, the total experimental time needed for the IR-CPMG approach is expected to be less than for IR-REXSY. Second, MT between semi-solid and mobile protons can effect the IR-CPMG peak amplitudes in a similar fashion to exchange between the liquid pools [14], making it difficult to uniquely identify intercompartmental exchange between mobile proton pools in cases where MT is present. For the IR-REXSY sequence, however, the nulled component can only grow due to exchange with the non-nulled component (for reasons described in Chapter III), allowing one to uniquely identify intercompartmental exchange. Third, higher-dimension (4D) REXSY experiments, can potentially be performed using the IR-REXSY approach. For example, Washburn *et al.* [15] proposed adding an additional dimension to the REXSY sequence, which they refer to as the propagator dimension. Essentially, this approach adds diffusion gradients on both sides of the mixing period, which are applied over a range of magnitudes. A q-space analysis [16] is then applied to the resultant REXSY data to determine the characteristic length-scale between exchanging pores. Adding this dimension to the IR-REXSY sequence could potentially allow one to collect these data using a 3D sequence, resulting in an approach with more manageable acquisition times compared to a 4D REXSY sequence.

Urea Phantom Studies

The SNR for the experimental urea data was $>10^4$. This was more than sufficient to reliably extract exchange rates from each model. Sample data and model fits acquired in aqueous urea are

given in Fig. 4.5 for each approach (REXSY, IR-REXSY, and IR-CPMG). The fitted parameter values are given in Table 4.1. Recall that inversion of CPMG data using the known solution stoichiometry (20/80% for urea/water protons) will be treated as the "gold standard" against which the other approaches will be compared. In order to obtain a measure of uncertainty, CPMG measurements were repeated four times over the course of the experiment, and the standard deviation in fitted parameter values across these acquisitions was computed. In order to obtain a measure of uncertainty for the other approaches, the 95% confidence interval was calculated based upon the nonlinear least squares model [17].

The exchange rates derived from each approach were in good agreement and were within 9%, 5%, and 6% of the exchange rates derived from the CPMG data and solution stoichiometry for the REXSY, IR-REXSY, and IR-CPMG approaches, respectively. The derived pool fractions and relaxation rates from each approach were also in good agreement, further validating each approach. Also, the general trend of experimental uncertainties in the fitted exchange rates — from lowest uncertainty to highest: REXSY, IR-REXSY, IR-CPMG — was in good agreement with the simulated data (see Fig. 4.3c, $R_x = 1\ s^{-1} M_0^{-1}$).

Table 4.1. Fittted model parameters for aqueous urea (pH 8.0). The uncertainties from inverting CPMG (using the known stoichiometry of the solution) were derived from the standard deviation across multiple acquisitions, while the uncertainties for the fitted parameters (R_1^a, R_1^b, and R_x) for REXSY, IR-REXSY, and IR-CPMG were based upon the 95% confidence interval of the nonlinear least-squares fit.

	$R_x\ (s^{-1}M_0^{-1})$	$R_1^a\ (s^{-1})$	$R_1^b\ (s^{-1})$	$R_2^a\ (s^{-1})$	$R_2^b\ (s^{-1})$	M_0^a	M_0^b
CPMG	1.03 (0.02)	–	–	17.04 (0.05)	5.00 (0.01)	0.2*	0.8*
REXSY	0.94 (0.02)	1.44 (0.02)	1.24 (0.01)	17.11	5.01	0.20	0.80
IR-REXSY	1.08 (0.07)	1.38 (0.01)	1.24 (0.01)	17.00	4.99	0.20	0.80
IR-CPMG	0.98 (0.14)	1.45 (0.01)	1.24 (0.01)	17.08	5.01	0.20	0.80

* Values known from urea solution stoichiometry.

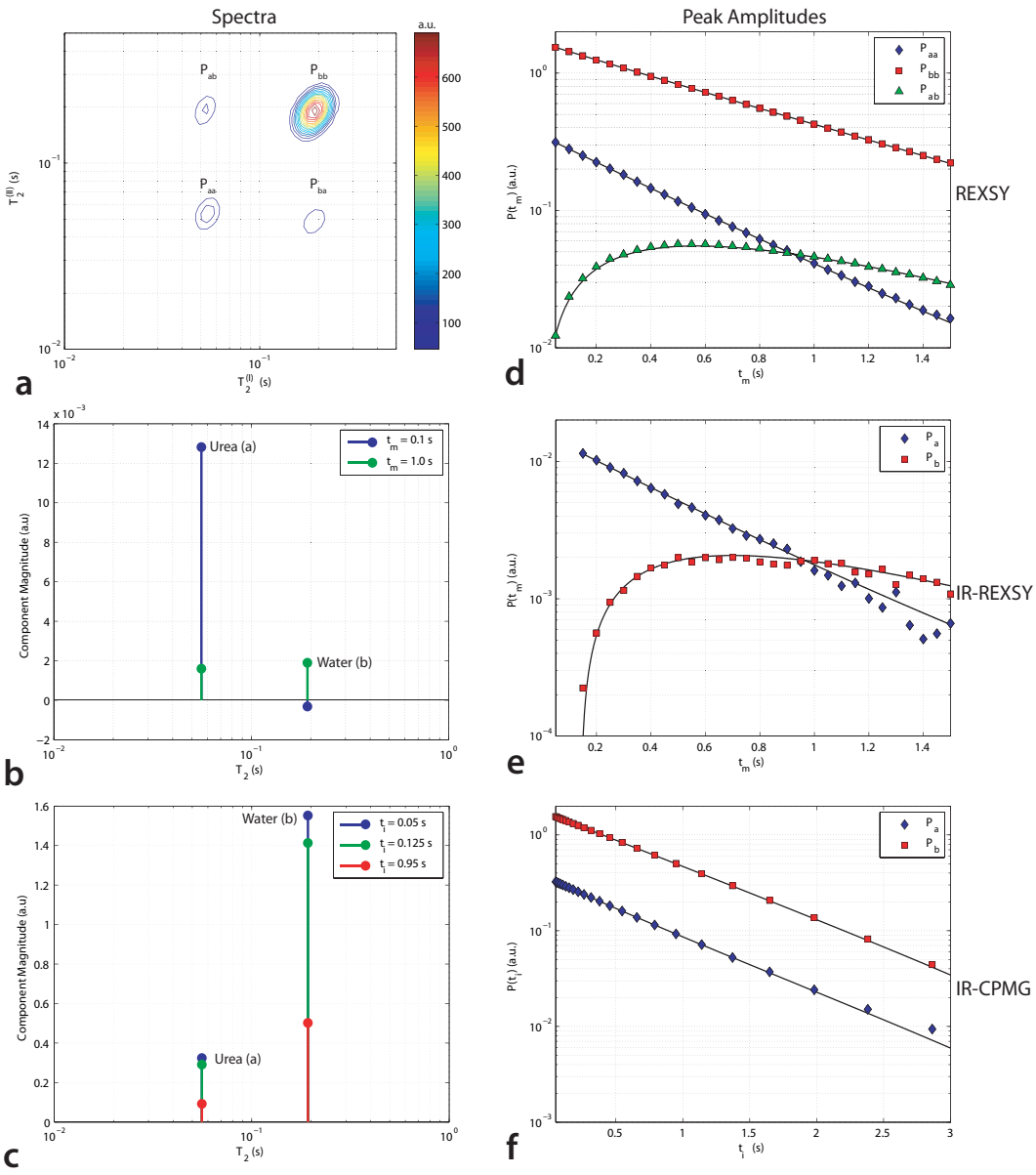

Fig. 4.5. Sample spectra (a–c) from urea data and corresponding spectral peak amplitudes and model fits (d–f) for each of the three methods: REXSY, IR-REXSY, and IR-CPMG. Note that a continuous T_2–T_2 spectrum is shown in (a), however, a sparse 2×2 spectrum [analogous to the spectra in (b) and (c)] was used when analyzing the data.

One potential issue with the aqueous urea model is pH instability, which arises due to decomposition of urea into ammonium and cyanate ions [18]. Previous work by our group [4] noted a significant pH drift in unbuffered solutions at nonneutral pH values. Exchange rates are very slow at neutral pH [1]; therefore, nonneutral pH preparations are likely of more interest for most model systems. In this study, we chose to buffer the solution to minimize this issue. Phosphate buffer was chosen because it has been shown to greatly reduce cyanate production in urea solutions [18]. A relatively low concentration of buffer (10 mM) was chosen because the addition of buffer can significantly increase exchange. This preparation resulted in a pH drift of less than 0.1 pH unit per 24-hr period. The addition of phosphate buffer makes it difficult, if not impossible, to compare the exchange rates derived herein to these previous studies. However, this model does provide a relatively stable and flexible — in terms of the relative relaxation rates and pool sizes — system that is ideal for testing novel approaches as well as routine calibration and quality control.

Conclusions

In this Chapter, Monte Carlo simulations and NMR measurements in an aqueous urea model were used to test and validate three methods for measuring intercompartmental exchange rates. In the following chapter, these methods will be applied in optic nerve, which is a two-pool system, and sciatic nerve, which is a three-pool system. Though we have only tested and validated our model in a two-pool systems, the models equations we developed in Chapter III are applicable to any N-pool system and should, in theory, allow us to extract exchange information from sciatic nerve.

References

[1] R. L. Vold, E. S. Daniel, and S. O. Chan, "Magnetic Resonance Measurements of Proton Exchange in Aqueous Urea," *J Am Chem Soc*, vol. 92, pp. 6771–6776, 1970.

[2] E. G. Finer, F. Franks, and M. J. Tait, "Nuclear Magnetic-Resonance Studies of Aqueous Urea Solutions," *J Am Chem Soc,* vol. 94, pp. 4424–4429, 1972.

[3] J. H. Lee, C. Labadie, C. S. Springer, and G. S. Harbison, "2-Dimensional Inverse Laplace Transform Nmr - Altered Relaxation-Times Allow Detection of Exchange-Correlation," *J Am Chem Soc*, vol. 115, pp. 7761–7764, 1993.

[4] R. A. Horch and M. D. Does, "Aqueous urea as a model system for bi-exponential relaxation," *MAGMA*, vol. 20, pp. 51–56, 2007.

[5] R. M. Henkelman, X. Huang, Q. S. Xiang, G. J. Stanisz, S. D. Swanson, and M. J. Bronskill, "Quantitative interpretation of magnetization transfer," *Magn Reson Med*, vol. 29, pp. 759–766, 1993.

[6] A. R. Travis and M. D. Does, "Selective excitation of myelin water using inversion-recovery-based preparations," *Magn Reson Med*, vol. 54, pp. 743–747, 2005.

[7] K. Levenberg, "A Method for the Solution of Certain Problems in Least-Squares," *Quarterly Applied Math*, vol. 2, pp. 164–168, 1944.

[8] D. W. Marquardt, "An Algorithm for Least-Squares Estimation of Nonlinear Parameters," *J Soc Indust Appl Math*, vol. 11, pp. 431–441, 1963.

[9] J. Mitchell, J. D. Griffith, J. H. Collins, A. J. Sederman, L. F. Gladden, and M. L. Johns, "Validation of NMR relaxation exchange time measurements in porous media," *J Chem Phys*, vol. 127, pp. 234701, 2007.

[10] F. C. Thomas and Y. Y. Li, "On The Convergence Of Interior-Reflective Newton Methods For Nonlinear Minimization Subject To Bounds," *Math Progr*, vol. 67, pp. 189–224, 1994.

[11] T. F. Coleman and Y. Y. Li, "An interior trust region approach for nonlinear minimization subject to bounds," *Siam J Optim*, vol. 6, pp. 418–445, 1996.

[12] S. J. Graham, P. L. Stanchev, and M. J. Bronskill, "Criteria for analysis of multicomponent tissue T_2 relaxation data," *Magn Reson Med*, vol. 35, pp. 370–378, 1996.

[13] J. E. M. Snaar and H. Vanas, "A method for the simultaneous measurements of NMR spin-lattice and spin-spin relaxation times in compartmentalized systems," *J Magn Reson*, vol. 99, pp. 139–148, 1992.

[14] D. F. Gochberg, R. P. Kennan, and J. C. Gore, "Quantitative studies of magnetization transfer by selective excitation and T_1 recovery," *Magn Reson Med*, vol. 38, pp. 224–231, 1997.

[15] K. E. Washburn and P. T. Callaghan, "Propagator resolved transverse relaxation exchange spectroscopy," *J Magn Reson*, vol. 186, pp. 337–340, 2007.

[16] P. T. Callaghan, A. Coy, D. MacGowan, K. J. Packer, and F. O. Zelaya, "Diffraction-like effects in NMR diffusion studies of fluids in porous solids," *Nature*, vol. 351, pp. 467–469, 1991.

[17] G. A. F. Seber and C. J. Wild, *Nonlinear Regression.* Hoboken, NJ, 2003.

[18] M. F. Lin, C. Williams, M. V. Murray, G. Conn, and P. A. Ropp, "Ion chromatographic quantification of cyanate in urea solutions: estimation of the efficiency of cyanate scavengers for use in recombinant protein manufacturing," *J Chromatogr B Analyt Technol Biomed Life Sci*, vol. 803, pp. 353–362, 2004.

CHAPTER V

NMR EXCHANGE MEASUREMENTS IN MODEL TISSUE SYSTEMS

Introduction

Previous work has attempted to quantify exchange rates in white matter [1] and optic nerve [2]. Unfortunately, the exchange rates derived from these studies were quite different, which is surprising given the structural similarity between these tissues. In peripheral nerve, previous work has suggested that exchange is very slow [3]; however, no studies to date have attempted to quantify these rates. As a result, additional studies are needed to quantify exchange rates in myelinated tissues.

In this Chapter, the IR-REXSY method for measuring exchange, which was presented in Chapter III and validated in Chapter IV, will be applied in two model tissues *ex vivo*: optic nerve and sciatic nerve. The resultant model parameters will be discussed in the context of experimental T_1–T_2 data. Also, the potential influence of MT on the extracted model parameters will be discussed.

Theory

The model equations developed in Chapter III are applicable to any *N*-pool system. As a result they will be applied herein to describe the two signal components identified in optic nerve and the three signal components identified in sciatic nerve.

The two-compartment system used to model optic nerve is shown in Fig. 5.1a. The superscript *m* denotes myelin water and the superscript *n* denotes non-myelin, or axonal plus

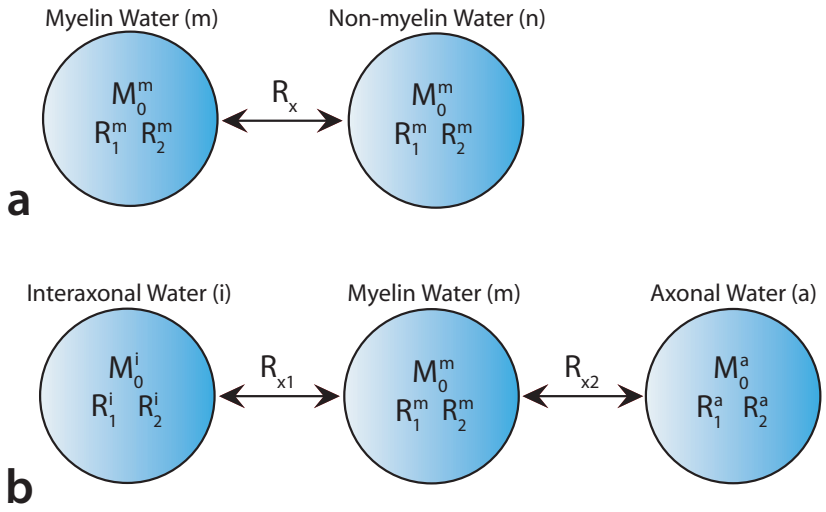

Fig. 5.1. Two- (a) and three-compartment (b) models for optic and sciatic nerve, respectively. Unique equilibrium magnetizations M_0^j and relaxation rates (R_1^j and R_2^j) are defined for each pool *j*. R_x is the single-parameter representation of the exchange rate between each compartment.

interaxonal water. The model contains seven independent parameters: the equilibrium magnetization of each compartment *j* (M_0^j), the relaxation rates for water within each compartment (R_1^j and R_2^j), and the exchange rate between compartments (R_x). Here, R_x is the single-parameter representation of the exchange rate [4], which must be weighted by the compartment sizes in each direction to obtain the pseudo first-order exchange rates (e.g, $k_{nm} = R_x M_0^m$ is exchange from compartment *n* to *m*).

The three-compartment system used to model sciatic nerve is shown in Fig. 5.1b. The superscript *m* denotes myelin water, the superscript *i* denotes interaxonal water, and the superscript *a* denotes axonal water. To simplify this model, it is assumed that no exchange occurs directly between interaxonal and axonal water. This is based upon the fact that water must traverse the myelin sheath to travel from the interaxonal space to the axonal space (and vice versa). This model can be further simplified, by assuming that the two single-parameter

exchanges rates are the same (i.e., $R_{x1} = R_{x2}$). This assumption can be derived from the following relationship [5]

$$P = k_{jk}\left(\frac{V_j}{A}\right) \tag{5.1}$$

where P is the membrane permeability coefficient (in cm/s), V_j is the volume of compartment j and, and A is the surface area of the membrane separating compartments j and k. Assuming the membrane permeability is the same between myelin and axonal water as between myelin and interaxonal water and that axon and nerve fiber are concentric cylinders, R_{x1} and R_{x2} can related by

$$\frac{R_{x2}}{R_{x1}} = g\text{-}ratio\left(\frac{M_0^i}{M_0^a}\right) \tag{5.2}$$

where the *g-ratio* is defined as the ratio of axon radius to nerve fiber radius. Using previously measured values of *g-ratio* $\approx$ 0.7 [6], M_0^i = 0.52, and M_0^a = 0.34 [7], this ratio reduces to approximately one. These simplifications result in a model with ten independent parameters defined in the same fashion as the two-compartment model parameters used to describe optic nerve.

Materials and Methods

Sample Preparation

Adult rats (Sprague-Dawley and Lewis) and African clawed frogs (*Xenopus laevis*) were used for all studies in accordance with protocols approved by the Institutional Animal Care and Use Committee of Vanderbilt University.

Rats (n = 2) were euthanized *via* CO_2 inhalation. Following euthanasia, both optic nerves were excised from the optic chiasm to the skull (≈ 1 cm segments), cleaned of attached blood and soft tissue, and immersed in phosphate buffered saline (PBS; Mediatech Inc., Herdon, VA) at 4˚C until NMR was performed (≤ 6 hrs).

Frogs (n = 2) were euthanized by either immersion in a 10 g/L bath of tricaine methanesulfonate (Finquel®; Argent, Redmond, WA) for 20–30 minutes or by 120 mg/kg i.p. injection of sodium pentobarbital (Sleepaway®; Ft. Dodge Laboratories, Ft. Dodge, IA). Following euthanasia, 1–2 cm segments of sciatic nerve were excised from each hindlimb, cleaned of attached blood and soft tissue, and immersed in amphibian Ringer's solution (Fisher Scientific, Rochester, NY) at room temperature until NMR was performed (≤ 2 hrs).

Prior to each NMR session, both optic nerve samples (or both sciatic nerve samples) were placed in 5-mm NMR tubes and bathed in perfluorcarbon solution (Fomblin®; Solvay Solexis, Thorofare, NJ) to prevent tissue drying without contributing proton signal. A T_2 spectrum was measured from CPMG data acquired at the beginning and end of each NMR session. The spectral characteristics (T_2 and amplitude of each component) from each of these measurements were similar for all samples, indicating that tissue microanatomy was well-preserved over the course of each NMR session.

NMR

NMR measurements were performed on excised samples at bore temperature (≈20˚C) using a 300 MHz, 16-cm bore Varian Inova (Varian Inc., Palo Alto, CA) spectrometer equipped with imaging gradients capable of generating 27 G/cm with switching times to full amplitude of 100 μs. An in-house-built loop-gap resonator (10 mm in diameter, 20 mm long) was used for RF transmission and reception.

Data were collected for CPMG and IR-REXSY pulse sequences (as defined in Figs. 2.2 and 3.6). For the CPMG sequence, 1024 echoes (NE) spaced at 1-ms were collected over four averaged excitations (NEX). A 20-s predelay was used to ensure thermal equilibrium was reached prior to each excitation pulse. IR-REXSY data were collected using the same parameters at 20 mixing times (t_m) linearly arrayed in 100 ms increments with a delay prior to storage (t_{e1}) of 2 ms. The IR-REXSY sequence was repeated in multiples of two (NEX = 2–6 depending on available SNR) to accompany the two-part phase cycle previously described (Chapter III). For each sample, the short-T_2 component, which is presumed to represent myelin water, was nulled. The inversion time (t_i) to null the myelin water component was experimentally determined from IR-CPMG derived T_2 spectra. The optimal inversion time (≈ 600 ms for all samples) was chosen as the value that minimized the relative contribution of the myelin water signal.

Data Analysis

Determining apparent relaxation times and pool fractions

Smooth, continuous T_2 distributions (as opposed to the discrete distributions used to describe aqueous urea) are thought to best represent the tissue microstructure present in nerve [8]. Therefore, continuous T_2 spectra were calculated from CPMG nerve data (m_i) by minimizing

$$\sum_{i=1}^{\mathrm{NE}}\left\{\sum_{j=1}^{J}\left(s_j \exp(-t_i / T_{2,j}) - m_i\right)^2\right\} + \mu\sum_{j=2}^{J-1}\left(s_{j-1} - 2s_j + s_{j+1}\right)^2 \tag{5.3}$$

in a non-negative least-squares (NNLS) [9] sense using $J = 256$ logarithmically spaced relaxation times. The first term in Eq. (5.3) minimizes data misfit, while the second term regularizes the solution by imposing a minimum curvature constraint [10], which smoothes the resultant spectrum according to the magnitude of the regularizer term μ. For this study, the value of μ was iteratively updated to a value that increased the χ^2 misfit by 2% relative to the unregularized fit ($\mu = 0$) [11]. Apparent component relaxation times $\tilde{T}_2^j$ and pool sizes $\tilde{M}_0^j$ were determined from these T_2 spectra as the weighted-mean and integrated area for each observed peak, respectively.

Determining exchange rates from IR-REXSY data

T_2 spectra were calculated from IR-REXSY data (at each mixing time) using the same procedure. The resulting T_2 spectra were segmented into domains (two for optic nerve and three for sciatic nerve) corresponding to each observed T_2 component. Domain boundaries for each component were taken as the relaxation times corresponding to the minimum spectral intensity between adjacent components. Component peak amplitudes were derived as the summed spectral signal over each of these domains. Because the component with the shortest T_1 was nulled, these component amplitudes should be negative (or zero). However, NNLS requires all components be nonnegative. As a result, magnitude data were fitted using the NNLS algorithm, and the negative of the resultant peak amplitudes was taken to reflect the true component amplitude.

To invert the compartmental models for each nerve sample, component amplitudes were then fitted to Eq. (3.20) using the previously described method (Chapter IV). Recall that this method uses CPMG-derived apparent relaxation times $\tilde{T}_2^j$ and equilibrium magnetizations $\tilde{M}_0^j$ to numerically constrain the corresponding fitted intrinsic values (T_2^j and M_0^j). For optic nerve data, this effectively reduced the number of free parameters to three (R_1^m, R_1^n, and R_x). For sciatic nerve data, this effectively reduced the number of free parameters to four (R_1^m, R_1^a, R_1^i, and R_x).

Results and Discussion

T_2 Measurements

Representative CPMG-derived T_2 spectra for optic and sciatic nerve are shown in Fig. 5.2. Two significant T_2 components were resolved in both optic nerve samples. These components are currently thought to represent myelin water and non-myelin water, or the combination of axonal and interaxonal water, in order of increasing relaxation time [12-16]. An additional long-T_2 component ($T_2 \approx 500$ ms) was also resolved in these data, but was ignored because it represented $\leq 3\%$ of the total signal. Three significant T_2 components were resolved in both sciatic nerve samples. These components are currently thought to represent myelin water, interaxonal water, and axonal water in order of increasing relaxation time [17, 18].

For each sample, myelin water signal was nulled by appropriate selection of inversion time. This is demonstrated in the IR-CPMG derived T_2 spectra shown in Fig. 5.2. Monte Carlo simulations (Chapter IV) indicated that the choice of component to null is arbitrary in terms of the SNR of the fitted parameters. We chose to null the myelin component here because: 1) the non-myelin water component in optic nerve exhibited a relatively broad T_1 distribution (as

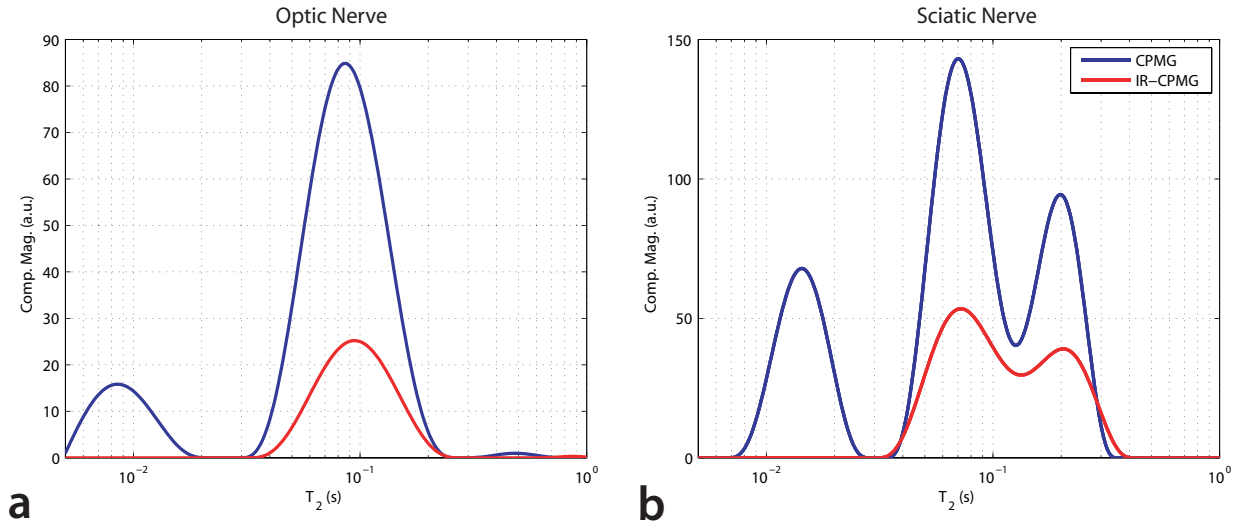

Fig. 5.2. Representative T_2 spectra from CPMG and IR-CPMG data for optic (a) and sciatic nerve (b). Two T_2 components were consistently observed in optic nerve, while three T_2 components were consistently observed in sciatic nerve. Appropriate choice of inversion times for the IR-CPMG sequence resulted in a nulled myelin water component.

demonstrated in Fig. 5.4b) and 2) the myelin water component is presumed to exhibit the largest magnetization transfer (MT) effect (see *Magnetization Transfer Effects* section).

Exchange Measurements

Sample optic nerve IR-REXSY data — T_2 component amplitudes as a function of mixing time — and corresponding model fits are given in Fig. 5.3. The SNR for these data (at thermal equilibrium) was 2570 ± 340. Previous simulations (Chapter IV) indicate that this is sufficient to accurately invert the model. Fitted model parameters for each sample, along with the mean ± SD across samples, are given in Table 5.1. Similar model parameters were derived for each optic nerve sample. Comparing these results to previously published values, it can be seen that our exchange rates were similar to those reported by Bjarnason *et al*. [1] in bovine white matter, but were quite different than those reported by Stanisz *et al*. [2] in bovine optic nerve.

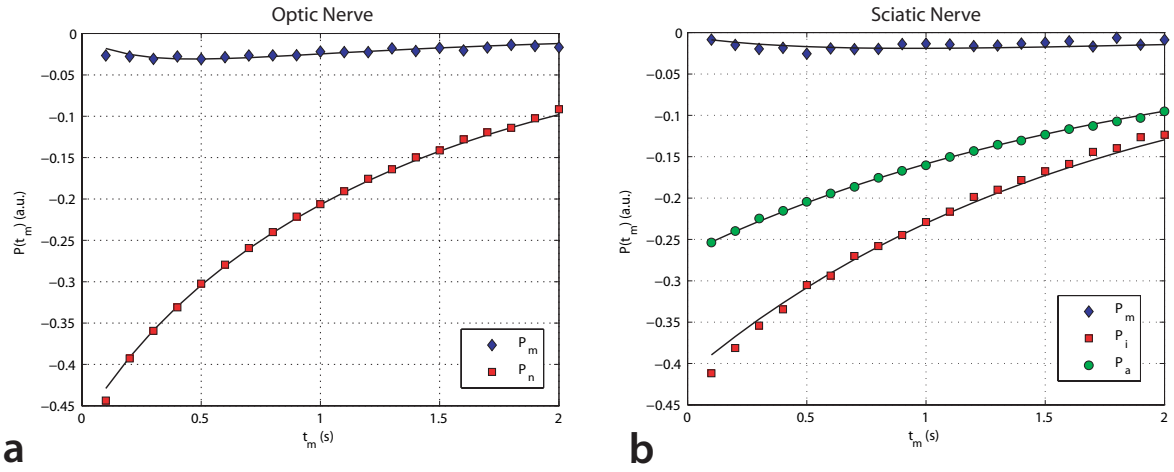

Fig. 5.3. Representative model fits for IR-REXSY data obtained in optic (a) and sciatic nerve.

The exchange rates derived herein were within ≈20% of those derived by Bjarnason *et al*. [1], which is reasonable given the fact that slightly different tissue models and temperatures were used for each study. Note the discrepancy between our fitted relaxation rates and the previously published values. This can likely be attributed to the different field strength used for each study (R_1 decreases and R_2 increases with increasing field strength).

Representative sciatic nerve data are shown Fig. 5.3, and corresponding fitted model parameters are given in Table 5.2. The SNR for these data (at thermal equilibrium) was 4490 ± 340. Again, similar model parameters were derived for each sample in sciatic nerve. Unfortunately, there are no previously published values of exchange rates in peripheral nerve with which to compare our results. However, these results are in agreement with the assertion that exchange is very slow in peripheral nerve [3]. The slower exchange rates in peripheral nerve relative to optic nerve are thought to reflect, at least in part, the characteristically thicker myelin sheaths found in peripheral nerve (peripheral nerve: 0.2–2.0 μm [19], optic nerve: 0.1–0.6 μm [20]).

Table 5.1. Fitted model parameters for optic nerve data. Individual results for each sample along with the mean ± SD across samples are given. Previously reported values are also given.

	Sample #1	Sample #2	Mean ± SD[a]	Stanisz *et al.* [2][b]	Bjarnason *et al.* [1][c]
$R_1^m\ (s^{-1})$	1.28	1.51	1.34 ± 0.17	2.16	2.91
$R_1^n\ (s^{-1})$	0.68	0.63	0.65 ± 0.03	1.03	1.06
$R_2^m\ (s^{-1})$	109.53	116.02	112.78 ± 4.59	45.46	68.49
$R_2^n\ (s^{-1})$	10.49	13.09	11.79 ± 1.84	5.68	8.93
M_0^m	0.14	0.16	0.15 ± 0.02	0.32	0.12
M_0^n	0.86	0.84	0.85 ± 0.02	0.68	0.88
$k_{mn}(s^{-1})$	2.54	2.54	2.54 ± 0.01	6.2	3.22
$k_{nm}(s^{-1})$	0.40	0.49	0.44 ± 0.06	2.9	0.57

[a] Study performed in rat optic nerve samples at 7 T and 20˚C.
[b] Study performed in bovine optic nerve samples at 1.5 T and ≈20˚C.
[c] Study performed in bovine white matter samples at 2.1 T and 24˚C.

Table 5.2. Fitted model parameters for sciatic nerve data. Individual results for each sample along with the mean ± SD across samples are given.

	Sample #1	Sample #2	Mean ± SD[a]
$R_1^m\ (s^{-1})$	1.24	1.13	1.18 ± 0.08
$R_1^i\ (s^{-1})$	0.52	0.53	0.53 ±0.01
$R_1^a\ (s^{-1})$	0.45	0.50	0.48 ± 0.03
$R_2^m\ (s^{-1})$	66.75	68.00	67.34 ± 0.86
$R_2^i\ (s^{-1})$	13.01	15.42	14.22 ± 1.71
$R_2^a\ (s^{-1})$	4.74	4.73	4.74 ± 0.01
M_0^m	0.22	0.19	0.21 ± 0.02
M_0^i	0.52	0.52	0.52 ± 0.01
M_0^a	0.26	0.29	0.28 ± 0.02
$k_{mi}(s^{-1})$	0.24	0.26	0.25 ± 0.02
$k_{im}(s^{-1})$	0.10	0.10	0.10 ± 0.01
$k_{ma}(s^{-1})$	0.12	0.14	0.13 ± 0.02
$k_{am}(s^{-1})$	0.10	0.10	0.10 ± 0.01

[a] Study performed in frog sciatic nerve samples at 7 T and ≈20˚C.

T_1–T_2 Simulations

The model parameters presented in Tables 5.1 (Sample #2) and 5.2 (Sample #1) were used in conjunction with Eq. (3.17) to generate T_1–T_2 data, which were subsequently 2D inverse Laplace transformed to generate T_1–T_2 spectra. The simulated results are shown Figs. 5.4a and 5.4c for optic and sciatic nerve, respectively, with the intrinsic model parameters shown in red and the corresponding simulated apparent values shown in blue. From these results, it can be seen that the T_2 values extracted from T_1–T_2 analysis are relatively unaffected by exchange. The extracted

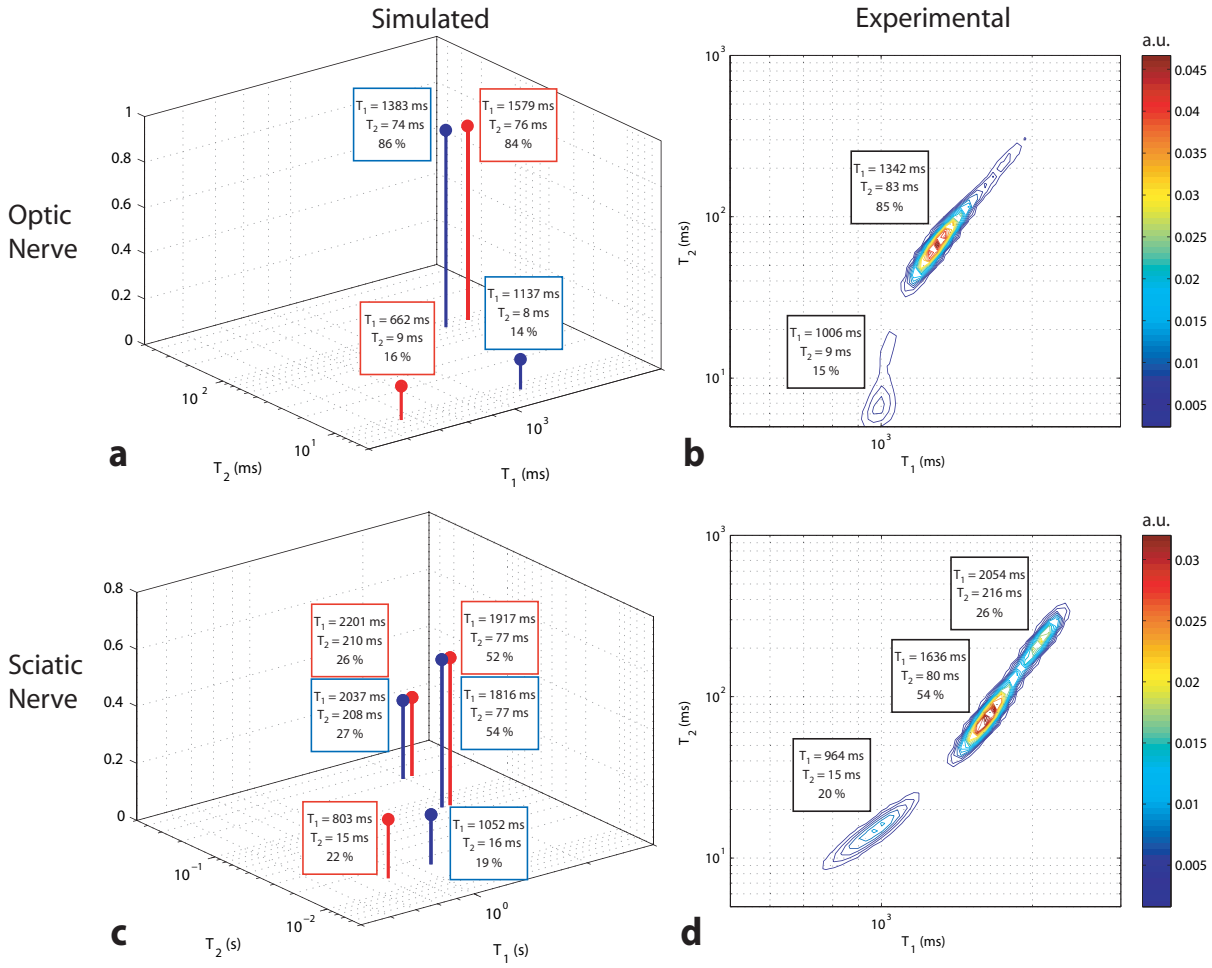

Fig. 5.4. (a and c) T_1–T_2 exchange simulations using the model parameters in Tables 5.1 (Sample #2) and 5.2 (Sample #1). Model parameters, or intrinsic values, are shown in red, while apparent values are in blue. (b and d) Corresponding experimental T_1–T_2 data.

T_1 values are much more significantly affected, which is expected given the longer timescale of T_1 relative to T_2. Looking at the relative compartment sizes, exchange between compartments results in an underestimation of the short-T_2 myelin water component by 2–3%, which is consistent with previous findings [1]. These simulated spectra were compared to experimentally derived T_1–T_2 spectra shown in Figs. 5.4b and 5.4d to determine whether our model parameters were sensible in this context. It can be seen that our simulated results reasonably predict the experimental results.

Magnetization Transfer Effects

Although the fitted model shown in Fig. 5.3 generally agrees with experimental data — the average residual deviation per point was ≈0.5% for all fits — some systematic differences were observed. This deviation from the model is especially visible at shorter mixing times. Likely causes for this deviation include: 1) the treatment of model parameters as discrete, rather than continuous distributions (as was done for T_2 spectral fitting), 2) inappropriate model assumptions (e.g., compartment-component relationships), and 3) MT between mobile and semi-solid protons within each anatomical compartment. Additional information about the shape and characteristic width of each model parameter's distribution is needed to test whether treating the model parameters as discrete is a significant issue. Also, though compartmental modeling of the NMR signal in myelinated tissue is still an ongoing area of research, each assumption made herein was based upon a sizeable body of literature [12-18]. With regards to MT, attempts to minimize this effect were made as discussed below.

At the beginning of the IR-REXSY storage period, semi-solid proton longitudinal magnetization is expected to be approximately nulled. This can be attributed to: 1) a progressive

saturation of semi-solid proton longitudinal magnetization with each RF pulse — assuming the RF pulse widths are on the order of the semi-solid proton T_2 (≈10 μs) — and 2) a loss of coherence for any semi-solid proton transverse magnetization created prior to the storage pulse. It has previously been shown that a difference in normalized longitudinal magnetization must exist between mobile and semi-solid proton pools for MT to occur [21]. Because the semi-solid pool will be approximately nulled at the beginning of the storage period, this effect will be smallest for the nulled mobile proton component. Because previous work suggests the MT contributions are most significant for myelin water [1-3], we chose to null myelin water in the current study.

Attempts to incorporate MT into our models — fitting optic nerve data to a four-compartment model as described in [1, 2] and fitting sciatic nerve data to a six-compartment model — were unsuccessful. This is not surprising given our measurements are not designed to be highly sensitive to MT. As a result, future work is needed to determine the magnitude of MT effects on IR-REXSY derived exchange rates. Though we ignored MT in our current model, the derived exchange rates were similar to those reported by Bjarnason *et al.* [1] (who did incorporate MT into their model), suggesting this effect might be relatively small in IR-REXSY data.

Conclusions

In this Chapter, rates of water exchange between compartments in optic and sciatic nerve were quantified using a novel approach. For optic nerve, the derived rates were similar to previously published values. Furthermore, T_1–T_2 data generated from fitted model parameter were is

reasonable agreement with experimentally derived T_1–T_2 data. Additional work in needed to determine the magnitude of MT effects on these derived exchange rates.

References

[1] T. A. Bjarnason, I. M. Vavasour, C. L. Chia, and A. L. MacKay, "Characterization of the NMR behavior of white matter in bovine brain," *Magn Reson Med*, vol. 54, pp. 1072–1081, 2005.

[2] G. Stanisz, A. Kecojevic, M. Bronskill, and R. Henkelman, "Characterizing white matter with magnetization transfer and T_2," *Magn Reson Med*, vol. 42, pp. 1128–1136, 1999.

[3] M. D. Does, C. Beaulieu, P. S. Allen, and R. E. Snyder, "Multi-component T_1 relaxation and magnetisation transfer in peripheral nerve," *Magn Reson Imaging*, vol. 16, pp. 1033–1041, 1998.

[4] R. M. Henkelman, X. Huang, Q. S. Xiang, G. J. Stanisz, S. D. Swanson, and M. J. Bronskill, "Quantitative interpretation of magnetization transfer," *Magn Reson Med*, vol. 29, pp. 759–766, 1993.

[5] S. T. Chen and C. S. Springer, Jr., "Ionophore-catalyzed cation transport between phospholipid inverted micelles manifest in DNMR," *Biophys Chem*, vol. 14, pp. 375–388, 1981.

[6] R. L. Friede, "Computer editing of morphometric data on nerve fibers. An improved computer program," *Acta Neuropathologica*, vol. 72, pp. 74–81, 1986.

[7] A. R. Travis and M. D. Does, "Selective excitation of myelin water using inversion-recovery-based preparations," *Magn Reson Med*, vol. 54, pp. 743–747, 2005.

[8] R. M. Kroeker and R. Mark Henkelman, "Analysis of biological NMR relaxation data with continuous distributions of relaxation times," *J Magn Reson*, vol. 69, pp. 218–235, 1986.

[9] C. L. Lawson and R. J. Hanson, *Solving Least Squares Problems*. Englewood Cliffs, NJ: Prentice-Hall, 1974.

[10] K. P. Whittall and A. L. Mackay, "Quantitative Interpretation of NMR Relaxation Data," *J Magn Reson*, vol. 84, pp. 134–152, 1989.

[11] S. J. Graham, P. L. Stanchev, and M. J. Bronskill, "Criteria for analysis of multicomponent tissue T_2 relaxation data," *Magn Reson Med*, vol. 35, pp. 370–378, 1996.

[12] W. A. Stewart, A. L. Mackay, K. P. Whittall, G. R. W. Moore, and D. W. Paty, "Spin-spin relaxation in experimental allergic encephalomyelitis: Analysis of CPMG data using

a nonlinear least-squares method and linear inverse-theory," *Magn Reson Med*, vol. 29, pp. 767–775, 1993.

[13] A. Mackay, K. Whittal, J. Adler, D. Li, D. Paty, and D. Graeb, "In-vivo visualization of myelin water in brain by magnetic resonance," *Magn Reson Med*, vol. 31, pp. 673–677, 1994.

[14] P. J. Gareau, B. K. Rutt, S. J. Karlik, and J. R. Mitchell, "Magnetization transfer and multicomponent T_2 relaxation measurements with histopathologic correlation in an experimental model of MS," *J Magn Reson Imaging*, vol. 11, pp. 586–595, 2000.

[15] C. Laule, E. Leung, D. K. Lis, A. L. Traboulsee, D. W. Paty, A. L. MacKay, and G. R. Moore, "Myelin water imaging in multiple sclerosis: quantitative correlations with histopathology," *Mult Scler*, vol. 12, pp. 747–753, 2006.

[16] A. Dula, "Micro-anatomical characterization of central white matter using magnetic resonance imaging," in *Biomedical Engineering*, vol. Ph.D. Nashville, TN: Vanderbilt University, 2008, pp. 111.

[17] S. Peled, D. G. Cory, S. A. Raymond, D. A. Kirschner, and F. A. Jolesz, "Water diffusion, T_2, and compartmentation in frog sciatic nerve," *Magn Reson Med*, vol. 42, pp. 911–918, 1999.

[18] K. Wachowicz and R. E. Snyder, "Assignment of the T_2 components of amphibian peripheral nerve to their microanatomical compartments," *Magn Reson Med*, vol. 47, pp. 239–245, 2002.

[19] R. L. Friede and W. Beuche, "A new approach toward analyzing peripheral nerve fiber populations. I. Variance in sheath thickness corresponds to different geometric proportions of the internodes," *J Neuropathol Exp Neurol*, vol. 44, pp. 60–72, 1985.

[20] R. W. Williams and L. M. Chalupa, "An analysis of axon caliber within the optic nerve of the cat: evidence of size groupings and regional organization," *J Neurosci*, vol. 3, pp. 1554–1564, 1983.

[21] D. F. Gochberg, R. P. Kennan, and J. C. Gore, "Quantitative studies of magnetization transfer by selective excitation and T_1 recovery," *Magn Reson Med*, vol. 38, pp. 224–231, 1997.

CHAPTER VI

COMPARTMENTAL CHARACTERIZATION OF WHITE MATTER AND NERVE *EX VIVO* USING CHROMIUM

Introduction

Water from within myelin, axonal, and interaxonal compartments of peripheral nerve can be isolated based upon multiexponential T_1 and/or T_2 [1-10]. In central white matter, however, only two relaxation components are generally found [11-15]: a short relaxation time component arising from myelin water and a long relaxation time component arising from a combination of axonal and interaxonal water. The inability to resolve signal from axonal and interaxonal water in white matter likely arises because each compartment exhibits similar relaxation characteristics. Under this presumption, signal from these compartments could be isolated by preferentially altering the T_1 and/or T_2 of axonal or interaxonal water using a compartmentally specific contrast reagent.

Chromium, specifically Cr(VI) in the form of potassium dichromate, may be such a reagent as it has been shown to result in white matter specific enhancement following injection into neural tissue [16]. This enhancement is thought to arise due to reduction of diamagnetic Cr(VI) to paramagnetic chromium species [Cr(V) and/or Cr(III)] by oxidizable myelin lipids. That is, enhancement is "turned on" following tissue-specific reduction of Cr(VI). Though myelin lipids are thought to play a primary role, differential enhancement of axonal and interaxonal water may occur as exchange with and/or access to paramagnetic chromium may be different for these compartments. Interestingly, enhancement has been shown to remain *in vivo* for up to 72 hours following intracerebroventricular (ICV) administration of potassium dichromate [16]. This

suggests that Cr(III), which is significantly more stable than intermediates such as Cr(V) [17], remains stably bound or complexed to oxidized compounds in white matter. This is an attractive property for its use in quantitative studies because it can be assumed that contrast-enhancement is constant over the time-course of most measurements, removing a free parameter that would otherwise need to be estimated.

In this study, integrated T_1–T_2 measurements, which are sensitive to the correlated T_1 and T_2 within a spin group [18-20], were made on potassium dichromate loaded (hereafter referred to as chromated) rat brains *ex vivo* to demonstrate its ability to isolate signal from axonal and interaxonal water in white matter. For comparison, similar measurements were made in formalin fixed brains enhanced with a "non-selective" contrast reagent, specifically Gd-DTPA. Additional studies were performed in optic nerve, a commonly used model for cerebral white matter. This model was chosen because reagent loading time is relatively short in optic nerve (due to its relatively small diameter), allowing studies to be performed in fresh, unfixed tissue. These studies were performed *ex vivo* because: i) they require high signal-to-noise ratio (SNR) and ii) potassium dichromate is a known carcinogen [21].

In order to investigate the compartmental basis of contrast enhancement in white matter, additional relaxation measurements were made in normal, Gd-enhanced, and chromated frog sciatic nerve. This model system was chosen because its relaxation characteristics and corresponding compartmental origins have been relatively well characterized [1, 3, 6, 8, 10]. Furthermore, each component of anatomical relevance — myelin, axonal, and interaxonal — should be resolvable in both normal and contrast-enhanced nerve, allowing inference of each compartment's relative access to the contrast reagent. This work represents the first attempt to

quantitatively characterize the compartmental relaxation characteristics of chromium in white matter and peripheral nerve.

Materials and Methods

Sample Preparation

Adult Sprague-Dawley rats and African clawed frogs (*Xenopus laevis*) were used for all studies in accordance with protocols approved by the Institutional Animal Care and Use Committee of Vanderbilt University. All studies were performed in excised rat brain, rat optic nerve, or frog sciatic nerve.

Brain Studies

Rats were euthanized *via* CO_2 inhalation. Following euthanasia, brains were excised, dried of excess fluid, and loaded with either potassium dichromate (chromated brains, n = 8) or Gd-DTPA (Gd-enhanced brains, n = 2).

For chromation, excised brains were immersed in 85 mM potassium dichromate ($K_2Cr_2O_7$; Sigma, Taufkirchen, Germany) dissolved in phosphate buffered saline (PBS; Mediatech Inc., Herdon, VA) for 72 hrs (pH = 5). These brains were then placed into fresh PBS, washing daily for ≈ 1 week. This period was chosen because it represented the point at which most excess potassium dichromate had diffused out of the brain (determined from color of PBS at each 24-hour interval). These studies were performed in fresh tissue (e.g., without any aldehyde fixation) because aldehydes are known reductants, which, if present, would reduce Cr(VI) before the reaching the targeted reductants in tissue (see *Discussion* for details).

For Gd-enhancement, excised brains were fixed by immersion in 10% neutral buffered formalin (VWR, West Chester, PA) for 24 hrs then washed in PBS for ≥ 48 hrs to wash out excess fixative. These brains were then immersed in 1 mM Gd-DTPA (Magnevist®; Belex, Montville, NJ) dissolved in PBS until the contrast reagent was evenly distributed throughout the brain (≥ 6 days).

Following contrast reagent loading, brains were placed in a custom-built holder and bathed in buffer solution. Chromated brains were immersed in perfluorcarbon solution (Fomblin®; Solvay Solexis, Thorofare, NJ) to prevent tissue drying without contributing proton signal, while Gd-enhanced brains were immersed in the same Gd-DTPA solution used for contrast reagent loading to ensure that contrast-enhancement was constant during each measurement.

Optic Nerve Studies

Rats were euthanized *via* CO_2 inhalation. Following euthanasia, both optic nerves were excised from the optic chiasm to the skull, dried of excess fluid, and immersed in either potassium dichromate (chromated optic nerves, n = 4) or PBS (control optic nerve, n = 3) at room temperature.

For chromation, optic nerve were immersed in 85 mM potassium dichromate dissolved in PBS for 1 hr. The optic nerve samples were then placed into fresh PBS, washing at least two times over a period of approximately 3 hrs. Control nerve remained in PBS during this 4-hr period. Following this period, samples were placed in 5-mm NMR tubes, bathed in Fomblin, and NMR measurements were performed.

Note the different chromation/washing period used in optic nerve relative to brain. These periods were determined for each tissue experimentally to ensure that: i) reagents were

homogenously distributed throughout the tissue and ii) excess chromium was removed, allowing compartmental differences in enhancement to be observed.

To evaluate whether any morphological changes had occurred during the reagent loading periods, several of these optic nerve samples were processed for histological analysis. These samples were fixed by immersion in 4% glutaraldehyde dissolved in 0.1 M phosphate buffer (pH 7.0), post-fixed with osmium tetroxide, and embedded in Epon. Sections (1 mm) were cut and stained with toluidine blue and evaluated by light microscopy using a Leica DM-IRB inverted microscope equipped with a Nikon DXM1200C digital camera.

Sciatic Nerve Studies

Frogs were euthanized by either immersion in a 10 g/L bath of tricaine methanesulfonate (Finquel®; Argent, Redmond, WA) for 20–30 minutes or by 120 mg/kg i.p. injection of sodium pentobarbital (Sleepaway®; Ft. Dodge Laboratories, Ft. Dodge, IA). Following euthanasia, 1–2 cm segments of sciatic nerve were excised from each hind leg, yielding two samples from each frog. Samples were then cleaned of attached blood and soft tissue, dried of excess fluid, and immersed in either potassium dichromate (chromated nerves, n = 2) , Gd-DTPA (Gd-enhanced nerves, n = 2), or amphibian Ringer's solution (control nerves, n = 2) at room temperature.

For chromation, nerve samples were immersed in 160 mM of potassium dichromate dissolved in amphibian Ringer's solution (Fisher Scientific, Rochester, NY) for 1 hour (pH = 4.6). These samples were then placed in fresh amphibian Ringer's solution, washing four times over an additional hour. For Gd-enhancement, nerve samples were immersed in 0.5 mM Gd-DTPA dissolved in amphibian Ringer's solution for approximately 2 hours. Control samples remained in amphibian Ringer's solution during this two-hour period. Immediately after each

two-hour treatment period, samples were placed in 5-mm NMR tubes and bathed in either fresh amphibian Ringer's solution (control and chromated samples) or Fomblin (Gd-enhanced samples), at which time NMR measurements were performed.

Data Acquisition

All measurements were made at bore temperature (≈ 20ºC) using a 7.0-T, 16-cm bore Varian Inova spectrometer (Varian Inc., Palo Alto, CA). A 25-mm diameter Litz RF coil (Doty Scientific, Columbia, SC) was used for MRI measurements of rat brain, while a 10-mm diameter single-turn RF coil was used for NMR measurements of frog sciatic nerve and rat optic nerve.

Brain Studies

For each rat brain, a single 1.5-mm slice orthogonal to the corpus callosum at its intersection with the fornix was first selected from coronal fast spin-echo scout images (Fig. 6.1a). Integrated T_1–T_2 measurements were then made using an inversion-recovery prepared multiple spin-echo (IR-ME) sequence at sixteen different inversion-recovery delays (TI) ranging logarithmically between 30 ms and 2 s, acquiring 32 echoes (NE) at a spacing of 6.5 ms (TE) for each inversion time. Additional imaging parameters included a 4-s repetition time to ensure thermal equilibrium before each inversion pulse, an acquisition bandwidth of 50 kHz, a 20 × 20 mm^2 field of view, a 64 × 64 acquisition matrix, and two averaged excitations (NEX). To ensure uniform inversion over the sample, a 5-ms hyperbolic secant inversion pulse was used [22]. Also, spoiler gradients were placed about each $90_x180_y90_x$ broadband composite refocusing pulse [23] in an alternating and descending fashion [24] in order to remove signal from unwanted coherence pathways. The spoiler gradients were calculated so as to cause a minimum phase dispersion of $\pi/2$ across one

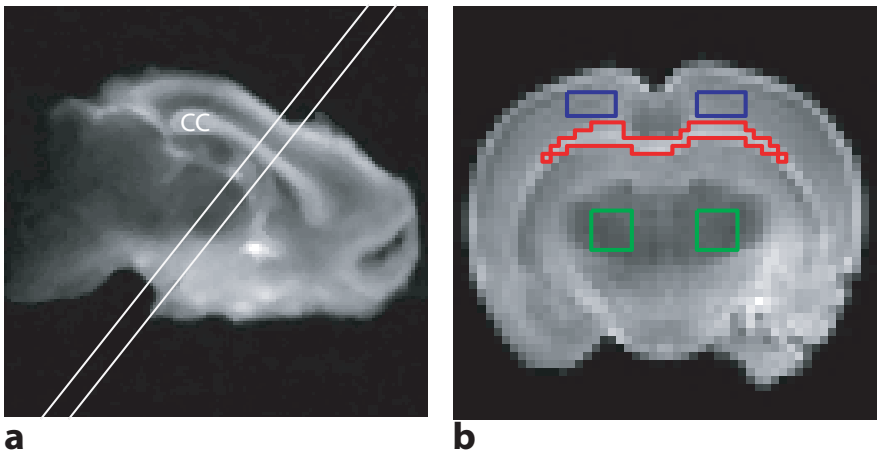

Fig. 6.1. (a) Sample T_2-weighted fast spin-echo coronal image, identifying a 1.5-mm slice orthogonal to the corpus callosum (cc) for T_1–T_2 measurements. The image was median-filtered for display purposes. (b) Resultant 1.5-mm slice from (a), identifying sample ROIs used for T_1–T_2 analysis. Shown are ROIs for corpus callosum (red), cortical grey matter (blue), and sub-cortical grey matter (green). Signal from contralateral ROIs in grey matter were summed prior to spectral analysis.

slice thickness, which was found to be sufficiently large to remove stimulated echo artifacts within the decay curve.

In each sample, regions of interest (ROIs) were defined within the corpus callosum, cortical grey matter, and sub-cortical grey matter for subsequent analysis (Fig. 6.1b). To remove bias from Rician noise, the maximum-likelihood estimator of each Rician-distributed ROI value was estimated [25].

Optic and Sciatic Nerve Studies

For each nerve sample, integrated T_1–T_2 measurements were made with an inversion-recovery prepared CPMG sequence (IR-CPMG) using 24 or 32 different logarithmically-spaced TI values (the range of values for each sample was chosen to ensure that the T_1 recovery curve was adequately sampled), 2000 NE, a 1-ms TE, a four-step phase cycle, and 4 NEX. In all samples,

the predelay was long enough to ensure thermal equilibrium was achieved prior to the inversion pulse. Additional equilibrium CPMG data were also acquired (without an inversion recovery preparation) to be used as described below.

Data Analysis

In order to satisfy nonnegativity constraints imposed by non-negative least-squares (NNLS) [26] fitting, inversion-recovery data were transformed to a decay (by subtracting IR-ME and IR-CPMG data from corresponding equilibrium data). Multiexponential analysis was then used to determine the distribution of T_1s and T_2s, or T_1–T_2 spectrum, within each rat brain ROI and nerve sample. This was done by fitting T_1–T_2 data, $y(\tau_i, t_j)$, in an NNLS sense to

$$y(\tau_i, t_j) = 2\sum_{m}^{M}\sum_{n}^{N} S_{mn} \exp\left(-\tau_i / T_{1m}\right) \exp\left(-t_j / T_{2n}\right) \tag{6.1}$$

where S_{mn} is the magnitude of each fitted exponential component and τ_i and t_j are the experimental parameters TI and TE, respectively. A logarithmically spaced grid (50 × 50) of relaxation times (T_{1m} and T_{2n}) was used for each fit with a range spanning all expected values within each sample. An additional minimum Laplacian constraint was incorporated into these fits to regularize the solution. This constraint smoothes the T_1–T_2 spectra and is analogous to minimum "curvature" constraints [27] commonly used to regularize the inversion of one-dimensional relaxation data. The regularizer parameter, which increases the weight of this minimum Laplacian constraint at the expense of data misfit, was set within the range of values small enough to allow resolution of neighboring peaks, yet large enough to minimize spurious

peaks. In order to reduce computational time, data and model dimensionality were reduced using a singular value decomposition approach prior to inversion [28].

Component relaxation times, defined as the mean relaxation time for a given component, and signal fractions, defined as the summed component signal divided by the total summed spectral signal, were calculated for observed components in each spectrum. Components not found in all samples were deemed spurious and ignored in these calculations. Also, a short-T_1 component found in Gd-enhanced samples (Fig. 6.2c, 6.3a, and 6.3c), which was thought to arise due to magnetization transfer (MT) effects, was ignored in these calculations as well (see *Results* for details). All reported values are given as mean (±SD) across samples within a given group (e.g., chromated white matter) unless otherwise stated.

Results

Brain Studies

Typical data from chromated and Gd-enhanced white matter along with corresponding model fits [Eq. (6.1)] and T_1–T_2 spectra are shown in Fig. 6.2. Although inversion of these data into a relaxation spectrum is a difficult numerical problem, with sufficient SNR and appropriate regularization, reproducible results can be found. Data from chromated white matter had an SNR > 2000 in all cases (where SNR is defined as the echo magnitude at TE/TI = 6.5/2000 ms divided by the standard deviation of the background noise after correction for its Rayleigh bias [29]). Simulations (results not shown) indicated this SNR to be sufficient to resolve the T_1–T_2 components shown in Fig. 6.2. The SNRs from all other ROIs were of the same order of magnitude.

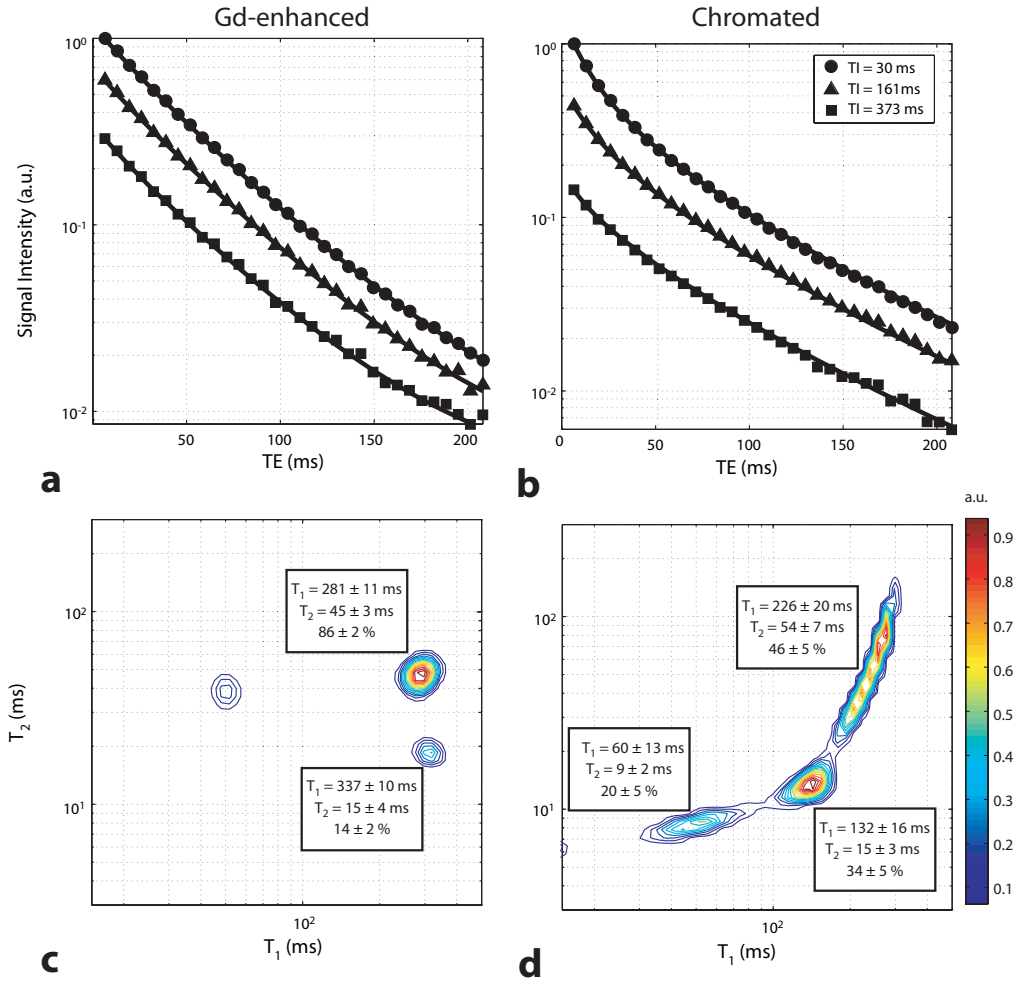

Fig. 6.2. Sample normalized signal intensities (a & b) and corresponding T_1–T_2 spectra (c & d) for Gd-enhanced (a & c) and chromated (b & d) white matter. (a & b) Shown are the decay curves for three of the sixteen inversion times along with model fits from Eq. (6.1). Note the deviation from a straight line for each semi-log plot, indicative of multiexponential decay. All errorbars were smaller than the markers used for plotting and were, therefore, omitted. (c & d) The component relaxation times and signal fractions averaged across samples are shown for each T_1–T_2 spectrum. Spurious components along with those likely arising from MT effects [unlabeled short-T_1 component in (c)] were ignored in the pool fraction calculation.

T_1–T_2 spectra from chromated white matter signal (Fig. 6.2d) revealed three distinct components, each with different T_1 and T_2 values. Across samples, mean signal fractions were 20 ± 5, 34 ± 5, and 46 ± 5 % for components with short (T_1 = 60 ± 13 ms, T_2 = 9 ± 2 ms), intermediate (T_1 = 132 ± 16 ms, T_2 = 15 ± 3 ms), and long relaxation times (T_1 = 226 ± 20 ms, T_2 = 54 ± 7 ms), respectively. Interestingly, these spectra are similar to those previously observed in peripheral nerve [4, 9, 10]. Also, the sizes of the spectral components (in order of increasing relaxation times) are in reasonable agreement with electron microscopy derived values of water content in the myelin, interaxonal, and axonal spaces, respectively, of crayfish abdominal nerve [30] — a model tissue for mammalian white matter.

T_1–T_2 spectra from Gd-enhanced white matter signal (Fig. 6.2c) also revealed three components in total, but were biexponential in either T_1 or T_2, which is consistent with previous measures in *normal white matter* [13, 31]. The unlabeled short-T_1 component in these spectra is thought to arise due to MT effects (as discussed below), while the two long-T_1 components are thought to represent distinct water compartments in white matter. Considering only signal arising from these water compartments, mean signal fractions across samples were 14 ± 2 and 86 ± 2 % for short- (T_1 = 337 ± 10 ms, T_2 = 15 ± 4 ms) and long-T_2 components (T_1 = 281 ± 11 ms, T_2 = 45 ± 3 ms), respectively. As in normal white matter, the long-T_2 component observed in Gd-enhanced white matter is thought to represent a combination of axonal and interaxonal water, while the short-T_2 component is thought to represent myelin water [11-15].

Sample grey matter T_1–T_2 spectra are shown in Fig. 6.3 (from cortical and sub-cortical ROIs in Fig. 6.1). Similar to white matter, chromation of grey matter resulted in multiple relaxation components that were unique in both T_1 and T_2. Gd-enhanced grey matter also presented similarly to its corresponding signal from white matter. Differences in the short-T_2 component

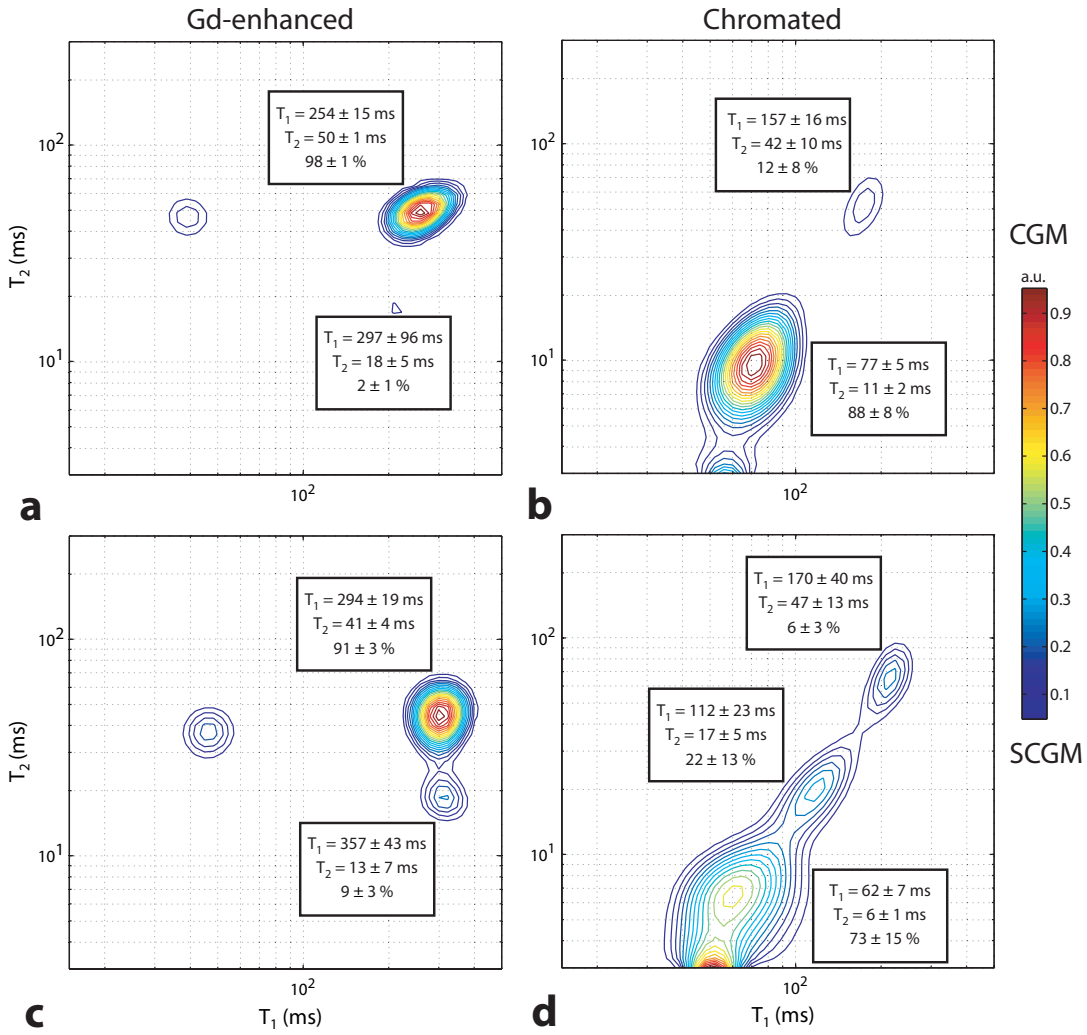

Fig. 6.3. Sample normalized grey matter T_1–T_2 spectrum for Gd-enhanced (a & c) and chromated (b & d) brains. Spectra from cortical (CGM, a & b) and sub-cortical (SCGM, c & d) grey matter signal are shown along with the component relaxation times and signal fractions averaged across samples. Spurious components along with those likely arising from MT effects [unlabeled short-T_1 component in (a & c)] were ignored in the pool fraction calculation.

signal fraction found in Gd-enhanced white matter (14 ± 2 %), cortical grey matter (2 ± 1 %), and sub-cortical grey (9 ± 3 %) matter are thought to reflect differences in myelin content within each of these ROIs.

The short-T_1 component in the Gd-enhanced rat brain T_1–T_2 spectra (Figs. 6.2c, 6.3a, and 6.3c) is thought to arise from MT effects [39]. Simply put, the relatively low power inversion pulse used is thought to invert the free water pool, while having minimal effect on the semi-solid proton pool. Exchange of magnetization between these pools then results in a biexponential recovery of the free water longitudinal magnetization. This interpretation is supported by the fact that this component was suppressed when a high power inversion pulse was used (data not shown). Although the magnitude of this component is thought to correlate to myelin content, the microanatomical origin of this component and its relationship to the myelin water fraction remains unclear. In chromated tissue, no such short-T_1 component was observed, possibly because it was simply too short or too close to other spectral components to be resolved.

Optic Nerve Studies

T_1–T_2 spectra from control and chromated rat optic nerve are given in Fig. 6.4. For control optic nerve, two signal components were observed, which is consistent with studies performed by Stanisz *et al*. in bovine optic nerve [32, 33]. Across samples, mean signal fractions were 14 ± 1 and 86 ± 1% for components with short (T_1 = 987 ± 29 ms, T_2 = 9 ± 1 ms) and long relaxation times (T_1 = 1279 ± 48 ms, T_2 = 83 ± 10 ms), respectively. Following chromation, three signal components were observed, consistent with our finding in chromated cerebral white matter. Across samples, mean signal fractions were 10 ± 2, 54 ± 12 and 36 ± 11 for components with short (T_1 = 39 ± 5 ms, T_2 = 8 ± 2 ms), intermediate (T_1 = 125 ± 8 ms, T_2 = 25 ± 1 ms), and long

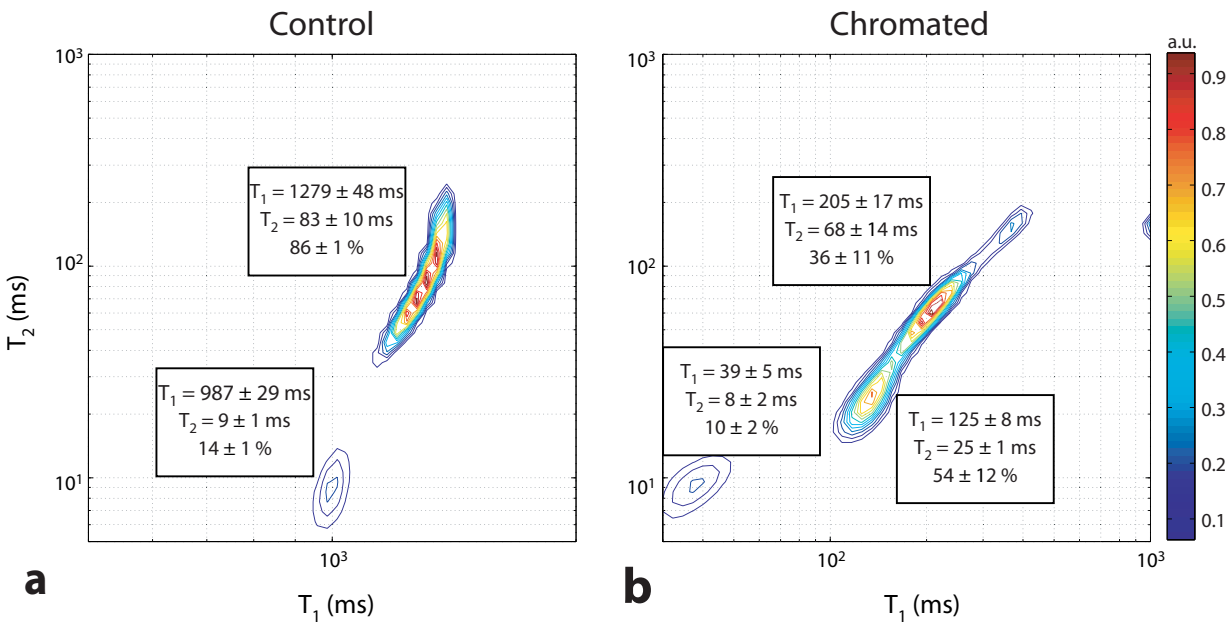

Fig. 6.4. Sample normalized T_1–T_2 spectrum for control (a) and chromated (b) optic nerves along with the component relaxation times and signal fractions averaged across samples. Spurious components were ignored in the pool fraction calculation.

relaxation times (T_1 = 205 ± 17 ms, T_2 = 68 ± 14 ms), respectively.

To ensure that tissue integrity was preserved during the period required to chromate and wash the tissue, three samples were prepared for light microscopy. The first was fixed immediately after excision, the second was chromated and washed prior to fixation, and the third was placed in PBS at 4 ˚C for a 12-hour period. The resultant light microscopy is shown in Fig. 6.5. It can be seen that the tissue integrity is reasonably preserved in the samples not fixed immediately. Similar data obtained from normal and chromated rat spinal cord showed no morphological changes following chromation and washing periods of up to 12 hours (data not shown). These results suggest that a window of up to 12 hours is available for reagent loading and washing.

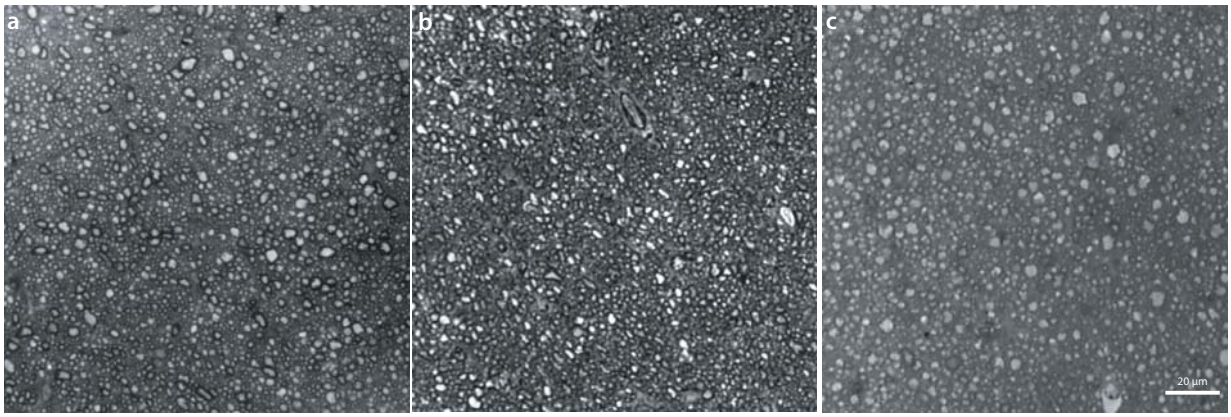

Fig. 6.5. Toluidine blue stained rat optic nerve sections taken from (a) nerve fixed immediately after excision, (b) nerve that was chromated and washed prior to fixation, and (c) nerve placed in PBS for 12 hours prior to fixation.

Sciatic Nerve Studies

T_1–T_2 spectra from control and chromated frog sciatic nerve are given in Fig. 6.6. For control samples, three signal components were observed that were similar in relaxation times and signal fractions to previously published measurements [10]. Three corresponding signal components were observed in chromated sciatic nerve. For each of these components, the increase in relaxation rate ($R_{1,2} = 1/T_{1,2}$) as a result of chromation is expected to scale linearly with the local concentration of paramagnetic chromium. Thus, the change in compartmental relaxation rates for chromated relative to control nerve ($\Delta R_{1,2}$) was tabulated from the relaxation times given in Fig. 6.6, the results of which are given in Table 6.1. It can be seen that the components with short and intermediate relaxation times, believed to be derived from myelin and interaxonal water, show a significantly larger ΔR_1 as a result of chromation compared to the component with long relaxation times, which is believed to be derived from axonal water [6, 8]. This indicates that paramagnetic chromium does not gain access to the axonal space to the same degree as the other spaces in these samples (see *Discussion* for details).

Table 6.1. Change in component relaxation rates ($\Delta R_{1,2}$) for chromated and Gd-enhanced relative to control peripheral nerve. Shown are the results for components with short, intermediate, and long relaxation times given in Fig. 6.6.

		Short	*Intermediate*	*Long*
Chromated	ΔR_1 (s^{-1})	3.9 ± 0.3	3.0 ± 0.5	0.2 ± 0.1
	ΔR_2 (s^{-1})	22.1 ± 17.1	7.1 ± 3.3	-0.4 ± 1.0
Gd-enhanced	ΔR_1 (s^{-1})	0.9 ± 0.1	1.5 ± 0.1	0.3 ± 0.1
	ΔR_2 (s^{-1})	16.5 ± 24.6	2.7 ± 3.1	-0.1 ± 0.9

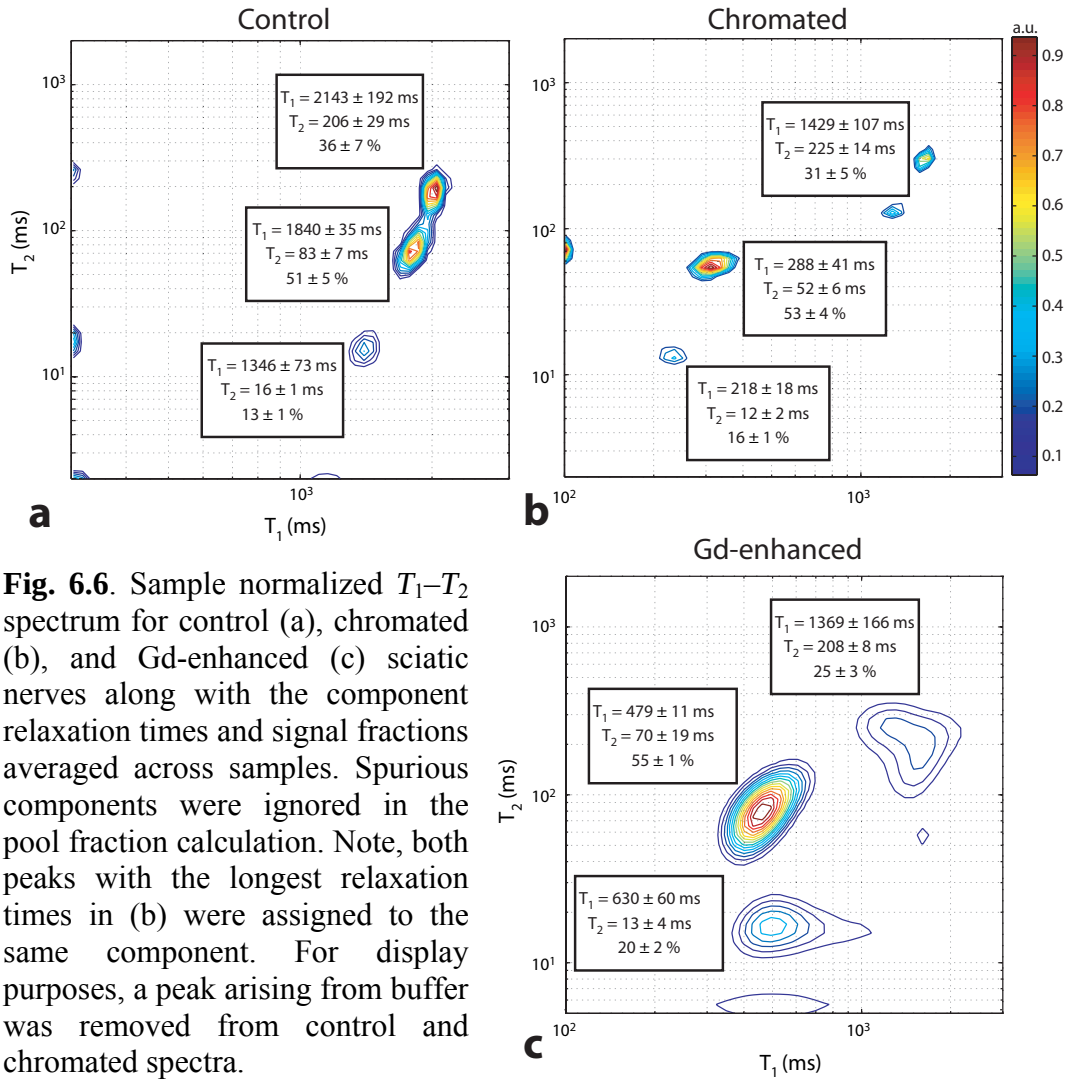

Fig. 6.6. Sample normalized T_1–T_2 spectrum for control (a), chromated (b), and Gd-enhanced (c) sciatic nerves along with the component relaxation times and signal fractions averaged across samples. Spurious components were ignored in the pool fraction calculation. Note, both peaks with the longest relaxation times in (b) were assigned to the same component. For display purposes, a peak arising from buffer was removed from control and chromated spectra.

For comparison, similar measurements were also performed in Gd-enhanced frog sciatic nerve, the results of which are given in Fig. 6.6 and Table 6.1. Three components were observed in Gd-enhanced nerve with similar signal fractions as observed in control and chromated nerve. As shown in Table 6.1, a different compartmental enhancement pattern was observed in Gd-enhanced than was observed in chromated nerve. Specifically, the component with intermediate relaxation times, believed to represent interaxonal water, showed a larger ΔR_1 compared to the components with short and long relaxation times, believed to represent myelin and axonal water, respectively. This suggests that the compartmental concentration (or relaxivity) of Gd-DTPA is greatest in the interaxonal space followed by myelin and axonal spaces.

Discussion

Previous work [16] has shown that ICV administration of potassium dichromate *in vivo* results in relaxation changes in white matter. This enhancement is thought to arise due to reduction of diamagnetic Cr(VI) to paramagnetic chromium species (Cr(V) and/or Cr(III)) by oxidizable lipids in myelin. The purpose of the studies herein was to better understand the compartmental basis of these relaxation changes by using multiexponential relaxation analysis, which is known to reflect the microanatomical compartition of water in nerve and white matter. In order to achieve the necessary SNR for such analysis, these studies were performed *ex vivo*.

It should be noted that the results herein were substantially different than previously reported results *in vivo* [16]. Watanabe *et al.* noted significant contrast-enhancement in white matter and only mild enhancement in grey matter *in vivo* after a low-dosage ICV injection of potassium dichromate. This was thought to arise because: (i) white matter has a substantially higher lipid content than does grey matter and (ii) myelin lipids possess a higher reactivity

towards Cr(VI) than do grey matter reductants. In the current study, however, a larger mean contrast-enhancement was found in grey matter than in white matter (as evidenced by comparing T_1 values from Figs. 6.2 and 6.3). One possible explanation for this is myelin lipid oxidation was saturated at the high concentration of potassium dichromate used herein, and Cr(VI) was reduced by the next available reductant in grey matter. Also, lipids oxidize rapidly following death, thus the distribution of available reductants, giving time for potassium dichromate to diffuse into the brain, is likely different *ex vivo* compared to *in vivo*.

Microanatomical Origins of Chromation

In peripheral nerve, previous studies (as well as the current one) have resolved three distinct components in T_1–T_2 water relaxation spectra [4, 9, 10], and a sizeable body of literature has related these components to myelin, interaxonal, and axonal water, in order of increasing relaxation times [3, 5, 6, 8, 13, 30]. From Fig. 6.6, it is apparent that axonal water is relatively unaffected by chromation in comparison to myelin and interaxonal water. One possible explanation for this is that diamagnetic Cr(VI), which has been shown to readily cross cell membranes [21, 34], is distributed throughout all nerve compartments, but is not reduced (i.e., "turned on") within axonal spaces due to a lack of available reductants. Another, perhaps more likely, possibility is that Cr(VI) does not gain access to the axonal space (to the same degree as the other spaces) because of the presence of the myelin sheath, which possesses a high content of oxidizable lipids. The natural interpretation is that Cr(VI) ions cannot penetrate through the entire thickness of the myelin sheath without being reduced. Reduced paramagnetic chromium ions are then prevented from entering the axonal space because: (i) they do not readily cross cell membranes [21, 34] and/or (ii) they remain bound or complexed to oxidized myelin lipids.

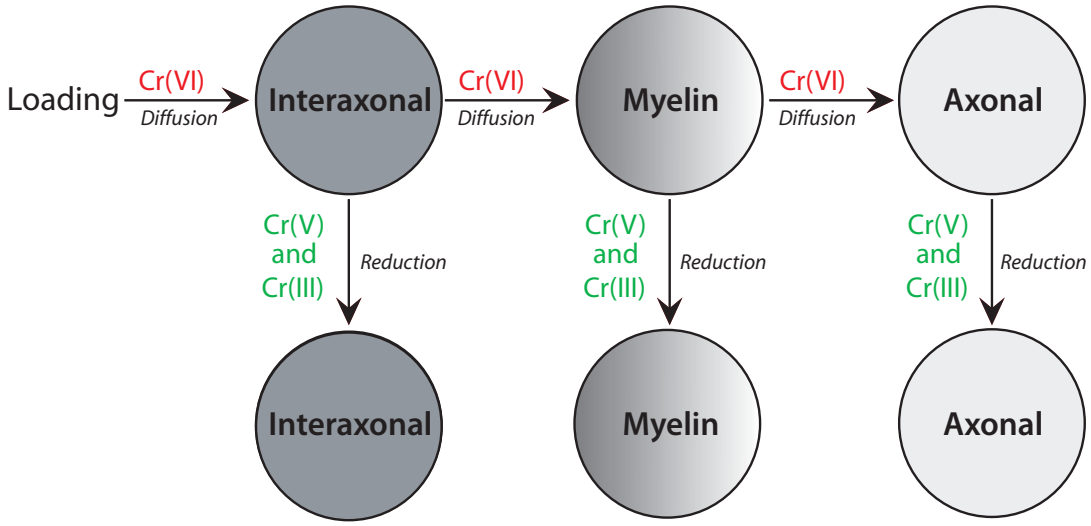

Fig. 6.7. Model of the observed enhancement pattern in chromated myelinated tissue. The shading for each compartment represents its relative access to diamagnetic Cr(VI), with darker shading representing greater Cr(VI) access. Cr(VI) is loaded into the interaxonal compartment and gains access to the other compartments *via* diffusion. The myelin sheath acts as a barrier for Cr(VI) diffusion into the axoplasm because Cr(VI) is reduced by myelin lipids as it traverses the myelin sheath. Therefore, though each individual compartment likely contains reductants, which "turn on" enhancement, axonal water enhancement is limited by its access to Cr(VI).

With this interpretation in peripheral nerve, the observations of relaxation changes in chromated white matter and optic nerve follow similarly. It is postulated that the myelin sheath reduces axonal access of paramagnetic chromium, resulting in smaller contrast-enhancement of axonal relative to interaxonal water and the ability to resolve each component. Therefore, in Fig. 6.2d and Fig. 6.4b, the spectral component with the longest relaxation times is believed to be axonal water, and (similar to peripheral nerve) the two components with shorter relaxation times are believed to be myelin and interaxonal water. This interpretation is summarized using the model shown in Fig. 6.7.

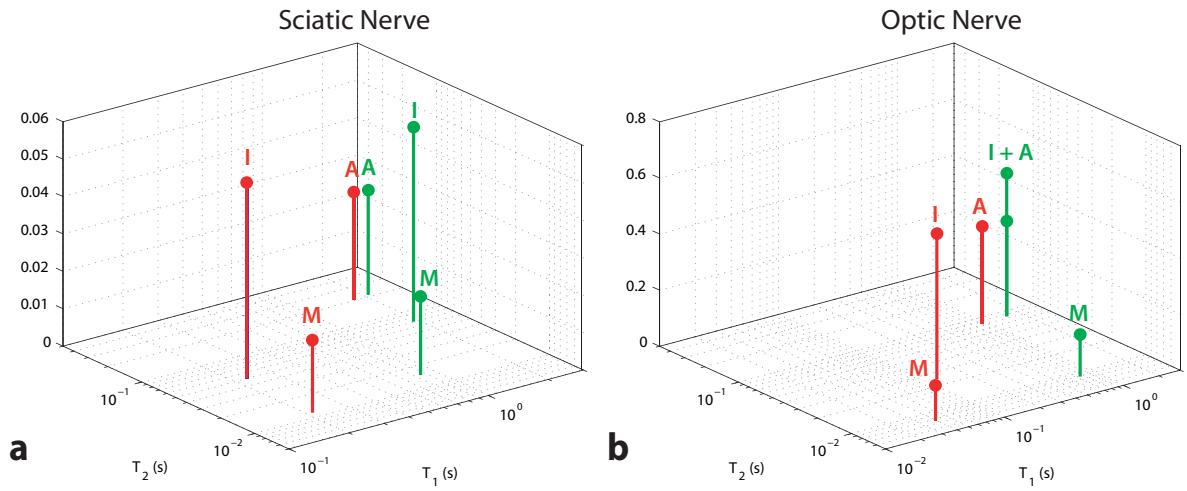

Fig. 6.8. Simulated T_1-T_2 spectra for chromated sciatic and optic nerve using the exchange model parameters defined in Table 5.1 and 5.2. Simulations were performed for no enhancement (green) and interaxonal and myelin water enhancement (red). Relaxation times following enhancement were assumed to be the values in Figs. 6.4b and 6.6b for optic and sciatic nerve, respectively. The relative signal fractions for axonal and interaxonal water in optic nerve were assumed to be the values reported in Fig. 6.4b. M – myelin water; A – axonal water; I – interaxonal water.

Note that, unlike peripheral nerve, white matter and optic nerve axonal relaxation times were significantly reduced in chromated tissue relative to normal tissue ($T_1 > 1$ s). This indicates that in these tissues: (i) some paramagnetic chromium does reach the axonal space and/or (ii) water exchange between the myelin and axonal compartments is sufficient to alter the apparent relaxation time in the axonal space. Both of these scenarios are reasonable given the thinner myelin sheath thickness in white matter and optic nerve (0.1–0.6 μm [35]) compared to peripheral nerve (0.2–2.0 μm [36]) and the faster exchange in optic nerve relative to sciatic nerve (as shown in Chapter V). To test the effect of exchange, T_1-T_2 data were generated from Eq. (3.17) using the fitted exchange model parameters in Tables 5.1 and 5.2. Data were generated for two scenarios. In the first scenario, data were generated using the intrinsic relaxation rates (in Tables 5.1 and 5.2) to simulate normal tissue. In the second scenario, interaxonal and myelin

relaxation rates were increased (using the values listed in Figs. 6.4b and 6.6b) to simulate chromation. As shown in Fig. 6.8, axonal water apparent relaxation times are relatively unaffected by exchange following chromation in both tissues. As a result, it is likely that paramagnetic chromium does reach the axonal space in optic nerve and white matter (and to a much lesser degree in sciatic nerve).

Another consideration in terms of the different enhancement pattern observed in white matter and optic nerve relative to peripheral nerve is the different chromation/washing periods used for each tissue: rat brains (72 hrs / 7 days), optic nerve (1 hr / 3 hrs), and sciatic nerve (1 hr / 1 hr). In spite of using very different chromation/washing periods, the compartmental enhancement pattern for chromated optic nerve and rat brain were similar. This indicates that the larger axonal enhancement observed in rat brains and optic nerve relative to peripheral nerve is likely reflective of differences in myelin sheath thickness, not differences in the chromation/washing periods used.

In chromated grey matter (Figs. 6.3b and 6.3d), a large fraction of the signal (88 ± 8 % in cortical ROIs and 73 ± 15 % in sub-cortical ROIs) was substantially reduced in T_1 and T_2, while the remaining signal was affected to a lesser degree. Assuming exchange is fast (on the T_2 timescale) between compartments that are not partitioned by the myelin sheath, the most reasonable explanation for these multiple relaxation components is the presence of myelinated axons within the grey matter ROIs used. Thus, using the same reasoning as in white matter, the components affected to a lesser degree (i.e, with the longest relaxation times) in grey matter are thought to represent water within myelinated axons. Supporting this presumption, pool fractions for these components were of similar magnitude to electron microscopy derived estimates of water content within myelinated axons in primate visual cortex [37]. Note, the reason that two

longer relaxation time components were found in chromated sub-cortical grey matter (Fig. 6.3d) is unclear. Furthermore, some of the so-called axonal component observed in chromated grey matter (as well as the myelin component in Gd-enhanced grey matter) may result from partial-volume averaging with white matter, especially considering the relatively large grey matter ROIs used (Fig 6.1b).

Microanatomical Origins of Gd-enhancement

Gd-enhancement of fixed white matter resulted in a noticeably different T_1–T_2 spectrum compared to chromated white matter. In these samples, signal was found to be biexponential in T_2, which is consistent with many studies of normal white matter that have identified a short-T_2 component arising from myelin water [11-15]. In Gd-enhanced grey matter, similar results were obtained to those found in white matter, with a smaller contribution from the short-T_2 component representing myelin water. This is in conflict with previous measurements [9] in normal grey matter that have reported monoexponential decay. The fact that multiple relaxation components were not previously resolved, may be due to SNR limitations of the previous study ($\approx 5\times$ lower than the present study) coupled to the small size one would expect for this component (i.e., the fractional volume of myelinated axons is relatively small in grey matter).

In fresh tissue, Gd-chelates typically do not cross intact cell membranes, which is consistent with the relatively small axonal enhancement observed in Gd-enhanced fresh frog sciatic nerve (Fig. 6.6c and Table 6.1). In formalin fixed tissue, Gd-chelates have been shown to cross cell membranes [38], which is consistent with our findings in formalin fixed white matter (Fig. 6.2c). To further test this, formalin fixed rat sciatic nerve samples (n = 10) were excised and loaded with a range of Gd-DTPA concentrations. Compartmental relaxation rates were

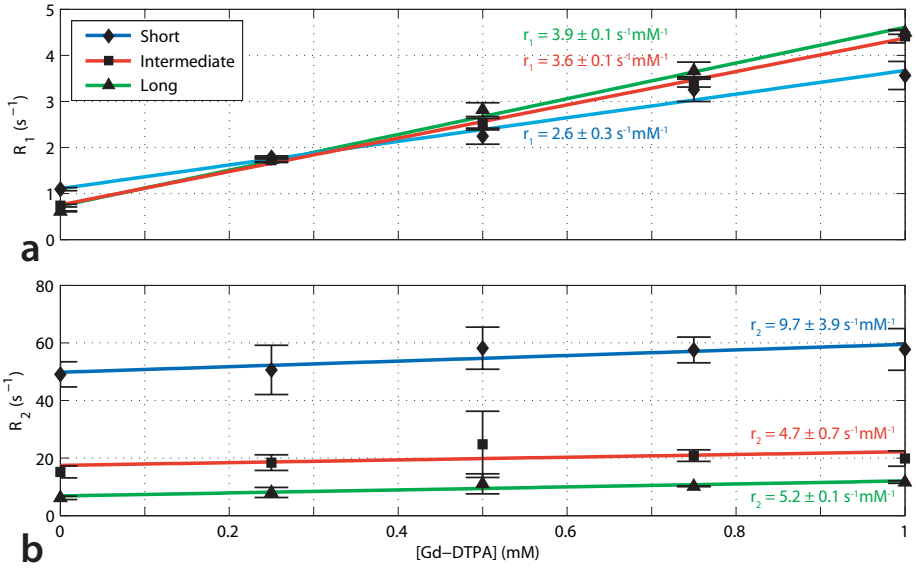

Fig. 6.9. R_1 (a) and R_2 (b) as a function of Gd-DTPA concentration in formalin fixed rat sciatic nerve. The errorbars represent the standard deviation across samples (n = 2 for each concentration). Each set of data was fitted to a linear model. The slope, or relaxivity (r_1 or r_2), is given for each of these fits. *Short* = component with short relaxation times; *Intermediate* = component with intermediate relaxation times ; *Long* = component with long relaxation times.

determined for each sample and were fitted to a linear model. The slope of this fit, or relaxivity, was then used as a measure of each compartment's relative access to Gd-DTPA. As shown in Fig. 6.9, the relaxivity (with respect to R_1) of each compartment was similar in fixed nerve, suggesting that the compartmental distribution of Gd-DTPA was relatively homogeneous in these samples.

Complicating Factors

One important issue to consider in excised chromated tissue is the extent to which tissue integrity is preserved. The results shown in Fig. 6.5 suggest that this integrity was preserved in optic nerve. Results from similar analysis in cerebral white matter, however, suggest a loss of tissue integrity during the much longer chromation and washing period used in brain (data not shown).

Though potassium dichromate has some value as a fixative, it is seldom used alone [40]. Unfortunately, attempts to incorporate aldehyde fixatives before, during, and after chromation resulted in a "non-specific" enhancement pattern. This can most likely be attributed to: i) increased membrane permeability following fixation (as observed in formalin fixed Gd-enhanced tissue) and ii) the fact that aldehydes are reductants themselves, likely reducing Cr(VI) before the reaching the targeted reductants in tissue.

In spite of these limitations, a similar compartmental enhancement pattern, with similar signal fractions for each compartment, was observed in chromated optic nerve (Fig. 6.4b) and cerebral white matter (Fig. 6.4d). This suggests that the results in chromated white matter may indeed reflect underlying tissue microstructure. Given that this claim has yet to be substantiated, one may wish to limit chromation studies to smaller volume tissue samples (e.g., mouse brain, spinal cord) where reagents can be rapidly loaded and washed.

Future Work

The ability to isolate signal from axonal and interaxonal water in chromated myelinated tissue may be a powerful tool for studying, amongst other things, the compartmental origin of diffusion and MT in white matter and optic nerve. Furthermore, chromation may provide a means for performing compartmental MR microscopy by allowing compartmental signals to be filtered (using the appropriate magnetization preparation scheme) based upon differences in T_1 [10], T_2 , or both [41]. As proof of concept, axonal signal from IR-ME data was selected based upon T_2 (Fig. 6.10). At TE = 71.5 ms, signal from myelin and interaxonal water has nearly decayed to baseline, leaving only signal from axonal water. In other words, the magnitude of this image is thought to correlate with the percentage of water within myelinated axons for each voxel,

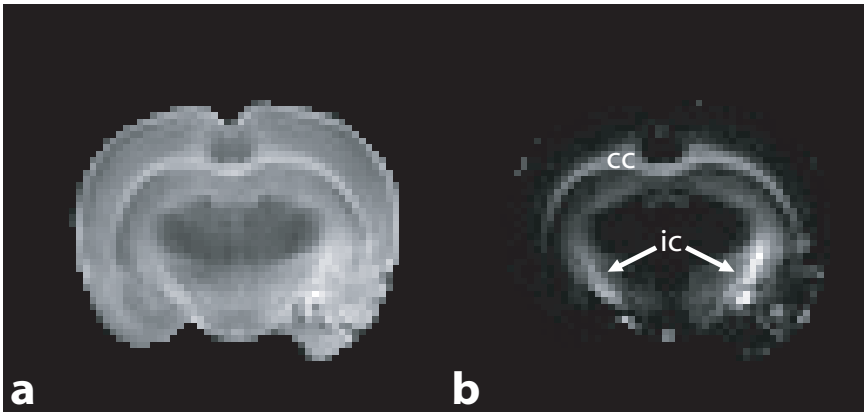

Fig. 6.10. Normalized images from chromated brain at TE = 6.5 ms (a) and 71.5 ms (b). In (b), the signal from both myelin and interaxonal water has nearly decayed to baseline, while residual signal from axonal water remains. Note, that substantial signal remains within the corpus callosum (cc) and internal capsule (ic).

supported by the high signal intensity found in both the corpus callosum and internal capsule. A more quantitative approach would be to calculate the fractional area under the long relaxation time component, or myelinated axon water fraction, using T_1–T_2 spectra from each voxel. This would correct for regional differences in contrast-enhancement, especially those found between white and grey matter. The high SNR per voxel required for this type of analysis is an obvious limiting factor, especially in grey matter where the mean relaxation times were relatively short.

Conclusions

Using T_1–T_2 measurements, signal from axonal and interaxonal water was resolved in chromated white matter and optic nerve. Separation of axonal and interaxonal water is thought to arise because myelin acts as a barrier for axonal access to paramagnetic chromium, resulting in its smaller relative contrast-enhancement. T_1–T_2 measurements in frog sciatic nerve, a well-characterized three-component system, support this postulation. Work is under way to exploit the

improved anatomical resolution available through chromation *ex vivo* as well as to validate findings histologically.

Acknowledgements

The authors would like to thank Dr. Bill Valentine and Dr. Holly Valentine for their useful consultation regarding lipid oxidation and Greg Apker for his help performing the frog nerve studies.

References

[1] V. Vasilescu, E. Katona, V. Simplaceanu, and D. Demco, "Water compartments in myelinated nerve. 3. Pulsed NMR results," *Experientia*, vol. 34, pp. 1443–1444, 1978.

[2] M. D. Does and R. E. Snyder, "T_2 relaxation of peripheral nerve measured in-vivo," *Magn Reson Imaging*, vol. 13, pp. 575–580, 1995.

[3] M. Does and R. Snyder, "Multiexponential T_2 relaxation in degenerating peripheral nerve," *Magn Reson Med*, vol. 35, pp. 207–213, 1996.

[4] M. D. Does, C. Beaulieu, P. S. Allen, and R. E. Snyder, "Multi-component T_1 relaxation and magnetisation transfer in peripheral nerve," *Magn Reson Imaging*, vol. 16, pp. 1033–1041, 1998.

[5] C. Beaulieu, F. R. Fenrich, and P. S. Allen, "Multicomponent water proton transverse relaxation and T_2-discriminated water diffusion in myelinated and nonmyelinated nerve," *Magn Reson Imaging*, vol. 16, pp. 1201–1210, 1998.

[6] S. Peled, D. G. Cory, S. A. Raymond, D. A. Kirschner, and F. A. Jolesz, "Water diffusion, T_2, and compartmentation in frog sciatic nerve," *Magn Reson Med*, vol. 42, pp. 911–918, 1999.

[7] G. Stanisz, R. Midha, C. Munro, and R. Henkelman, "MR properties of rat sciatic nerve following trauma," *Magn Reson Med*, vol. 45, pp. 415–420, 2001.

[8] K. Wachowicz and R. E. Snyder, "Assignment of the T_2 components of amphibian peripheral nerve to their microanatomical compartments," *Magn Reson Med*, vol. 47, pp. 239–245, 2002.

[9] M. D. Does and J. C. Gore, "Compartmental study of T_1 and T_2 in rat brain and trigeminal nerve in vivo," *Magn Reson Med*, vol. 47, pp. 274–283, 2002.

[10] A. R. Travis and M. D. Does, "Selective excitation of myelin water using inversion-recovery-based preparations," *Magn Reson Med*, vol. 54, pp. 743–747, 2005.

[11] R. S. Menon and P. S. Allen, "Application of continuous relaxation-time distributions to the fitting of data from model systems and excised tissue," *Magn Reson Med*, vol. 20, pp. 214–227, 1991.

[12] W. A. Stewart, A. L. Mackay, K. P. Whittall, G. R. W. Moore, and D. W. Paty, "Spin-spin relaxation in experimental allergic encephalomyelitis: Analysis of CPMG data using a nonlinear least-squares method and linear inverse-theory," *Magn Reson Med*, vol. 29, pp. 767–775, 1993.

[13] A. Mackay, K. Whittal, J. Adler, D. Li, D. Paty, and D. Graeb, "In-vivo visualization of myelin water in brain by magnetic resonance," *Magn Reson Med*, vol. 31, pp. 673–677, 1994.

[14] R. Harrison, M. J. Bronskill, and R. M. Henkelman, "Magnetization-transfer and T_2 relaxation components in tissue," *Magn Reson Med*, vol. 33, pp. 490–496, 1995.

[15] P. J. Gareau, B. K. Rutt, C. V. Bowen, S. J. Karlik, and J. R. Mitchell, "In vivo measurements of multi-component T_2 relaxation behaviour in guinea pig brain," *Magn Reson Imaging*, vol. 17, pp. 1319–1325, 1999.

[16] T. Watanabe, R. Tammer, S. Boretius, J. Frahm, and T. Michaelis, "Chromium(VI) as a novel MRI contrast agent for cerebral white matter: Preliminary results in mouse brain in vivo," *Magn Reson Med*, vol. 56, pp. 1–6, 2006.

[17] K. J. Liu and X. Shi, "In vivo reduction of chromium (VI) and its related free radical generation," *Mol Cell Biochem*, vol. 222, pp. 41–47, 2001.

[18] H. Peemoeller and M. M. Pintar, "Two-dimensional time-evolution approach for resolving a composite free-induction decay," *J Magn Reson*, vol. 41, pp. 358–360, 1980.

[19] A. E. English, K. P. Whittall, M. L. Joy, and R. M. Henkelman, "Quantitative two-dimensional time correlation relaxometry," *Magn Reson Med*, vol. 22, pp. 425–434, 1991.

[20] J. E. M. Snaar and H. Vanas, "A method for the simultaneous measurements of NMR spin-lattice and spin-spin relaxation times in compartmentalized systems," *J Magn Reson*, vol. 99, pp. 139–148, 1992.

[21] M. Ding and X. L. Shi, "Molecular mechanisms of Cr(VI)-induced carcinogenesis," *Mol Cell Biochem*, vol. 234, pp. 293–300, 2002.

[22] M. S. Silver, R. I. Joseph, C. N. Chen, V. J. Sank, and D. I. Hoult, "Selective population inversion in NMR," *Nature*, vol. 310, pp. 681-683, 1984.

[23] M. H. Levitt and R. Freeman, "Compensation for pulse imperfections in NMR spin-echo experiments," *J Magn Reson*, vol. 43, pp. 65–80, 1981.

[24] C. S. Poon and R. M. Henkelman, "Practical T_2 quantitation for clinical applications," *J Magn Reson Imaging*, vol. 2, pp. 541–553, 1992.

[25] J. M. Bonny, O. Boespflug-Tanguly, M. Zanca, and J. P. Renou, "Multi-exponential analysis of magnitude MR images using a quantitative multispectral edge-preserving filter," *J Magn Reson*, vol. 161, pp. 25–34, 2003.

[26] C. L. Lawson and R. J. Hanson, *Solving Least Squares Problems*. Englewood Cliffs, NJ: Prentice-Hall, 1974.

[27] K. P. Whittall and A. L. Mackay, "Quantitative Interpretation of NMR Relaxation Data," *J Magn Reson*, vol. 84, pp. 134–152, 1989.

[28] L. Venkataramanan, S. Yi-Qiao, and M. D. Hurlimann, "Solving Fredholm integrals of the first kind with tensor product structure in 2 and 2.5 dimensions," *IEEE Trans Sig Proc*, vol. 50, pp. 1017–1026, 2002.

[29] H. Gudbjartsson and S. Patz, "The Rician distribution of noisy MRI data," *Magn Reson Med*, vol. 34, pp. 910–914, 1995.

[30] R. S. Menon, M. S. Rusinko, and P. S. Allen, "Proton relaxation studies of water compartmentalization in a model neurological system," *Magn Reson Med*, vol. 28, pp. 264–274, 1992.

[31] D. F. Gochberg and J. C. Gore, "Quantitative magnetization transfer imaging via selective inversion recovery with short repetition times," *Magn Reson Med*, vol. 57, pp. 437–441, 2007.

[32] G. Stanisz, A. Kecojevic, M. Bronskill, and R. Henkelman, "Characterizing white matter with magnetization transfer and T_2," *Magn Reson Med*, vol. 42, pp. 1128–1136, 1999.

[33] G. J. Stanisz and R. M. Henkelman, "Diffusional anisotropy of T_2 components in bovine optic nerve," *Magn Reson Med*, vol. 40, pp. 405–410, 1998.

[34] M. Travacio, J. M. Polo, and S. Llesuy, "Chromium(VI) induces oxidative stress in the mouse brain," *Toxicology*, vol. 150, pp. 137–146, 2000.

[35] R. W. Williams and L. M. Chalupa, "An analysis of axon caliber within the optic nerve of the cat: evidence of size groupings and regional organization," *J Neurosci*, vol. 3, pp. 1554–1564, 1983.

[36] R. L. Friede and W. Beuche, "A new approach toward analyzing peripheral nerve fiber populations. I. Variance in sheath thickness corresponds to different geometric proportions of the internodes," *J Neuropathol Exp Neurol*, vol. 44, pp. 60–72, 1985.

[37] A. Peters and C. Sethares, "Myelinated axons and the pyramidal cell modules in monkey primary visual cortex," *J Comp Neurol*, vol. 365, pp. 232–255, 1996.

[38] A. Purea and A. G. Webb, "Reversible and irreversible effects of chemical fixation on the NMR properties of single cells," *Magn Reson Med*, vol. 56, pp. 927–931, 2006.

[39] D. F. Gochberg, R. P. Kennan, and J. C. Gore, "Quantitative studies of magnetization transfer by selective excitation and T_1 recovery," *Magn Reson Med*, vol. 38, pp. 224–231, 1997.

[40] J. A. Kiernan, *Histological and Histochemical Methods: Theory and Practice*, 1st edition ed. New York: Pergamon Press, 1981.

[41] M. D. Does, "Relaxation-selective magnetization preparation based on T_1 and T_2," *Magn Reson Imaging*, vol. 172, pp. 306–311, 2005.

CHAPTER VII

COMPARTMENTAL CHARACTERIZATION OF RAT GLIOBLASTOMA *IN VIVO* USING MULTIEXPONENTIAL T_2 ANALYSIS

Introduction

The nuclear magnetic resonance (NMR) signal has been shown to exhibit multiexponential T_2 (MET_2) decay in a number of tissues (e.g., white matter [1, 2], peripheral nerve [3, 4], skeletal muscle [5]), arising from a combination of microanatomical water compartition (e.g., intracellular and extracellular water) and slow intercompartmental exchange. The goal of MET_2 analysis is to decompose bulk NMR signal into components that represent underlying tissue compartments. In doing so, one can probe individual tissue compartments that exist on a sub-voxel scale.

Given the heterogeneous nature of tumors, one might expect to observe MET_2 relaxation in tumors. In fact, MET_2 relaxation has been observed in animal models (both *in vivo* [6] and *ex vivo* [7]), surgical samples *ex vivo* [8, 9], and in humans *in vivo* [10], though results have been inconsistent. This inconsistency is presumably a product of differences in tumor types, models, and staging as well as differences in the data acquisition and analysis techniques used. Of these previous studies, only one [10] attempted to characterize MET_2 relaxation in tumors using an imaging approach (others used non-imaging CPMG [11, 12] approaches). In that particular study, T_2 measurements were made in human gliomas and the resultant signal was found to decay biexponentially; however, as the authors note, these results should be interpreted carefully due to the low signal-to-noise ratio (SNR) of the data.

The goal of this study was to characterize MET_2 relaxation in a rat glioblastoma tumor model. Towards this end, we performed Monte Carlo simulations as well as *in vivo* and *ex vivo* imaging experiments. The simulations were designed to see if the experimental imaging data achieved the appropriate SNR to perform region of interest (ROI) and/or voxel-based analyses. The *in vivo* data were acquired to characterize MET_2 relaxation in a commonly used tumor model, while the *ex vivo* measurements were acquired to ensure that the *in vivo* results were not significantly corrupted due to either partial-voluming or low SNR.

Materials and Methods

Simulations

Monte Carlo simulations were performed to determine the SNR requirements for MET_2 analysis of tumor signal. MET_2 decay curves, y_i were generated according to

$$y_i = \sum_{j=1}^{3} \left| s_j \exp(-t_i / T_{2,j}) + \varepsilon_i \right|, \quad i = 1, 2, ..., \mathrm{NE} \tag{7.1}$$

where s_j is the weight of the exponential component associated with $T_{2,j}$, NE is the total number of echoes, t_i is the echo time (TE) of the i^{th} echo, and ε_i is Gaussian noise added to the i^{th} echo.

Two sets of simulations were generated using Eq. (7.1) and the mean experimental values listed in Table 7.1. The first set was designed to simulate the biexponential decay observed *in vivo* (see Table 7.2), while the second set was designed to simulate the triexponential decay observed *ex vivo* (see Table 7.3). The decay curve sampling for each set was designed to match its corresponding decay curve sampling during experimental studies. Within each set, decay curves were generated with SNR values logarithmically spaced between 100 and 3200, where

Table 7.1. Parameters for simulated decay curves [Eq. (7.1)] where s_j is the weight of the exponential component associated with $T_{2,j}$, NE is the total number of echoes, and Δt is the inter-echo spacing. *In vivo*: Biexponential decay curves were generated using the mean component values listed in Table 7.2 (Components I and II) and the same echo sampling parameters used for *in vivo* measurements. *Ex vivo*: Triexponential decay curves were generated using the mean component values listed in Table 7.3 (Components I, I, and III) and the same echo sampling parameters used for *ex vivo* measurements.

Simulation	s_1	s_2	s_3	$T_{2,1}$ (ms)	$T_{2,2}$ (ms)	$T_{2,3}$ (ms)	Δt (ms)	NE
In vivo	0.07	0.93	-	21	76	-	8	32
Ex vivo	0.08	0.80	0.12	38	110	263	15	40

SNR is defined as the magnitude of the first echo divided by the standard deviation of the Gaussian noise. For a given SNR, 2000 decay curves (each with a unique noise realization) were generated and the bias introduced by the magnitude operation, which converts the underlying Gaussian noise to Rician, was removed (see *Data Analysis* for more details) [13]. MET_2 analysis was then performed to determine the distribution of T_2s (i.e., the T_2 spectrum) in the simulated data. This was done by minimizing

$$\sum_{i=1}^{\mathrm{NE}}\left\{\sum_{j=1}^{J}\left(s_j \exp(-t_i / T_{2,j}) - y_i\right)^2\right\} + \mu\sum_{j=2}^{J-1}\left(s_{j-1} - 2s_j + s_{j+1}\right)^2 \tag{7.2}$$

in a non-negative least-squares (NNLS) [14] sense using J = 100 logarithmically spaced relaxation times over the interval $t_1/2 < T_{2,j} < 2t_{NE}$. The first term in Eq. (7.2) minimizes data misfit, while the second term regularizes the solution by imposing a minimum curvature constraint [15], which smoothes the resultant spectrum according to the magnitude of the

regularizer term, μ. For this study, the value of μ was determined in a two-step process. First, μ was iteratively updated to determine the value that increased the χ^2 misfit by 2% relative to the unregularized fit (μ = 0) for each unique decay curve [16]. Second, the median μ across data with the same SNR was determined, and was subsequently used in a final regularized fit so that all T_2 spectra from data with the same SNR were smoothed to the same degree.

Each spectral peak, n, and its corresponding range of relaxation times $T_{2,n,\min} < T_{2,j} < T_{2,n,\max}$, was identified using an automated peak- and valley-finding algorithm (based upon locating zero-crossings of the first-derivative of the spectrum). For all non-spurious components (defined here as any peak that was consistently observed and represented more than 1% of the total signal), relaxation times and signal fractions were then calculated from

$$\overline{T}_{2,n} = \frac{\sum_{j=n,\min}^{n,\max} T_{2,j} s_j}{\sum_{j=n,\min}^{n,\max} s_j} \tag{7.3}$$

and

$$p_n = \frac{\sum_{j=n,\min}^{n,\max} s_j}{\sum_{j=1}^{J} s_j}, \tag{7.4}$$

respectively. Spectra were deemed admissible if the expected components (two for *in vivo* and three for *ex vivo* simulations, respectively) were resolved. The percentage of admissible spectra,

or admissibility, was then calculated for each SNR value to determine the SNR requirements for MET_2 analysis.

Animal Preparation

All procedures were approved by our Institution's Animal Care and Usage Committee. Male Wistar rats (n = 11) were immobilized and anesthesia was induced and maintained with a 2%/98% isofluorane/oxygen mixture (Minrad Inc., Bethlehem, PA). Rats were then inoculated with 1×10^5 C6 gliosarcoma cells using a 10-μL gastight syringe approximately one mm anterior and two mm lateral to bregma on the right side of the head, at a depth of three mm relative to the dural surface. C6 is a common glioblastoma model that is widely used in experimental neuro-oncology to evaluate tumor growth, invasion, migration, and blood-brain-barrier disruptions, and has been used extensively to investigate the efficacy of various therapies including chemotherapy and radiation therapy [17]. *In vivo* MRI was performed 14 to 21 days (see Table 7.2 for details) after this procedure.

After *in vivo* imaging, a transcardial perfusion was performed in three of the eleven animals described above. During this procedure, animals were immobilized and anesthesia was induced and maintained with a 2%/98% isofluorane/oxygen mixture. A 23-g needle was inserted into the left ventricle of the heart and phosphate-buffered saline (PBS; Mediatech Inc., Herdon, VA) was perfused to flush the blood out of the vascular system, at which point the perfusate was changed to 10% neutral buffered formalin (VWR, West Chester, PA). Following perfusion, brains were extracted and stored in 10% neutral buffered formalin overnight. Brains were then stored in PBS (to remove excess fixative) until *ex vivo* MRI was performed.

In vivo Magnetic Resonance

Rats (n = 11) were imaged using a 7.0-T, 16-cm bore Varian INOVA spectrometer (Varian Inc., Palo Alto, CA). A 63-mm inner diameter quadrature volume coil was used for RF transmission and reception. During imaging, animals were anesthetized with a 2%/98% isofluorane/oxygen mixture and temperature was maintained at 37 ºC with a rectal thermometer and warm-air feedback system. Respiratory signals were also monitored using a small pneumatic pillow placed near the rat's abdomen (SA Instruments, Stony Brook, NY).

For each rat, a single 1.5-mm axial slice through the center of the tumor volume was first selected from T_2-weighted scout images (Fig. 7.1a). T_2 measurements were then made using a single-slice, multi-echo spin-echo sequence [18] with an echo spacing (ΔTE) = 8 ms, TR = 4 s, number of echoes (NE) = 32, field of view = 35 × 35 mm^2, acquisition matrix = 64 × 64, in-plane resolution = 547 × 547 μm^2, acquisition bandwidth = 50 kHz, number of averages (NEX) = 8, and total imaging time ≈ 34 minutes. Spoiler gradients were placed about each $90_x180_y90_x$ broadband composite refocusing pulse [19] in an alternating and descending fashion [18] in order to remove signal from unwanted coherence pathways. The spoiler gradients were calculated so as to cause a minimum phase dispersion of $\pi/2$ across one slice thickness, which was found to be sufficiently large to remove these unwanted signal components.

Ex vivo Magnetic Resonance

Excised brains (n = 3) were imaged at bore temperature (≈ 20 ºC) using a 7.0-T, 16-cm bore Varian INOVA spectrometer and 38-mm diameter Litz RF coil (Doty Scientific, Columbia, SC). For imaging, brains were placed in a custom-built holder and bathed in fresh PBS. To minimize

air bubbles, both the brain and holder were fully immersed in PBS while loading the brain into the holder.

A single 1-mm axial slice through the center of the tumor volume (representing approximately the same slice acquired *in vivo*) was first selected from T_2-weighted scout images (Fig. 7.1b). Imaging was then performed using the same multiple-spin echo sequence as described for *in vivo* imaging, but at higher resolution and SNR. Relevant parameters for *ex vivo* T_2 measurements included ΔTE = 15 ms, TR = 4 s, NE = 40, field of view = 19.2 × 19.2 mm^2, acquisition matrix = 64 × 64, in-plane resolution = 300 × 300 μm^2, acquisition bandwidth = 40 kHz, NEX = 64, and total imaging time ≈ 4 ½ hours. Note the echo spacing used for *ex vivo* acquisitions (15 ms) was longer than for *in vivo* acquisitions (8 ms). This was to ensure that the decay curve was adequately sampled *ex vivo* because: 1) the observed relaxation times *ex vivo* were generally longer than corresponding relaxation times *in vivo* and 2) an additional long-lived component was observed *ex vivo* (see *Results*).

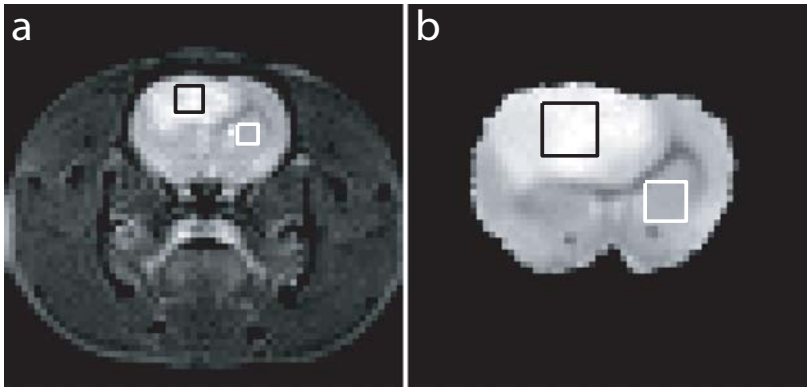

Fig. 7.1. (a) Representative T_2-weighted images acquired *in vivo* (TE = 40 ms) along with representative ROIs for tumor (black box) and normal (contralateral subcortical grey matter, white box) tissue. (b) Corresponding *ex vivo* image (TE = 30 ms) from the same animal (Rat #10).

Data Analysis

All data analysis was performed using routines written in-house in MATLAB (Mathworks, Natick, MA). For ROI-based analysis, tumor and contralateral subcortical grey matter ROIs were defined from T_2-weighted scout images (as shown in Fig. 7.1). Tumor ROIs were defined to encompass as much of the tumor as possible, while avoiding the tumor margin where significant partial-voluming of tumor and normal tissue may occur. Once defined, the maximum-likelihood estimator of each Rician-distributed ROI value was determined [13]. This approach has been shown to minimize bias introduced by the Rician noise present in magnitude MR images, especially for those images acquired with low SNR (i.e., at longer echo times). T_2 spectra were then determined by minimizing Eq. (7.2) as described for simulated data. For these fits, the regularizer parameter, μ, was iteratively updated to determine the value that increased the χ^2 misfit by 2% relative to the unregularized fit for each individual ROI. The median μ across samples – 0.15 and 0.01 for *in vivo* and *ex vivo* data, respectively – was then determined and used in a final regularized fit. Component relaxation times and signal fractions were calculated for each non-spurious component in the resultant T_2 spectra from Eqs. [3] and [4], respectively.

Simulations indicated (see *Results* for details) that the SNR per voxel was insufficient to perform voxel-based MET_2 analysis. Therefore, to increase SNR, *in vivo* and *ex vivo* images were spatially filtered by applying a multichannel (with each echo representing a different channel) anisotropic diffusion filter [20] prior to voxel-based MET_2 analysis. This approach has been previously applied to MET_2 analysis [21] and has been shown to reduce variability with minimal introduction of bias due to partial-voluming. After filtering, T_2 spectra were determined for each voxel by minimizing Eq. (7.2) with μ = 0.07 and 0.01 for *in vivo* and *ex vivo* data, respectively (determined using an analogous approach to that used for ROI-based analyses). For

each voxel's T_2 spectrum, component relaxation times [Eq. (7.3)] and signal fractions [Eq. (7.4)] were calculated.

All values are given as mean (± SD) across samples unless otherwise reported.

Results

Simulations

Fig. 7.2a displays the admissibility of MET_2 analysis for *in vivo* and *ex vivo* simulated data as a function of SNR. For *ex vivo* data, the admissibility for resolving all three observed components as well as resolving the short-lived component from the two longer-lived components was determined. Once again, simulated data were generated using Eq. (7.1) along with the parameters listed in Table 7.1.

Assuming a minimum admissibility threshold of 90%, an SNR of approximately 500 is required for *in vivo* acquisition with two components. The SNR for tumor ROIs was 839 ± 381 (and 649 ± 211 for grey matter ROIs), while the SNR per voxel was 193 ± 61. Based upon the simulations shown in Fig. 7.2a, this SNR is sufficient to perform ROI-based MET_2 analysis *in vivo*; however, SNR is insufficient to perform voxel-based MET_2 analysis (with an admissibility of ≈ 50%). As a result, spatial smoothing with an anisotropic diffusion filter (as described in *Methods*) was used to increase SNR for voxel-based MET_2 analysis *in vivo*.

Again assuming a minimum admissibility threshold of 90%, an SNR of approximately 3000 is required to resolve all three components from the *ex vivo* data. The SNR for tumor ROIs was 3989 ± 2265 (and 2335 ± 344 for grey matter ROIs), while the SNR per voxel was 557 ± 28. Therefore, from Fig. 7.2 it can be seen that the SNR is sufficient to perform ROI-based MET_2 analysis and insufficient to perform voxel-based MET_2 analysis *ex vivo*. As a result, spatial

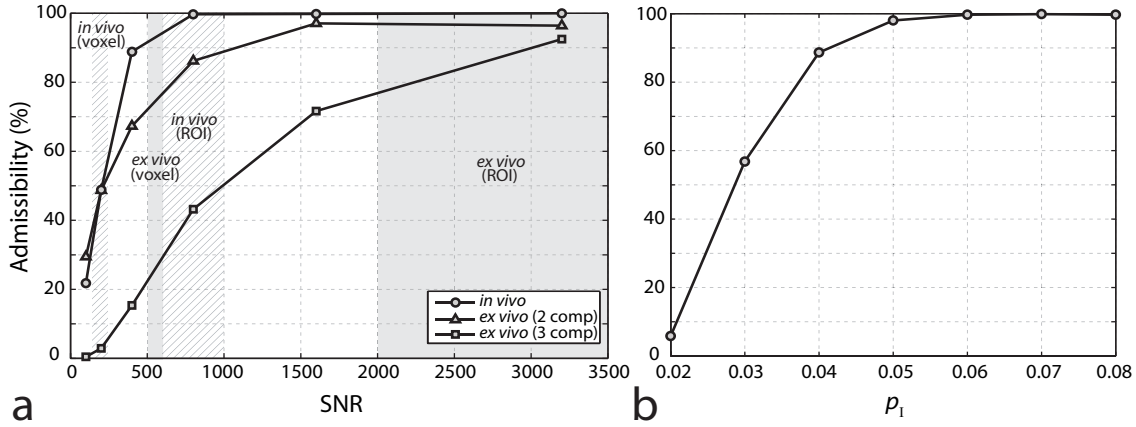

Fig 7.2. (a) Admissibility as a function of SNR for simulated *in vivo* and *ex vivo* tumor MET_2 data [using Eq. (7.1) and the parameters listed in Table 7.1]. For *ex vivo* data, the admissibility for resolving all three observed components (3 comp) as well as resolving the short-lived component from the two longer-lived components (2 comp) was tabulated. The approximate range of experimental SNRs for voxel- and ROI-based analyses *in vivo* (hatched boxes) and *ex vivo* (grey boxes) is also indicated. (b) Admissibility as a function of p_I for simulated *in vivo* data (SNR = 800).

smoothing with an anisotropic filter was also used to increase SNR for voxel-based MET_2 analysis *ex vivo*. Additional simulations showed that an SNR of approximately 1000 is required to resolve the short-lived component (component I) from the two longer-lived components (components II and III) in the *ex vivo* data. Thus, for comparison to the two-component *in vivo* spectra, *ex vivo* spectra that exhibited either two or three components were deemed admissible for voxel-based analysis.

An additional set of simulations was performed to assess the effect of the size of the short-lived component (p_I) on admissibility. Sets of two component data were generated over a range of p_I values using the same relaxation times and data sampling parameters as the *in vivo* simulations and an SNR of 800 (similar to ROI-based analysis *in vivo*). As seen in Fig. 7.2b, admissibility was found to increase with increasing size of the short-lived component. Using the

same minimum admissibility threshold of 90% as above, these simulations suggest that we should consistently observe MET_2 relaxation when the size of the short-lived component is greater than approximately 4% of the total signal.

In vivo Magnetic Resonance

Fig. 7.3 displays the results of the ROI-based MET_2 analysis *in vivo*. Fig. 7.3a and 7.3b show sample T_2 decay curves from normal and tumor ROIs and corresponding monoexponential fits [Eq. (7.2) with $J = 1$]. It can be seen that signal from tumor ROIs showed a larger deviation from a monoexponential model than signal from normal grey matter, suggesting a multiexponential model may be more appropriate for tumor signal. The MET_2 results (Fig. 7.3c and 7.3d) from normal and tumor ROIs support this. For tumor ROIs, eight of eleven animals exhibited T_2 spectra with two components: I) a short-lived component ($\overline{T}_{2,I}$ = 20.7 ± 5.4 ms) representing 6.8 ± 6.2% of the signal and II) a long-lived component ($\overline{T}_{2,II}$ = 76.4 ± 9.3 ms) representing the remaining 93.2 ± 6.2%. In contrast, 99.4 ± 1.3% of the total signal could be described by a single component ($\overline{T}_2$ = 48.8 ± 2.3 ms) for normal grey matter, which is consistent with previous findings [2, 22]. The relaxation times ($\overline{T}_{2,n}$) and signal fractions (p_n) for each individual animal measured *in vivo* are detailed in Table 7.2.

Recall, images were smoothed with an anisotropic diffusion filter prior to voxel-based MET_2 analysis. Fig. 7.4 displays the effects of this spatial smoothing on representative mean spectral T_2, $<\overline{T}_2>$ [calculated using Eq. (7.3) over the entire spectral range $t_1/2 < T_{2,j} < 2t_{NE}$], and p_I maps. The $<\overline{T}_2>$ maps in Fig. 7.4a and 7.4b illustrate the location of the tumor, which has a much longer $<\overline{T}_2>$ than surrounding tissue. The p_I maps in Fig. 7.4c and 7.4d illustrate that the

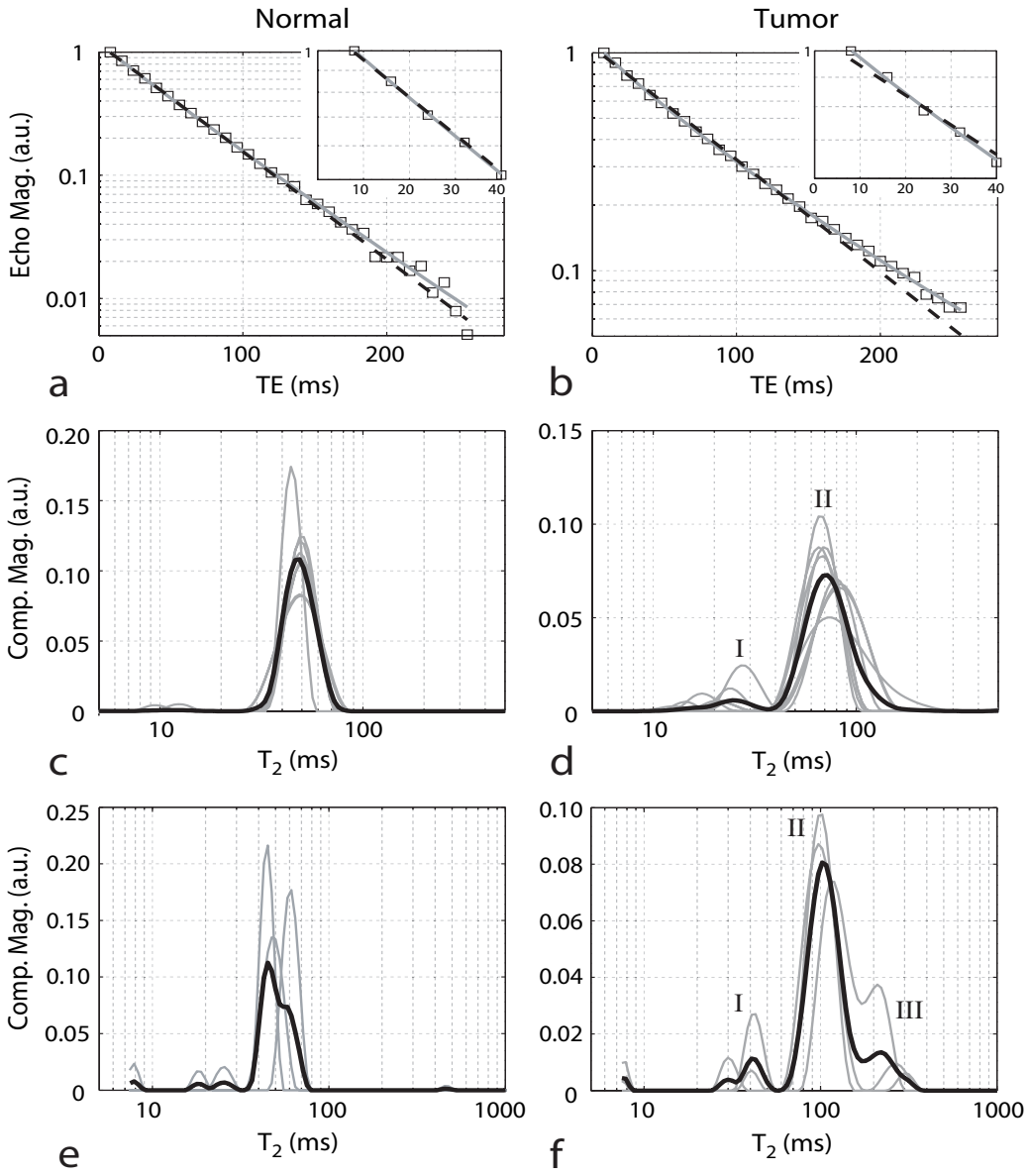

Fig. 7.3. (a and b) Sample decay curves from normal and tumor tissue ROIs *in vivo*. Data were fitted using multiexponential (grey solid line) and monoexponential (black dashed line) models. Note that tumor signal deviates from the monoexponential model fit, especially at shorter echo times as shown in the zoomed insets. (c and d) T_2 spectra from *in vivo* measurements for individual animals (gray) as well as the mean spectrum across animals (black). Two components (I and II) were observed in tumor signal in eight of the eleven rats *in vivo* (only spectra from these eight rats are given here), while signal from normal tissue was consistently monoexponential. (e and f) T_2 spectra from *ex vivo* measurements. Three components (I, II, and III) were in observed in tumor signal in all three rats. Once again, normal tissue was consistently monoexponential. Note, the small peaks to the far left of these spectra were deemed artifacts of the fitting process and were ignored in subsequent analysis. Component values for each rat are listed in Tables 7.2 and 7.3 for *in vivo* and *ex vivo* measurements, respectively.

Table 7.2. *In vivo* ROI-based MET_2 results for tumor and normal ROIs (as defined in Fig. 7.1). Component relaxation times ($\overline{T}_{2,n}$) and signal fractions (p_n) were tabulated for each animal using the spectra shown in Fig. 7.3 (panels c and d). The day post inoculation (DPI) each imaging study was performed is also given for each rat.

Rat		Tumor				Normal	
		I		II			
#	DPI	p_I (%)	$\overline{T}_{2,I}$ (ms)	p_{II} (%)	$\overline{T}_{2,II}$ (ms)	p (%)	$\overline{T}_2$ (ms)
1	14	4.5	25.5	95.5	68.1	100	50.7
2	15	4.6	21.2	95.4	85.6	100	44.6
3	16	21.2	28.1	78.8	80.1	100	49.2
4	14	3.0	14.5	97.0	67.4	100	50.3
5	14	8.5	24.3	91.5	70.2	100	49.6
6*	14	0	-	100	83.5	100	48.3
7*	18	0	-	100	80.8	96.8	50.1
8	18	2.0	12.6	98.0	66.2	100	49.6
9	21	3.7	21.9	96.3	85.3	100	49.8
10	18	7.2	17.7	92.8	88.2	96.8	50.1
11*	18	0	-	100	57.2	100	44.2
Mean	16.4±2.4	6.8±6.2	20.7±5.4	93.2±6.2	76.4±9.3	99.4±1.3	48.8±2.3

*Indicates animals whose tumor T_2 spectra exhibited a single peak (n.b., these three animals exhibited relatively small tumors). As a result, spectra from these animals are not given in Fig. 7.3. For these animals, component values for the single observed peak are given in the long-lived component columns and these values were ignored in calculating the mean component values across animals for tumor results.

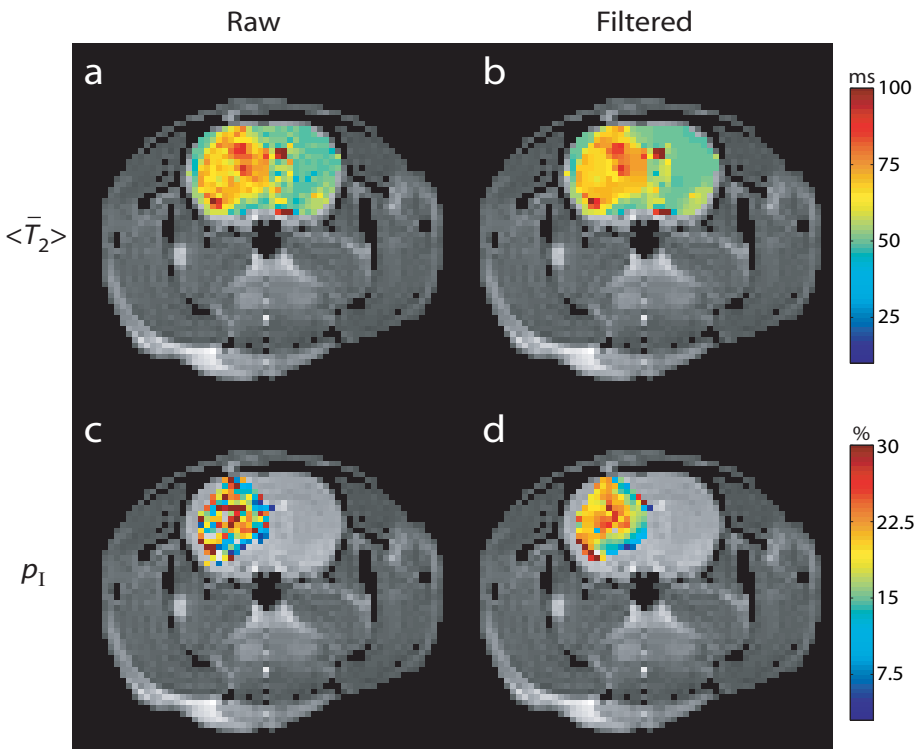

Fig. 7.4. $<\bar{T}_2>$ (a and b) and p_I (c and d) maps calculated from raw and filtered images overlaid onto an anatomical image from one animal (Rat #3). For p_I, only voxels whose T_2 spectra were deemed admissible — defined as spectra that exhibited two components in the range 8–200 ms — are shown. Additional contributions from white matter were also removed (see *Methods*). Observe that there exists significant intra-tumoral heterogeneity.

anisotropic spatial smoothing employed results in decreased variability for MET_2 results with minimal introduction of partial-voluming between tumor and normal tissue (though some information about tumor heterogeneity is likely lost after smoothing with this approach). Note, only results for voxels deemed admissible — defined here as voxels with spectra that exhibited two components in the range 8–200 ms — are shown. Additional contributions from white matter, which exhibited two components in this range consistent with previous findings [1, 2], were removed. These contributions were removed based upon the fact that the long-lived component in white matter has a $T_2 \approx 50$ ms (similar to the single component observed in grey

matter shown in Fig. 7.3c), while the long-lived component in tumor tissue exhibited a $T_2 \approx 75$ ms (Component II in Fig. 7.3d). Thus, only spectra whose long-lived component exhibited a $T_2 > 60$ ms are displayed in Fig. 7.4c and 7.4d (and in the p_1 maps in Fig. 7.5).

Additional representative $< \overline{T}_2 >$ and p_1 maps acquired *in vivo* are displayed in Fig. 7.5a (Rats #9–11). Note that tumor voxels consistently exhibited biexponential decay, while normal grey matter voxels did not, which is consistent with the ROI-based results shown in Fig. 7.3. Mean ROI component values for the voxel-based MET_2 results are summarized in Table 7.4 for all eleven animals. Only voxels deemed admissible within each ROI were used for these calculations. These results suggest that voxel-based MET_2 analysis might be possible *in vivo* because: 1) the voxel-based results (Table 7.4) were similar to those obtained from ROI-based analysis (Table 7.2) for most animals and 2) 86.1 ± 22.0% percent of voxels were deemed admissible. It should be noted that the ROI-based tumor signal was monoexponential in Rats #6 and 7, while the voxel-based signal was multiexponential (for 30.0 and 69.2 % of the voxels, respectively). This discrepancy can most likely be explained by partial-voluming of normal and tumor tissue within the chosen tumor ROIs.

Ex vivo Magnetic Resonance

Fig. 7.3e and 7.3f displays the results of the ROI-based MET_2 analysis *ex vivo*. For tumor ROIs, all three animals exhibited T_2 spectra with three components: I) a short-lived component ($\overline{T}_{2,I}$ = 37.8 ± 6.5 ms) representing 7.8 ± 6.5 % of the signal, II) an intermediate-lived component ($\overline{T}_{2,II}$

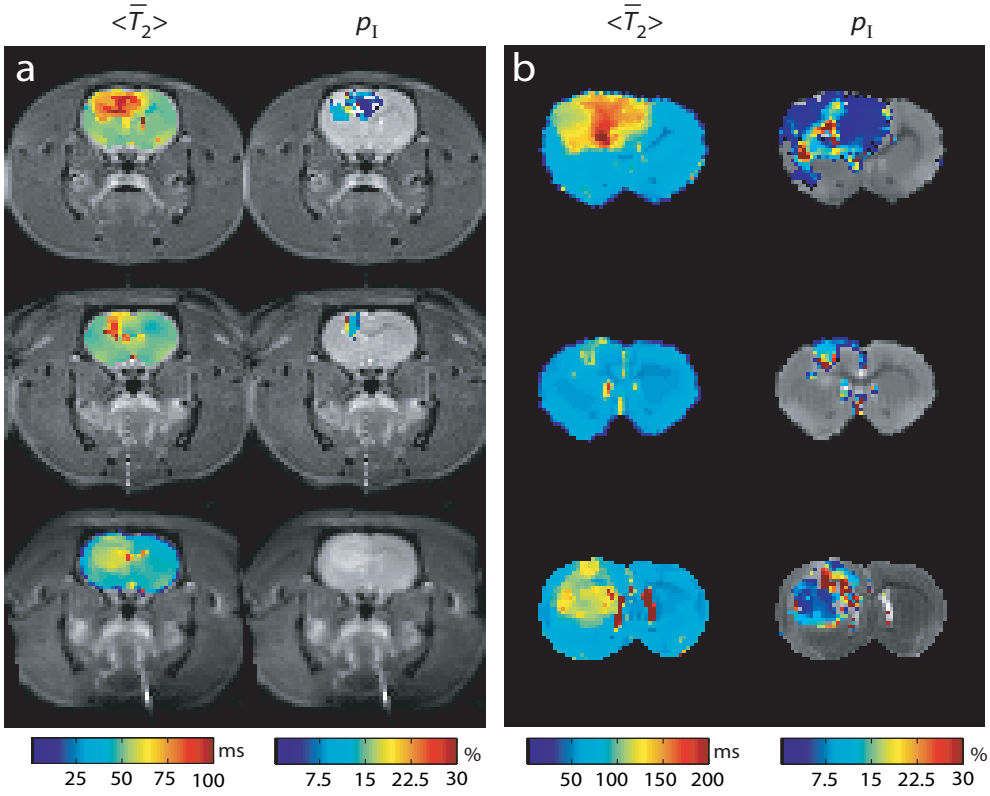

Fig. 7.5. (a) *In vivo* $<\overline{T}_2>$ and p_I maps overlaid onto anatomical images (Rats #9-11). (b) Corresponding *ex vivo* results from the same three rats. For p_I, only voxels whose T_2 spectra were deemed admissible — defined as spectra that exhibited two components in the range 8–200 ms or 15–300 ms for *in vivo* and *ex vivo* acquisition, respectively — are shown. Additional contributions from white matter were also removed (see *Methods*).

= 109.5 ± 14.2 ms) representing 80.6 ± 8.2% of the signal, and III) a long-lived component ($\overline{T}_{2,III}$ = 262.6 ± 44.6 ms) representing the remaining 11.6 ± 12.0% of the signal. Consistent with the *in vivo* findings, 94.5 ± 5.3% of the total signal could be described by a single component ($\overline{T}_2$ = 51.2 ± 8.4 ms) for normal grey matter *ex vivo*. It should be noted that relaxation times for components observed both *in vivo* and *ex vivo* (components I and II) were increased following fixation and washing in PBS, which is consistent with previous findings [23] in fixed primate grey matter. The relaxation times ($\overline{T}_{2,n}$) and signal fractions (p_n) for each sample measured *ex vivo* are detailed in Table 7.3.

Table 7.3. *Ex vivo* ROI-based MET_2 results for tumor and normal ROIs (as defined in Fig. 7.1). Component relaxation times ($\overline{T}_{2,n}$) and signal fractions (p_n) were tabulated for each animal using the spectra shown in Fig. 7.3 (panels e and f).

Rat	Tumor						Normal	
	I		II		III			
#	p_I (%)	$\overline{T}_{2,I}$ (ms)	p_{II} (%)	$\overline{T}_{2,II}$ (ms)	p_{III} (%)	$\overline{T}_{2,III}$ (ms)	p (%)	$\overline{T}_2$ (ms)
9	2.8	40.7	71.9	125.9	25.3	215.8	93.6	60.6
10	15.1	42.3	81.9	101.3	3.0	304.6	89.4	48.3
11	5.5	30.4	88.1	101.2	6.4	267.5	100	44.7
Mean	7.8±6.5	37.8±6.5	80.6±8.2	109.5±14.2	11.6±12.0	262.6±44.6	94.4±5.3	51.2±8.4

In contrast to ROI-based measurements, voxel-based T_2 spectra in tumor consistently exhibited only two components *ex vivo* (though three components were resolved for some voxels). Fig. 7.5b displays $< \overline{T}_2 >$ and p_I maps acquired *ex vivo* and Table 7.4 summarizes these results. Again, only results for voxels whose spectra were deemed admissible — defined here as spectra that exhibited either two or three components in the range 15–300 ms — are shown in Fig. 7.5b. Additional contributions from white matter were also removed by only displaying spectra whose long-lived T_2 component was > 70 ms (using the same arguments as described above for *in vivo* measurements). These results suggest that voxel-based MET_2 analysis might be possible with regards to resolving two components *ex vivo* because 97.6 ± 4.1% percent of voxel within tumor ROIs were deemed admissible.

Comparing *in vivo* and *ex vivo* voxel-based results, it can be seen that similar results were found for Rats #9 and #10, while a substantial difference was found for Rat #11. However, this

Table 7.4. Voxel-based MET_2 results acquired *in vivo* (Rats #1-11) and *ex vivo* (Rats #9-11). For each rat, mean (± SD) ROI component relaxation times ($\overline{T}_{2n}$) and signal fractions (p_n) were tabulated using voxel-based MET_2 analysis. Only voxels deemed admissible were used in these calculations. The total percentage of admissible voxels within tumor ROIs, or admissibility (*admiss*), was also tabulated.

Rat	*In Vivo*			*Ex Vivo*		
#	p_1 (%)	$\overline{T}_{2,1}$ (ms)	*admiss* (%)	p_1 (%)	$\overline{T}_{2,1}$ (ms)	*admiss* (%)
1	7.1 ± 2.8	28.7 ± 2.3	100			
2	10.8 ± 10.8	28.7 ± 10.6	88.9			
3	21.3 ± 3.3	29.4 ± 3.4	97.0			
4	4.6 ± 1.1	20.4 ± 3.2	100			
5	12.1 ± 1.6	28.4 ± 1.5	100			
6	6.9 ± 3.2	33.0 ± 5.6	30.0			
7	11.1 ± 9.6	29.9 ± 17.9	69.2			
8	2.7 ± 0.4	22.3 ± 4.3	90.0			
9	8.1 ± 10.2	26.6 ± 12.6	85.7	9.0 ± 10.1	48.9 ± 25.7	92.9
10	11.0 ± 1.5	22.5 ± 1.3	100	11.3 ± 3.0	34.9 ± 4.3	100
11*	0	-	0	5.3 ± 1.3	30.3 ± 4.3	100
Mean	9.6 ± 4.5	22.1 ± 5.5	86.1 ± 22.0	8.5 ± 4.8	38.1 ± 11.4	97.6 ± 4.1

*Indicates animal was ignored in calculating the mean values across animals for *in vivo* measurements.

particular animal (Rat #11) was sacrificed a full four days after the *in vivo* study (compared to one day for the other animals). Therefore, comparison between the *in vivo* and *ex vivo* data in this case is difficult as tumor growth had progressed significantly in those four days. In summary, the presented *ex vivo* results argue against the assertion that the *in vivo* results are due to either partial-voluming or low SNR.

Discussion

This study demonstrates that T_2 in a C6 rat glioblastoma model is heterogeneous on the scale of a typical MR voxel. Tumor signal exhibited two T_2 components in eight of the eleven animals *in vivo*, while a majority of the signal from contralateral grey matter could be described by a single T_2 component. Tumor signal in three of the eleven animals was monoexponential. Interestingly, the tumors of these animals were all relatively small in volume, suggesting that the observed MET_2 signal might contain information about tumor progression. It should be noted, however, that no correlation was found between time post-innoculation and any of the MET_2 parameters, which is not surprising given our observed variability in tumor volume across animals for a given time post-innoculation. Further longitudinal studies are needed to test the effect of tumor progression on MET_2 parameters.

A similar pattern was observed in the higher resolution and SNR *ex vivo* data; however, in this case three T_2 components were observed in tumor signal, while again a majority of the signal from contralateral gray matter could again be described by a single T_2 component. The reason an additional long-lived peak (component III in Fig. 7.3f) was resolved *ex vivo* is unclear. Previous studies in white matter [24] have shown that T_2 spectral characteristics are well-preserved in fixed samples. One possible explanation for the observed differences is the limited SNR of the *in*

vivo data. In fact, spectra resulting from *in vivo* ROI-based analysis and *ex vivo* voxel-based analysis — data used for each of these analyses had approximately the same SNR — both exhibited two components (at least for a majority of tumor voxels in the *ex vivo* voxel-based analysis).

MET_2 relaxation has been previously observed [6-10] in a number of tumor types and models with variable results. Given that microanatomical characteristics (and likely resultant relaxation spectra) vary across different tumor types and models, this observed variability is not surprising. Furthermore, a variety of models (e.g., biexponential, continuous) were employed in these past studies, which may be an additional contributing factor in this observed variability. In the current study, a linear least-squares algorithm with non-negative constraints (NNLS) was employed, which fits the data to a continuous distribution of decaying exponentials. This approach is particularly attractive as it makes no assumptions about the number of exponential components in the sample. Data sampling parameters (e.g, SNR, echo spacing) are an important consideration when employing such an approach [16]. In the current study, Monte Carlo simulations were performed to ensure that these were sufficient to obtain reproducible results.

A number of physiological and microanatomical parameters are altered in tumors that may affect T_2. This list includes variations in pO_2 [25], pH [26], and water content [27] as well as the presence (or absence) of irregular vasculature, necrotic tissue [28], or densely packed proliferating cells [29]. Given the heterogeneity common in tumors, a typical tumor voxel may contain regions that vary substantially in several of these parameters, which may explain the observed MET_2 relaxation. The relevance of each of these with respect to the findings presented herein is discussed below.

It has been known for some time that the mean T_2 (as well as T_1) of viable tumor is elevated relative to normal tissue [30] and that this increase correlates with increased water content [27]. This is consistent with the findings presented herein, in which $< \overline{T}_2 >$ was found to be elevated in tumors relative to contralateral grey matter. This can be attributed to the fact that the long-lived T_2 (76.4 ± 9.3 ms) component in tumor signal, which represented a majority of the total signal (93.2 ± 6.2%), was longer than that observed in contralateral grey matter (48.8 ± 2.3 ms). Therefore, it is reasonable to assume that the long-T_2 component in tumor signal represents signal from viable tumor tissue and that the underlying mechanism for the increased T_2 of the component is increased water content. It should be noted that additional factors may also play a role in the elevated T_2 of this component. For example, hypoxia (low tissue pO_2) and intracellular acidosis have been shown to result in increased T_2 in skeletal muscle [31]. Given that viable tumor cells are commonly hypoxic and acidic, these may be underlying factors contributing to the observed long-T_2 component in this study.

Assignment of an underlying mechanism for the short-T_2 component observed in tumor signal is less straightforward. Recall the T_2 of this component was substantially reduced (20.7 ± 5.4 ms) relative to contralateral grey matter (48.8 ± 2.3 ms); therefore, it is unlikely that this component reflects partial-volumed normal tissue within tumor ROIs (or voxels). One possible explanation for the observed short-T_2 component in tumor signal is the presence of densely packed proliferating cells. It has previously been shown [32] that T_2 and cellularity are inversely related in a human melanoma xenograft model — most likely attributed to that fact that macromolecular content increases and water content decreases with increased cellularity. The authors noted that T_2 varied by a factor of approximately 1.5 between regions with extracellular volume fractions of 5 and 70% (27). In terms of the current study, it appears that increased

cellularity alone cannot explain the observed short-T_2 component. Even if we assume that the extracellular volume fraction varies to the extreme of the previously mentioned study, this variation alone could not explain the approximately 2.5-fold decrease in T_2 of the short-T_2 component in tumor signal relative to contralateral grey matter. Another possible explanation for the observed short-T_2 component in tumor signal is the presence of irregular tumor vasculature (e.g., dead ends, shunts that are commonly found in tumor associated vasculature [28]), which may result in accumulation of paramagnetic deoxyhemoglobin and a corresponding decrease in T_2 for adjacent tissue. A final, more likely, explanation for this component is the presence of necrotic tissue, which has been shown to have decreased water content (and similar T_2) relative to normal tissue in surgical specimens taken from patients with lung cancer [8]. A longitudinal study [7] in an EO 771 adenocarcinoma mouse model also noted decreases in T_2 that correlated with the onset of necrosis.

Additional studies are needed to determine the physiological origin of these components. One proposed study is to use dynamic contrast-enhanced studies (DCE) MRI and histopathology and assess tumor necrosis. Correlation of these measures to the short-lived T_2 signal fraction will allow us to test the hypothesis that this component arises from necrotic tissue. Though the underlying physiological origin of the observed MET_2 components is currently unknown, MET_2 analysis holds promise as a non-invasive tool for characterizing the tumor microenvironment *in vivo* on a sub-voxel scale.

Acknowledgements

We thank Jarrod True for providing expert assistance and guidance in technical animal care and handling issues and Kevin Wilson for assistance in MATLAB code development.

References

[1] W. A. Stewart, A. L. Mackay, K. P. Whittall, G. R. W. Moore, and D. W. Paty, "Spin-spin relaxation in experimental allergic encephalomyelitis: Analysis of CPMG data using a nonlinear least-squares method and linear inverse-theory," *Magn Reson Med*, vol. 29, pp. 767–775, 1993.

[2] A. Mackay, K. Whittal, J. Adler, D. Li, D. Paty, and D. Graeb, "In-vivo visualization of myelin water in brain by magnetic resonance," *Magn Reson Med*, vol. 31, pp. 673–677, 1994.

[3] M. D. Does and R. E. Snyder, "T_2 relaxation of peripheral nerve measured in-vivo," *Magn Reson Imaging*, vol. 13, pp. 575–580, 1995.

[4] V. Vasilescu, E. Katona, V. Simplaceanu, and D. Demco, "Water compartments in myelinated nerve. 3. Pulsed NMR results," *Experientia*, vol. 34, pp. 1443–1444, 1978.

[5] G. Saab, R. T. Thompson, and G. D. Marsh, "Multicomponent T_2 relaxation of in vivo skeletal muscle," *Magn Reson Med*, vol. 42, pp. 150–157, 1999.

[6] R. M. Kroeker, C. A. Stewart, M. J. Bronskill, and R. M. Henkelman, "Continuous distributions of NMR relaxation times applied to tumors before and after therapy with X-rays and cyclophosphamide," *Magn Reson Med*, vol. 6, pp. 24–36, 1988.

[7] Z. Kovalikova, M. H. Hoehn-Berlage, K. Gersonde, R. Porschen, C. Mittermayer, and R. P. Franke, "Age-dependent variation of T_1 and T_2 relaxation times of adenocarcinoma in mice," *Radiology*, vol. 164, pp. 543–548, 1987.

[8] S. Shioya, M. Haida, Y. Ono, M. Fukuzaki, and H. Yamabayashi, "Lung cancer: differentiation of tumor, necrosis, and atelectasis by means of T_1 and T_2 values measured in vitro," *Radiology*, vol. 167, pp. 105–159, 1988.

[9] P. Fantazzini and A. Sarra, "A comparison of the proton relaxation in human epithelial tumors and associated uninvolved tissue," *MAGMA*, vol. 2, pp. 405–407, 1994.

[10] L. R. Schad, G. Brix, I. Zuna, W. Harle, W. J. Lorenz, and W. Semmler, "Multiexponential proton spin-spin relaxation in MR imaging of human brain tumors," *J Comput Assist Tomogr*, vol. 13, pp. 577–587, 1989.

[11] H. Y. Carr and E. M. Purcell, "Effects of Diffusion on Free Precession in Nuclear Magnetic Resonance Experiments," *Phys Rev*, vol. 94, pp. 630–638, 1954.

[12] S. Meiboom and D. Gill, "Modified Spin-Echo Method for Measuring Nuclear Relaxation Times," *Rev Sci Instrum*, vol. 29, pp. 688–691, 1958.

[13] J. M. Bonny, O. Boespflug-Tanguly, M. Zanca, and J. P. Renou, "Multi-exponential analysis of magnitude MR images using a quantitative multispectral edge-preserving filter," *J Magn Reson*, vol. 161, pp. 25–34, 2003.

[14] C. L. Lawson and R. J. Hanson, *Solving Least Squares Problems*. Englewood Cliffs, NJ: Prentice-Hall, 1974.

[15] K. P. Whittall and A. L. Mackay, "Quantitative Interpretation of NMR Relaxation Data," *J Magn Reson*, vol. 84, pp. 134–152, 1989.

[16] S. J. Graham, P. L. Stanchev, and M. J. Bronskill, "Criteria for analysis of multicomponent tissue T_2 relaxation data," *Magn Reson Med*, vol. 35, pp. 370–378, 1996.

[17] R. F. Barth, "Rat brain tumor models in experimental neuro-oncology: the 9L, C6, T9, F98, RG2 (D74), RT-2 and CNS-1 gliomas," *J Neurooncol*, vol. 36, pp. 91–102, 1998.

[18] C. S. Poon and R. M. Henkelman, "Practical T_2 quantitation for clinical applications," *J Magn Reson Imaging*, vol. 2, pp. 541–553, 1992.

[19] M. H. Levitt and R. Freeman, "Compensation for pulse imperfections in NMR spin-echo experiments," *J Magn Reson*, vol. 43, pp. 65–80, 1981.

[20] G. Gerig, O. Kubler, R. Kikinis, and F. A. Jolesz, "Nonlinear anisotropic filtering of MRI data," *IEEE Trans Med Imaging*, vol. 11, pp. 221–232, 1992.

[21] C. K. Jones, K. P. Whittall, and A. L. MacKay, "Robust myelin water quantification: averaging vs. spatial filtering," *Magn Reson Med*, vol. 50, pp. 206–209, 2003.

[22] M. D. Does and J. C. Gore, "Compartmental study of T_1 and T_2 in rat brain and trigeminal nerve in vivo," *Magn Reson Med*, vol. 47, pp. 274–283, 2002.

[23] H. E. D'Arceuil, S. Westmoreland, and A. J. de Crespigny, "An approach to high resolution diffusion tensor imaging in fixed primate brain," *Neuroimage*, vol. 35, pp. 553–65, 2007.

[24] C. Laule, P. Kozlowski, E. Leung, D. K. Li, A. L. Mackay, and G. R. Moore, "Myelin water imaging of multiple sclerosis at 7 T: correlations with histopathology," *Neuroimage*, vol. 40, pp. 1575–1580, 2008.

[25] A. R. Padhani, K. A. Krohn, J. S. Lewis, and M. Alber, "Imaging oxygenation of human tumours," *Eur Radiol*, vol. 17, pp. 861–872, 2007.

[26] R. A. Gatenby and R. J. Gillies, "Why do cancers have high aerobic glycolysis?" *Nat Rev Cancer*, vol. 4, pp. 891–899, 2004.

[27] I. C. Kiricuta, Jr. and V. Simplaceanu, "Tissue water content and nuclear magnetic resonance in normal and tumor tissues," *Cancer Res*, vol. 35, pp. 1164–1167, 1975.

[28] G. Bergers and L. E. Benjamin, "Angiogenesis: Tumorigenesis and the angiogenic switch," *Nat Rev Cancer*, vol. 3, pp. 401–410, 2003.

[29] K. A. Krohn, D. A. Mankoff, and J. F. Eary, "Imaging cellular proliferation as a measure of response to therapy," *J Clin Pharmacol*, pp. 96S–103S, 2001.

[30] R. Damadian, "Tumor detection by nuclear magnetic resonance," *Science*, vol. 171, pp. 1151–1153, 1971.

[31] B. M. Damon, C. D. Gregory, K. L. Hall, H. J. Stark, V. Gulani, and M. J. Dawson, "Intracellular acidification and volume increases explain R_2 decreases in exercising muscle," *Magn Reson Med*, vol. 47, pp. 14–23, 2002.

[32] I. Jakobsen, H. Lyng, O. Kaalhus, and E. K. Rofstad, "MRI of human tumor xenografts in vivo: proton relaxation times and extracellular tumor volume," *Magn Reson Imaging*, vol. 13, pp. 693–700, 1995.

CHAPTER VIII

CONCLUSIONS AND FUTURE WORK

The primary aims of this work were to: 1) develop and validate methods for measuring intercompartmental exchange 2) apply these methods in myelinated tissue, and 3) develop methods for resolving axonal and interaxonal water in white matter and optic nerve. To address the first aim, a novel method for measuring intercompartmental exchange (IR-REXSY), which allows for a significant reduction in scan time relative to existing methods, was presented in Chapter III. This method was subsequently tested by way of simulation studies and validated by way of phantom studies in Chapter IV. To address the second aim, the IR-REXSY method was applied in excised optic and sciatic nerve samples in Chapter V. For optic nerve, the fitted exchange rates were comparable to previously published values, further validating our novel approach. For the third aim, T_1–T_2 measurements were performed in a wide array of myelinated tissues before and after administration of contrast reagents as a means to characterize the compartmental enhancement pattern associated with each reagent. The results of these studies, which were presented in Chapter VI, suggest that administration of potassium dichromate might allow one to resolve axonal and interaxonal water in white matter and optic nerve *ex vivo*. Though not directly related, an additional study was included in Chapter VII, which showed that novel information about tumor microenvironment may be available *in vivo* using the inverse techniques presented throughout this work.

Several future studies are recommended based upon the finding presented herein. For the exchange studies, additional work is needed to determine the magnitude of MT effects on the derived exchange rates from our novel sequence. This may be addressed by: 1) including semi-solid proton pools and exchange between these pools and each mobile proton pool in our simulations and/or 2) simultaneously fitting additional MT-sensitive data with our exchange-sensitive IR-REXSY data. Also, it may be possible to extend the IR-REXSY approach into an imaging sequence, which would allow one to investigate exchange in more complex tissues (e.g., excised brain). As a result, this possibility needs to be investigated. For the chromium studies, additional work is needed to validate the postulated component-compartment relationship in chromated tissue. This is currently being investigated using X-ray fluorescence microscopy, a technique that may allow us to map the spatial distribution of chromium in our chromated tissue samples. Once validated, the increased anatomical resolution available in chromated white matter and optic nerve can be exploited to study the compartmental basis of diffusion and MT in these tissues.